UNIVERSITY OF NAPLES FEDERICO II

Polytechnic and Basic Sciences School

PhD in Chemical Sciences

XXXVI CYCLE

Protein aggregation mechanisms: from amyloid fibrils to the design of new bionanomaterials

Supervisor

Prof. Delia Picone

PhD student

Dr. Rosanna Lucignano

INDEX

INTRODUCTION

Molecular self-assembly is a hallmark of life[1], and refers to the spontaneous organization of molecules from a monomeric state to an ordered multimeric state under near-thermodynamic equilibrium conditions without external control[2,3]. The common features of the self-assembly process are to take advantage of mutual interactions between building blocks to form architectures with a defined structure[4]. Fascinated by the phenomena of natural self-assembly, scientific community has built different strategies to fabricate novel supramolecular architectures[5]. Basic building blocks widely used include small organic molecules[6], metal particles[7], DNA[8], and peptides[9]. Compared with these building blocks, the design and construction of nanoarchitectures with proteins as building blocks has been largely inaccessible due to their structural complexity and chemical heterogeneity. However, thanks to the structural and functional diversity, recently proteins have intensively been investigated as building blocks for nanostructured soft materials ranging from cages to extended two and three-dimensional arrays[10].

Consequently, the use of proteins as building blocks yields more hierarchical and powerful materials at different scales. Proteins self-assembly usually can be divided into two types of processes: spontaneous and non-spontaneous[11]. The first one spontaneously occurs in nature and concerns all the protein characterized by having a functional quaternary organization. This process consists in the intra-subunits assembly and involves mainly the interactions between protein subunits to form blocks for the construction of the final level of protein self-organization, the quaternary structure[12]. The other process is the inter-molecular assembly. It can be defined as non-spontaneous since it occurs in peculiar physico-chemical conditions, which represent a stressful environment for the protein. Through this route, the whole protein molecules, rather than subunits, are used as building blocks to form larger supramolecular structures through steerable assembly strategies. Clearly this process cannot be spontaneous but should be carefully directed. Although each design strategy adopts different specific methods, the springboard is the formation of appropriate specific interactions stabilizing the protein assembly. Moreover, specific interactions play a vital role in the assembly process. In particular, non-covalent interactions are dominant in self-assembly processes, which not

only sustain the stability of the accurate advanced structures, but also endows assemblies with structural sophistication and functional diversity[13]. By manipulating factors such as pH, ionic strength and temperature, these non-covalent interactions can be precisely controlled to regulate self-assembly behaviors to obtain all kinds of nanomaterials including 1D fibrils, nano-strings and nanotubes, 2D planar sheets and 3D protein cages, special frameworks and crystalline lattices[13–17].

Acquiring bionanomaterials with emerging properties is the ultimate goal of protein assembly. In living system, exquisite protein assemblies with hierarchical structure including microtubules, bacterial surface layers, and virus capsids are responsible for normal operation of life, which in turn, stimulate scientists to create artificial nanomaterials.

In this context takes place my PhD research project: it is based on the study of protein assembly mechanisms responsible for the formation of protein supramolecular structures.

The project objectives were:

1. Investigation of the self-assembly properties of nanotechnology relevant protein and the characterization of structure and morphology of the resulting fibrillar and/or nanocages

aggregates, with a particular attention to their dimensions, ordering and functional appealing properties. Different protein self-assembly model systems (single chain monellin, ribonucleases, amyloid β-peptides) were already available and deep-studied in my research group and others were easily accessible (insulin, albumin, ferritin).

2. Preparation of different types of protein-based aggregates and investigation of their structural and application-relevant properties.

The wealth of knowledge obtained in the previous objectives were the basis for the design (both at the molecular and at nanometre scale) and the preparation of novel proteinaceous materials for nanomedicine and/or nanotechnology applications.

In particular, my investigation focused on two types of self-assembly processes upon mild destabilization of the native state: one exploits the spontaneous tendency of a protein to form hollow nanocages under physiological conditions, and the other one takes places under moderate physico-chemical stress. As model systems for this analytical approach, I used ferritin, a protein characterized by a spherical architecture made

up by 24 subunits, and derivatives of the plant sweet protein monellin, already known the propensity to form fibrillar aggregates.

REFERENCES

(1) Sun, H.; Marelli, B. Polypeptide Templating for Designer Hierarchical Materials. *Nat Commun* **2020**, *11* (1), 351. https://doi.org/10.1038/s41467-019-14257-0.

(2) Whitesides, G. M.; Mathias, J. P.; Seto, C. T. Molecular Self-Assembly and Nanochemistry: A Chemical Strategy for the Synthesis of Nanostructures. *Science* **1991**, *254* (5036), 1312–1319. https://doi.org/10.1126/science.1962191.

(3) Mendes, A. C.; Baran, E. T.; Reis, R. L.; Azevedo, H. S. Self-assembly in Nature: Using the Principles of Nature to Create Complex Nanobiomaterials. *WIREs Nanomed Nanobiotechnol* **2013**, *5* (6), 582–612. https://doi.org/10.1002/wnan.1238.

(4) Philp, D.; Stoddart, J. F. Self-Assembly in Natural and Unnatural Systems. *Angew. Chem. Int. Ed. Engl.* **1996**, *35* (11), 1154–1196. https://doi.org/10.1002/anie.199611541.

(5) Zhang, S. Fabrication of Novel Biomaterials through Molecular Self-Assembly. *Nat Biotechnol* **2003**, *21* (10), 1171–1178. https://doi.org/10.1038/nbt874.

(6) Yang, P.; Zhao, W.; Shkurenko, A.; Belmabkhout, Y.; Eddaoudi, M.; Dong, X.; Alshareef, H. N.; Khashab, N. M. Polyoxometalate–Cyclodextrin Metal–Organic Frameworks: From Tunable Structure to Customized Storage Functionality. *J. Am. Chem. Soc.* **2019**, *141* (5), 1847–1851. https://doi.org/10.1021/jacs.8b11998.

(7) Xie, X.; Sun, T.; Xue, J.; Miao, Z.; Yan, X.; Fang, W.; Li, Q.; Tang, R.; Lu, Y.; Tang, L.; Zha, Z.; He, T. Ag Nanoparticles Cluster with pH-Triggered Reassembly in Targeting Antimicrobial Applications. *Adv Funct Materials* **2020**, *30* (17), 2000511. https://doi.org/10.1002/adfm.202000511.

(8) Shao, Y.; Jia, H.; Cao, T.; Liu, D. Supramolecular Hydrogels Based on DNA Self-Assembly. *Acc. Chem. Res.* **2017**, *50* (4), 659–668. https://doi.org/10.1021/acs.accounts.6b00524.

(9) Yang, J.; An, H.-W.; Wang, H. Self-Assembled Peptide Drug Delivery Systems. *ACS Appl. Bio Mater.* **2021**, *4* (1), 24–46. https://doi.org/10.1021/acsabm.0c00707.

(10) Yeates, T. O.; Liu, Y.; Laniado, J. The Design of Symmetric Protein Nanomaterials Comes of Age in Theory and Practice. *Current*

Opinion in Structural Biology **2016**, *39*, 134–143. https://doi.org/10.1016/j.sbi.2016.07.003.

(11) Subramani, K.; Khraisat, A.; George, A. Self-Assembly of Proteins and Peptides and Their Applications in Bionanotechnology. *CNANO* **2008**, *4* (2), 201–207. https://doi.org/10.2174/157341308784340831.

(12) Mason, T. O.; Shimanovich, U. Fibrous Protein Self-Assembly in Biomimetic Materials. *Advanced Materials* **2018**, *30* (41), 1706462. https://doi.org/10.1002/adma.201706462.

(13) Solomonov, A.; Shimanovich, U. Self-Assembly in Protein-Based Bionanomaterials. *Israel Journal of Chemistry* **2020**, *60* (12), 1152–1170. https://doi.org/10.1002/ijch.201900083.

(14) Bai, Y.; Luo, Q.; Liu, J. Protein Self-Assembly via Supramolecular Strategies. *Chem. Soc. Rev.* **2016**, *45* (10), 2756–2767. https://doi.org/10.1039/C6CS00004E.

(15) Yang, G.; Wu, L.; Chen, G.; Jiang, M. Precise Protein Assembly of Array Structures. *Chem. Commun.* **2016**, *52* (70), 10595–10605. https://doi.org/10.1039/C6CC04190F.

(16) Yang, L.; Liu, A.; Cao, S.; Putri, R. M.; Jonkheijm, P.; Cornelissen, J. J. L. M. Self-Assembly of Proteins: Towards Supramolecular Materials. *Chemistry A European J* **2016**, *22* (44), 15570–15582. https://doi.org/10.1002/chem.201601943.

(17) Korpi, A.; Anaya-Plaza, E.; Välimäki, S.; Kostiainen, M. Highly Ordered Protein Cage Assemblies: A Toolkit for New Materials. *WIREs Nanomed Nanobiotechnol* **2020**, *12* (1), e1578. https://doi.org/10.1002/wnan.1578.

CHAPTER 1

A supramolecular protein assembly: the ferritin nanocage

STATE OF ART

In bionanotechnology, biological engineered or native systems as varied as viruses, protein complexes, lipid vesicles and artificial cells, are being developed for applications in engineering, medicine, and materials science[1,2].

The capsids of viruses and other protein complexes, such as heat shock proteins, with defined interior cavities, are particularly attractive targets for bionanotechology: they can be readily produced in large quantities, have well-characterized atomic structures, are usually monodisperse in solution[3]. Among them, ferritins appear of particular interest.

The ferritin family proteins are ubiquitous in nature. The primary role of ferritin is to protect cells from the damage caused by the Fenton reaction, where, in oxidizing conditions, free Fe(II) produces harmful reactive oxygen species that can damage the cellular machinery[4]. They are also able to store a significant quantity of iron within a hollow core, and act as storage systems for iron within cells[5]. The active site of ferritin family proteins, named the ferroxidase center (FOC), is able to safely oxidize iron (II) in the presence of oxygen, or peroxide, to produce ferrihydrite minerals that are stored within the core of the ferritin nanocage[6]. The

FOC active site has conserved glutamic acid, aspartic acid and histidine residues that coordinate iron and facilitate its controlled oxidation[7].

The ferritins family has various members which show structural and functional differences. The classic ferritin (Ftn), found in eukaryotes and some bacteria, also known as maxi-ferritin, is a four-helix bundle protein of around 200 amino acids that self-assembles forming a cage of 24 subunits arranged in octahedral 432 symmetry[8], with an outer diameter of roughly 12 nm and an inner diameter of 8 nm able to storage up to 4500 iron atom (in the form of a ferrihydrite mineral core with variable amount of phosphate) (**Figure 1.1**). Mammalian ferritins are heteropolymers consisting of heavy chain subunits (H-chain, 182 amino acids) and light chain subunits, with a slightly lower molecular weight (L-chain, 174 amino acids)[9]. The ratio of the two types of subunits in ferritin is species- and tissue-specific, because each subunit carries out a different function. The H-chains play a major role in iron oxidation, and the L-chains are involved in the efficient nucleation and mineralization of iron[10].

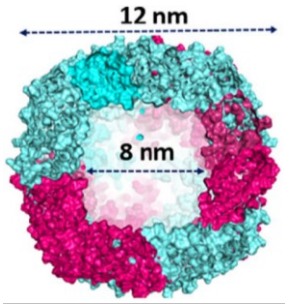

Figure 1.1. Computer model of a human heteropolymer ferritin with 70% H subunits (cyan) and 30% L subunits (hot pink)[11].

Other Ftn variants exist and include the amphibian M-chain ferritin, which has the FOC active site, but shorter than that of the H-chain Ftn[7] (**Figure 1.2**).

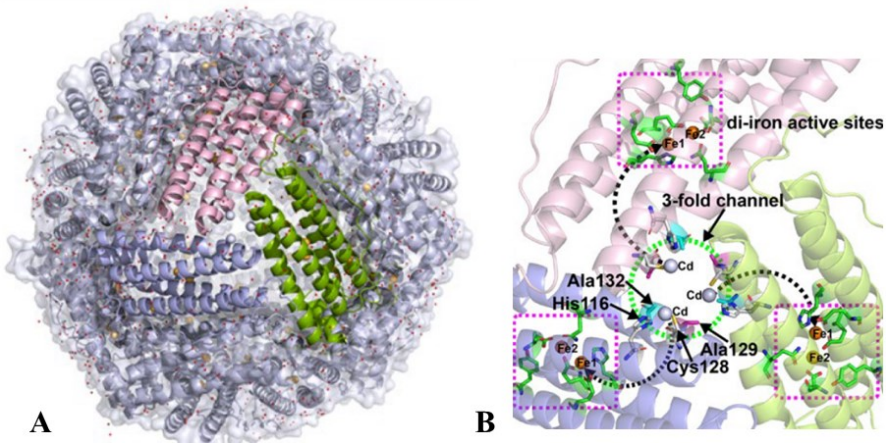

Figure 1.2. (**A**) stereo view of the M3 protein nanocage; (**B**) schematic overview of incoming metal ions moving via the three-fold channel from outside the M3 protein cage. The arrows indicate the connections from the three-fold channel toward ferroxidase sites in which yellow and light-blue spheres represent iron and cadmium ions, respectively[12].

Along with the classic ferritin, some bacteria and archaea possess bacterioferritin (Bfr), which differs from Ftn by the incorporation of twelve b-type heme groups between subunits in a two-fold symmetric binding site[13] (**Figure 1.3**).

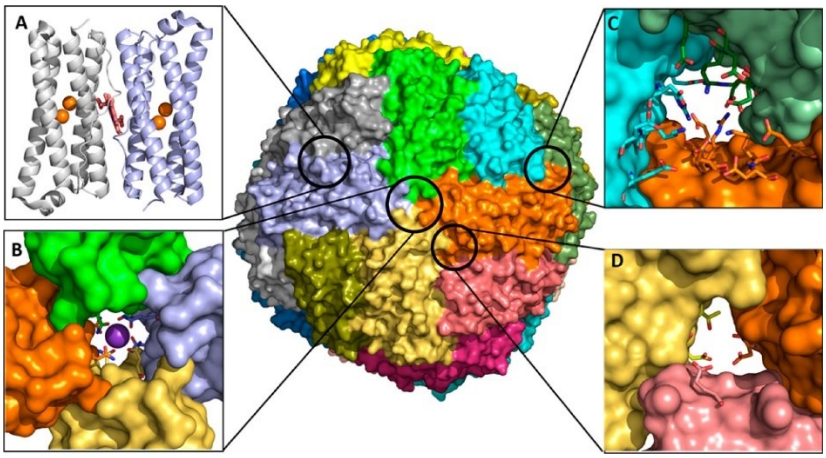

Figure 1.3. Bfr assembled from 24 identical subunits and 12 hemes. (**A**) The heme is at the interface of 2 subunits; iron is shown as orange spheres. The interior cavity is in contact with the exterior via 4-fold pores (**B**) (K^+ present in each of the 4-fold pores is shown as a purple sphere), 3-fold pores (**C**), and B-pores (**D**)[14].

In all the mentioned ferritin, each monomer is made up of a four-helix bundle (the A, B, C and D helices) with a short fifth helix (the E helix) at the C-terminus (**Figure 1.4**). In the octahedral cage structure (432 point group symmetry), each subunit interacts with six adjacent monomers through three types of symmetry-related interfaces. There are twelve dimerization interaction interfaces at the two-fold axes, eight

trimerization interaction interfaces at the three-fold axes and six tetramerization interfaces at the four-fold axes.

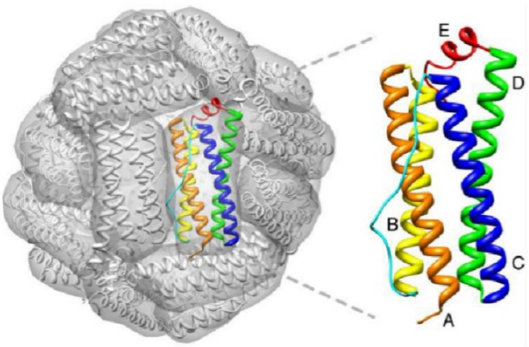

Figure 1.4. Typical structure of octahedral maxi-ferritin. The four-helix bundle monomers are shown as ribbons. The A helix is colored orange; the B helix, yellow; the BC loop, cyan; the C helix, blue; the D helix, green and the E helix, red[15].

Another member of the super family is the mini-ferritin, DNA-binding Protein from Starved cells (DPS), initially discovered in *Escherichia coli* cells during the stationary phase and found in many bacteria and some archaea[16], where its primary role is to protect the bacterial chromosome from oxidative damage[17]. In contrast to the 24-meric assembly of Ftn and Bfr, it has a dodecameric assembly (32 point group symmetry, tetrahedral), with 9 nm outer diameter and 5 nm inner diameter (**Figure 1.5**). Like Ftn and Bfr, DPS has a ferroxidase site and can store iron within its core, albeit in smaller quantities due to the smaller inner diameter of the dodecameric complex (up to ~500 Fe^{3+} ions)[18]. Like the

maxi-ferritins, the Dps monomer folds into a four-helix bundle (the A, B, C and D helices). However, unlike the maxi-ferritin, the loop between the B and C helices forms a short helix (**Figure 1.5**). The BC helix runs nearly orthogonal to the four-helix bundle axis and is exposed on the outside of the assembled protein cage. Moreover, the Dps monomer contains no E helix as is found in the maxi-ferritins.

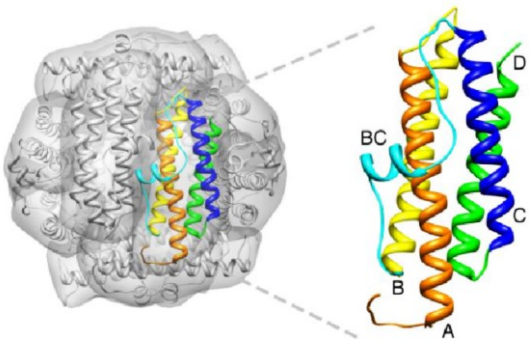

Figure 1.5. Typical tetrahedral structure of mini-ferritin. The four-helix bundle monomers are shown as ribbons. The A helix is colored orange; the B helix, yellow; the BC loop, cyan; the C helix, blue; the D helix, green[15].

The ferritin family proteins are probably the best-studied protein scaffold[19]. The ferritin cage has been employed as a template to mineralize a range of different non-physiological metals and metal complexes through either self-assembly around solutions of metal ions, chemically mediated redox reactions, or photochemistry[20,21]. The plasticity of the *in vitro* mineralization of ferritin makes it an ideal tool

for cellular imaging, as labelled heavy atoms and heavy atom complexes can be readily sequestered within its core. Furthermore, the ability to modify ferritin through protein engineering and chemical means has enabled their use as contrast agents in basic scientific investigations of cellular ultrastructure and for medical imaging. Iron-loaded ferritin has also been used as a contrast agent in both electron microscopy[22] and MRI[23]. Further to the use of ferritin as an MRI contrast agent, other clinical applications for ferritin family proteins arise from their nature as highly stable compartments that are biocompatible, amenable to disassembly, reconstitution, and surface modification. Indeed, ferritin nanoparticles contain three distinct exploitable interfaces: the interior and external surfaces, and the inter-subunit regions. All are amenable to manipulation through chemical and genetic engineering to make them useful for biotechnology. The smaller size of Ft compared with other drug carriers could lead to longer circulation half-life and to better accumulation rates. Furthermore, Ft possesses site-specific targeting potential, since it can be recognized and internalized by receptors over-expressed in a variety of malignant cells[24]. By using expression cloning, Li and co-workers identified human transferrin receptor-1 (TfR1) as an important receptor for the H-chain ferritin with little or no binding to L-

chain ferritin. They showed that after binding of HFt to TfR1 on the cell surface, HFt enters both endosomes and lysosomes[25]. Yu *et al*. found out that scavenger receptor class A (SR-A) are type II transmembrane proteins that recognize both self and non-self targets. Among them, SCARA5 can function as a receptor for L-chain ferritin[26]. These properties have been used to develop ferritin as a drug delivery platform[27]. Last but not least, at physiological pH ferritin exists as a stable 24-mer, whilst in highly acidic or basic solutions it disassembles, and when returned to a neutral solution the supramolecular complex spontaneously reassembles. This phenomenon can be used to trap molecules in solution within its cavity by dis/assembling ferritin in the presence of drug solutions. This procedure was firstly described by Ji and co-workers[28] and it is known as the alkaline pH protocol. By this procedure, the apo pig pancreas ferritin is disassembled at basic pH and then reassembled in the presence of the bioactive molecules to be trapped inside the protein bulk. In this way, during the reassemble stage, the biomolecule is trapped within the inner cavity of the cage. In particular, the Ft subunit disassociation and successive recombination are achieved by moving back and forth from pH 7.0 to 13.0. The latter protocol has been used for the first time to successfully load the cavity with metal

containing drugs, such as the cancer drug cisplatin[28] and the iron chelator desferrioxamine B[29]. Then, several other experiments replicated this encapsulation procedure to trap small molecules with success. However, this protocol has been applied mostly to horse spleen ferritin. During my PhD research activity, I carried out expression and purification of a recombinant human ferritin only composed of H-chains, the hHFt. This choose is due to the high affinity of H-chains for the transferrin receptor-1, overexpressed in different cancer cell lines, to improve the affinity of this protein for the tumoral cells. The objective has been a deep study of this new protein system, especially regarding its behavior in the experimental conditions that candidate it as a potential delivery system. In this respect, the first experimental approach has been a direct comparison with the widely used horse spleen ferritin: both proteins have been loaded with a small gold anticancer drug and they have been fully characterized. The results obtained from this first study opened several questions on the ferritin behaving in certain conditions which became the driving force of a series of analyses able to complete the mosaic depicting the protein in its entirety.

RESULTS AND DISCUSSION

1. A case study: Auranofin loading within ferritin nanocages

Auranofin (AF) is a drug that has been approved by FDA for the treatment of rheumatoid arthritis[30]. AF has shown potent anticancer activity against many cancer cell lines[31–33]. The drug complex consists of two parts, a water-soluble modified aurothioglucose entity with a sulfur donor group, and a phosphine ligand that provides lipophilicity (**Figure 1.6**).

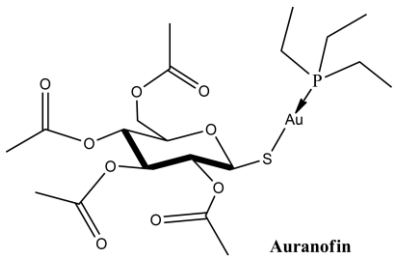

Figure 1.6. Schematic representation of Auranofin.

AF acts as a pro-oxidant agent, disrupting the redox system of the cell by strongly inhibiting thioredoxin reductases (TrxRs)[34]. Since it is already recognized and approved as a drug, AF has been selected as a candidate to be loaded in hHFt by using the alkaline

disassembly/reassembly protocol, already used to trap different metallodrugs within the Ft cage[35,36]. The experiment has been carried out simultaneously with the AF encapsulation within horse spleen ferritin to have a comparison.

Preparation and characterization of Auranofin-encapsulated horse spleen and human H-chain ferritins

The Auranofin-encapsulated human H-chain ferritin ($_{AF}$hHFt) and horse spleen ferritin ($_{AF}$hsFt) were prepared using the alkaline disassembly/reassembly protocol as described in the Materials and Methods section and characterized by circular dichroism (CD), UV-vis absorption spectroscopy and inductively coupled plasma-atomic emission spectroscopy (ICP-AES) , in collaboration with University of Pisa.

Far-UV CD spectra of $_{AF}$hHFt and $_{AF}$hsFt were collected to analyze the protein folding after the encapsulation procedure (**Figure 1.7 A-B**). The superposition of the CD spectra of gold-loaded Fts with those of AF-free proteins showed that the experimental conditions used for AF encapsulation did not significantly affect the secondary structure content of Fts, since the proteins kept their fold upon drug encapsulation.

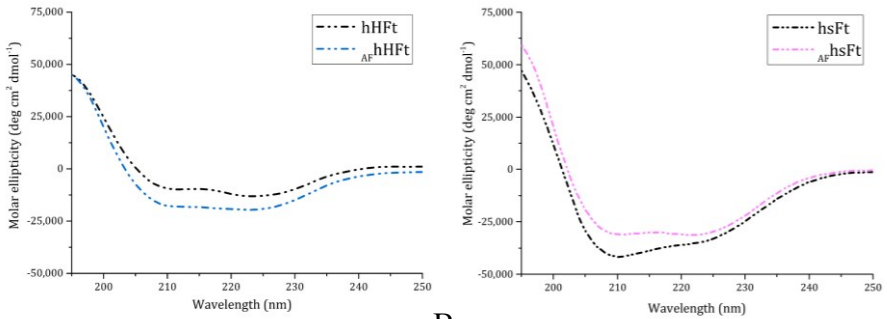

A B

Figure 1.7. Far UV-CD spectra of $_{AF}$hHFt (**A**, light blue dashes) and $_{AF}$hsFt (**B**, pink dashes) in comparison to the spectra of the respective gold-free proteins (black dashes).

Since it has been already reported that absorption increase in the region between 250 and 280 nm in the UV-vis spectrum of Fts indicates successful drug encapsulation[36,37], the UV-vis spectra of the AF-loaded nanocomposites were registered and compared with those of the respective drug-free Fts (**Figure 1.8 A-B**). Different results were obtained for the two preparations. $_{AF}$hsFt showed a significant absorbance increase between 250 and 280 nm when compared to the AF-free protein (**Figure 1.8 B**), while only a slight variance of the absorbance occurred when the spectrum of $_{AF}$hHFt was compared with that of hHFt (**Figure 1.8 A**). This difference may be associated with a variation in the drug loading ability of the two Fts.

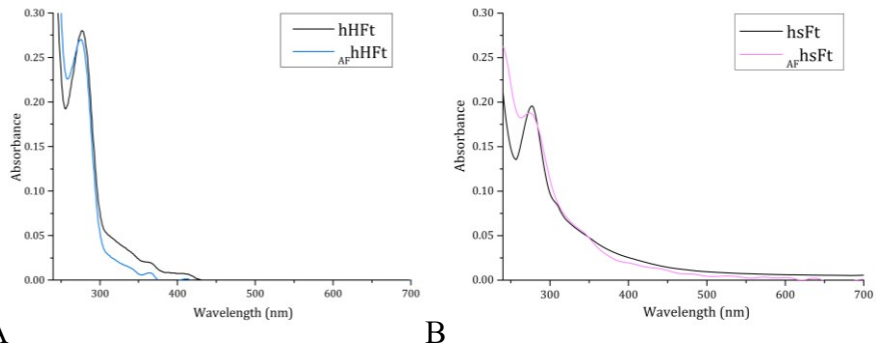

A B

Figure 1.8. UV–vis spectra of $_{AF}$hHFt (**A**, light blue line) and $_{AF}$hsFt (**B**, pink line) in comparison to the spectra of the respective gold-free proteins (black lines).

To explain the difference in the UV-vis spectra and to define with high accuracy the amount of AF that is encapsulated within the Ft nanocages, ICP-AES measurements were carried out. ICP-AES data indicated that about 270 gold atoms were encapsulated within $_{AF}$hsFt, achieving a protein chain to metallodrug molar ratio of ~1:11, while only about 90 atoms of gold were found in the nanocage based on the human H-chain Ft, with a protein chain to metallodrug molar ratio of ~1:4. Therefore, the ICP-AES analysis is in line with the conclusions suggested through UV-vis absorption spectroscopy. However, this unexpected difference required a deeper investigation, suggesting a structural characterization in order to identify the determinants of such a diverse behavior.

The AF-loaded nanocomposites were crystallized, and the X-ray structures were solved in the laboratory of Professor Antonello Merlino.

The overall conformation of both proteins in the crystals was not significantly affected by the presence of AF. The Cα root mean square deviations from the AF-free protein structures (PDB code 5ERK[35] for hsFt and 5N27[38] for hHFt were within the range 0.12–0.52 Å. Positions of gold atoms in both structures were identified by inspection of anomalous difference and Fourier difference (2Fo-Fc and Fo-Fc) electron density (e.d.) maps.

In the structure of $_{AF}$hHFt, two gold binding sites were found. The first one was close to Cys130. Here, a gold atom with low occupancy (0.15) was bound to the SG atom of the Cys and to a water molecule, showing a linear geometry (**Figure 1.9 C**). The second binding site was on the outer surface of the cage, close to the side chains of Cys90 and Cys102 (**Figure 1.9 B-D**). Here, several peaks in the anomalous difference e.d. map were found, suggesting the possibility that a "cluster" of gold atoms could be formed. The structure of the potential gold cluster could not be exactly defined since the interpretation of the maps at this site is very hard, also because of the disordering of residues 89–94 in that region (Cys90 and Glu94 have been modeled in two alternative conformations, in **Figure 1.9 D**). Whereas clear from the inspection of the maps is that two gold atoms were directly coordinated to the side chains of Cys90 and

Cys102. Considering that ICP-AES data indicated that $_{AF}$hHFt contains about four gold atoms per hHFt chain and that at least three Cys residues (Cys90, Cys102 and Cys130) bind gold centers in the X-ray structure of $_{AF}$hHFt, it can be concluded that only a small fraction of AF was encapsulated in the bulk of the hHFt nanocage.

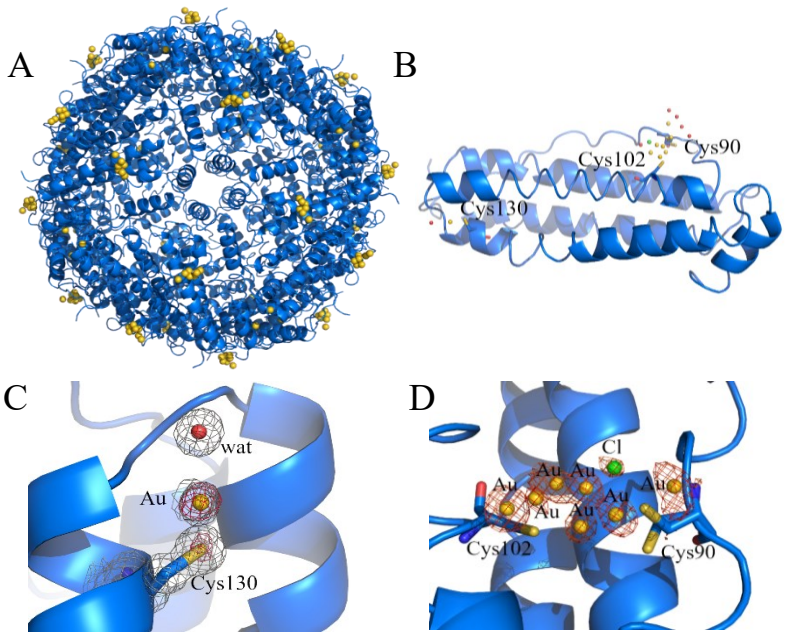

Figure 1.9. Cartoon representation of the structure of the cage (**A**) and of the single protein chain (**B**) of $_{AF}$hHFt. The gold binding sites are shown in panels (**C-D**), and 2Fo–Fc and anomalous electron density maps are contoured at 1.0 σ (grey) and 3.0 σ (red), respectively.

At variance with what was observed for $_{AF}$hHFt, the structure of $_{AF}$hsFt presented a single gold binding site. A gold atom with 0.20 occupancy

binds the SG atom of Cys126; a water molecule completes the metal coordination sphere, giving rise to a linear geometry (**1.10 Figure B-C**). In the case of $_{AF}$hsFt, the comparison between the structural data and the ICP-AES results (one gold binding site in the X-ray structure and 11 AF molecules per hsFt chain suggested via ICP-AES data) demonstrated that a significant fraction of AF is not directly bound to the protein, but it is encapsulated in the bulk of the hsFt nanocage.

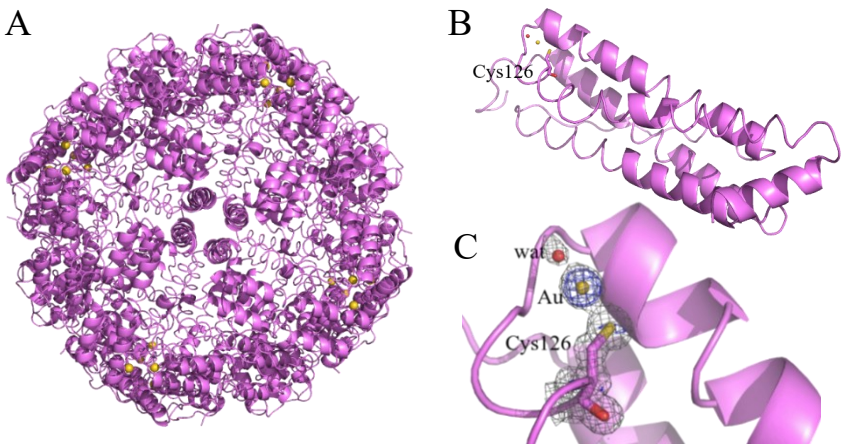

Figure 1.10. Cartoon representation of the structure of the cage (**A**) and of the single protein chain (**B**) of $_{AF}$hsFt. The gold binding site is shown in panel (**C**), and 2Fo–Fc and anomalous electron density maps are contoured at 1.0 σ (grey) and 3.0 σ (blue).

The anticancer efficacy of AF has been proven in different tumors, including several types of carcinomas[33]. To evaluate the cytotoxicity of AF when encapsulated within hHFt and hsFt, a human epidermoid

carcinoma (A431) and immortalized human keratinocytes (HaCaT) were incubated with increasing concentrations of $_{AF}$hHFt, $_{AF}$hsFt and AF. After a 48 h incubation, cell viability was evaluated via the MTT assay[39] and the respective IC_{50} values, corresponding to the drug concentration able to reduce the cell viability by 50%, were determined (**Table 1.1**). This assay was conducted in the laboratory of Professor Daria Maria Monti. By comparing the IC_{50} values obtained for the two gold-loaded nanocomposites with those obtained from treating cells with the free drug, it was possible to assess the effect of the protein on the toxicity and the selectivity of the metal compound. $_{AF}$hHFt was the system endowed with lower selectivity, as its IC_{50} value on immortalized cells was much lower when compared to $_{AF}$hsFt and even more so to AF. On the contrary, $_{AF}$hsFt preserved almost the same cytotoxicity of AF on the cancer cell line, but its selectivity was also decreased when compared to free AF.

Table 1.1. IC_{50} values expressed as gold concentration (μM) after 48 h of incubation with Auranofin, $_{AF}$hsFt and $_{AF}$hHFt (based on the concentration of AF obtained via ICP-AES) for HaCaT and A431 cell lines.

	AF	**$_{AF}$hHFt**	**$_{AF}$hsFt**
HaCaT	10.2 ± 0.4	1.1 ± 0.2	4.8 ± 1.5
A431	1.0 ± 0.1	1.3 ± 0.2	1.7 ± 0.6

The effect of hsFt on the pro-oxidant activity of metallodrugs leading to apoptosis activation has been investigated in several studies[37,40], while what happens when a metallodrug is in part encapsulated within the hHFt nanocage and in part bound on the outer surface of hHFt is not known. For this reason, the ability of AF and $_{AF}$hHFt to alter the redox state of A431 cells has been studied by measuring the intracellular ROS levels and the variation in the mitochondrial membrane potential, which are two biological markers for oxidative stress. In this respect, it is useful to recall that the mechanism of action of AF includes its pro-oxidant activity, related to the activation of apoptosis[34]. As shown in **Figure 1.11**, AF was able to induce a significant increase in intracellular ROS levels after an 8 h incubation, whereas $_{AF}$hHFt was able to significantly increase intracellular ROS levels after a 48 h incubation.

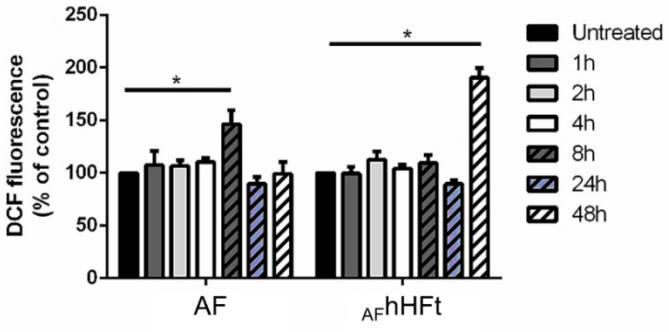

Figure 1.11. Time-course experiment to determine the effect of AF and $_{AF}$hHFt on intracellular ROS levels of A431 cells. Cells were incubated in presence of both AF and

$_{AF}$hHFt for 1 h (dark grey bars), 2 h (light grey bars), 4 h (white bars), 8 h (dashed dark grey bars), 24 h (dashed light grey bars), 48 h (dashed white bars). Black bars refer to the untreated cells. The fluorescence intensity of the probe is related to the intracellular ROS level and is reported as a percentage of untreated cells (%). Data shown are the means ± S.D. of three independent experiments and * indicates $p < 0.05$ with respect to untreated cells.

It is known that mitochondria are sensitive to changes in the cellular redox status and ROS activation is known to induce the depolarization of the mitochondrial membrane[41]. For this reason, the mitochondrial membrane potential of A431 cells upon AF and $_{AF}$hHFt treatment was measured via a TMRE assay[42] over time (**Figure 1.12**). A431 cells were incubated for 2, 4, 8, 16 and 24 h with an amount of AF and $_{AF}$hHFt corresponding to their IC_{50} values. In both cases, treatment resulted in the dissipation of the mitochondrial membrane potential ($\Delta\psi m$). However, for the free drug, a decrease in fluorescence intensity was observed already after 8 h incubation; whereas a strong depolarization started to occur after 16 h when cells were treated with $_{AF}$hHFt. The lowest permeability threshold found after 16 h of treatment remained constant up to 24 h of incubation. This implies mitochondrial damage during treatment with AF and $_{AF}$hHFt. These results are in line with those obtained with the alteration in ROS levels, thus suggesting that AF from $_{AF}$hHFt acts more slowly than the free drug.

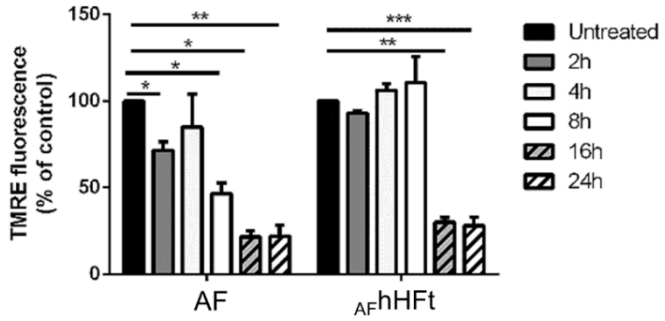

Figure1.12 . Changes in the mitochondrial membrane potential (Δψm) of A431 cells upon incubation with both AF and $_{AF}$hHFt. Cells were incubated for 2 h (dark grey bars), 4 h (light grey bars), 8 h (white bars), 16 h (dashed dark grey bars), 24 h (dashed white bars). Black bars refer to the untreated cells. The fluorescence intensity of the probe related to Δψm is reported as a percentage of the control (%). Data shown are the means ± S.D. of three independent experiments and * indicates $p < 0.05$, ** indicates $p < 0.005$, *** indicates $p < 0.001$ with respect to untreated cells.

Preliminary experiments on the mechanism of the action of $_{AF}$hHFt have also been carried out. Data suggest cell death induced by apoptosis, as observed in the case of cells that are treated with hHFt nanocages carrying high doses of doxorubicin[43], but these represented only preliminary results.

The present study aimed to verify that hHFt has the same ability of other ferritins to disassemble and reassemble at alkaline pH. Horse spleen ferritin, already used to encapsulate several metallodrugs[35–37,44] has been used as an experimental template for the human one. Thus, the two

nanocomposites, loaded in the same manner with the gold compound AF, were characterized from different point of views. The two AF-loaded systems showed significant differences especially regarding the loading efficiency and the localization of gold on the inner or outer surface of the cage. From these differences emerged the doubt that this encapsulation protocol does not fit for human H-chain ferritin, since most of the gold compound (in high molar excess to the respect of the protein) remains out of the cage. This prompted a deeper investigation of the efficacy of the encapsulation protocols present in literature and commonly used to load bioactive molecules within ferritin.

2. Investigation of alkaline pH protocol efficacy on human H-chain ferritin disassembly: set up of a new protocol of encapsulation

The experimental approach thought to obtain information of hHFt diverse behaving has been the analysis of each step of its disassembly and reassembly performed with the standard protocols present in literature and set up a new and more efficient procedure.

Indeed, an efficient procedure to disassemble hHFt nanocages using low concentrations of SDS, followed by dilution with pure buffer to allow

the reassembly, has been developed. The results obtained with this new protocol were compared with those obtained with methods usually applied for other Ft, based on the disassembly of the protein nanocage upon exposure to very acidic or alkaline pH and to its reassembly at neutral pH. The aggregation state of the protein upon different treatments was assessed by native PAGE electrophoresis (**Figure 1.33**). In a first experiment, five identical samples of 3 mg mL^{-1} hHFt dissolved in 20 mM Tris-HCl buffer pH 7.4 were incubated overnight in the presence of SDS at final concentrations of 1.0%, 1.5%, 2.0%, 2.5%, and 3.0%. Aliquots of each sample were analyzed on native gel (**Figure 1.13 A**, *lanes 2–6*). The comparison with the untreated sample (*lane 1*) revealed that all the tested SDS concentrations can completely disassemble the hHFt nanocages, as only a single band with a very high electrophoretic mobility was detected. After SDS removal by 10-fold dilution and extensive dialysis against 20 mM Tris-HCl pH 7.4, the samples were concentrated by ultrafiltration (cut-off 100.000 Da) to the initial volume and loaded on the gel (**Figure 1.13 B**). Only the bands corresponding to the untreated sample (*lane 1*) were detected in all the lanes, indicating that the hHFt nanocage is correctly and completely reconstituted, *i.e.,* the disassembly process is reversible. A following experiment was carried

out in similar conditions, but using lower concentrations of SDS, from 0.1% to 0.9%. Also in this case, PAGE under non-denaturing conditions revealed the efficient disassembly/reassembly of hHFt in all the explored experimental conditions (data not shown). Encouraged from this result, we evaluated the possibility of a further decrease of SDS percentages, from 0.01% to 0.09%. The PAGE analysis (**Figure 1.13 C**) reveals significant differences in the dissociation, as the nanocages are only partially dissociated at the lowest SDS concentrations, *i.e.,* from 0.01% to 0.07% (**Figure 1.13 C**, *lanes 2–8*), while full dissociation occurs only in the presence of 0.08% and 0.09% SDS. Based on these data, in the following experiments we selected 0.1% SDS to allow an extensive nanocage dissociation, while to remove the SDS and to achieve an efficient recovery of the reassembled form we used a 10 times dilution (*i.e.* a SDS reduction to 0.01%) followed by overnight incubation at 4 °C. Residual SDS was removed by extensive washing with pure buffer on *Centricon* tubes with cut-off 100.000 Da. In a further experiment, we decided to compare the disassembly/reassembly procedure based on the treatment with 0.1% SDS with the disassembly/reassembly protocols based on the pH switch, following the procedures described in detail in the experimental section. The results of the native gel, reported in **Figure**

1.13 D, revealed that upon treatment both at pH 12.0 and 13.0 (*lane 2* and *lane 4*, respectively) a large fraction of the protein migrates still like the untreated sample (*lane 1*), suggesting that the alkaline treatment allows only a partial disassembly of the nanocages. On the other hand, the acidic treatment allows a more efficient disassembly with respect to the alkaline treatment, as the band of the reference protein almost disappears (*lanes 6* and *8* for the samples disassembled at pH 1.5 and 2.0, respectively). Still, the disassembly process is not complete, as also indicated by the presence of an intense smear along both the lanes. As described in the experimental section, to allow the reassembly the samples were diluted with pure buffer, restoring the pH to 7.4, and incubated overnight at 4 °C. Then, before the native PAGE analysis, all the samples were concentrated to the initial volumes by ultrafiltration on *Centricon* tubes with cut-off 100.000 Da. In both cases, *i.e.,* upon incubation at pH 1.5 and 2.0, the nanocage band reappears after increasing the pH up to 7.4 (*lanes 7* and *9*), but no full recovery is achieved, since significant amounts of high-mobility species were still detected on the gel. In contrast, only the band corresponding to the 24-mer is detected in the sample reassembled after dissociation carried-out in the presence of 0.1% SDS (**Figure 1.13 D**, *lane 10*). Interestingly,

while during both the treatments at alkaline pH and with SDS the protein solutions remained always clear, the protein solutions incubated at acidic pH became cloudy when restoring the pH to 7.4, suggesting that a precipitation occurred.

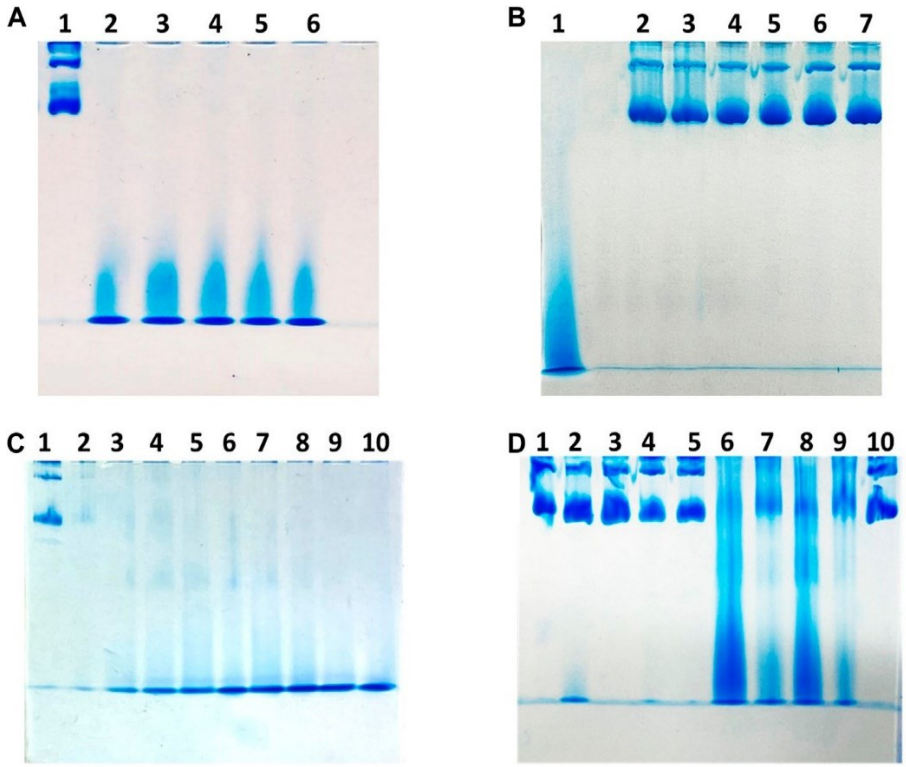

Figure 1.13. Gel electrophoresis under native conditions of hHFt to evaluate the assembly state upon different treatments. Panel (**A**) *lane 1* untreated hHFt; from *lane 2* to *lane 6* $hHFt_{SDS}$ incubated with 1.0%, 1.5%, 2.0%, 2.5% and 3.0% SDS, respectively. Panel (**B**) *lane 1* untreated hHFt; from *lane 2* to *lane 6* $hHFt_{SDS}$ incubated with 1.0%, 1.5%, 2.0%, 2.5% and 3.0% SDS after SDS removal by dialysis against 20 mM Tris-HCl pH 7.4. Panel (**C**) *lane 1* untreated hHFt; from *lane 2* to *lane 10* $hHFt_{SDS}$ incubated with 0.01%, 0.02%, 0.03%, 0.04%, 0.05%, 0.06%, 0.07%, 0.08%, and 0.09% SDS,

respectively. Panel (**D**) *lane 1*: untreated hHFt; *lane 2* $hHFt_{pH12.0}$ *lane 3* $hHFt_{pH\ 12.0->7.4}$ (reassembled); *lane 4* $hHFt_{pH\ 13.0}$; *lanes 5* $hHFt_{pH\ 13.0->7.4}$ (reassembled); *lanes 6* $hHFt_{pH\ 1.5}$; *lane 7* $hHFt_{pH\ 1.5->7.4}$ (reassembled); *lane 8* $hHFt_{pH\ 2.0}$; *lane 9* $hHFt_{pH\ 2.0->7.4}$ (reassembled); *lane 10* $hHFt_{SDS\ 0.1\%}$ (reassembled).

Accordingly, an estimation of the protein amount in the samples before and after the disassembly/reassembly procedures carried out by UV absorption spectroscopy shows that no significant protein loss occurs for samples treated at basic pH and with SDS, while more than 50% of the samples disassembled at acidic pH is lost. As further proof, aliquots of hHFt samples at pH 2.0, pH 13.0 and in the presence of 0.1% of SDS were taken and analyzed by TEM (**Figure 1.14)**. The provided data confirmed that a quantitative disassembly occurs at pH 2.0 (**Figure 1.14 A**) and in the presence of SDS (**Figure 1.14 C**), while at pH 13 (**Figure 1.14 B**) the nanocages are still present.

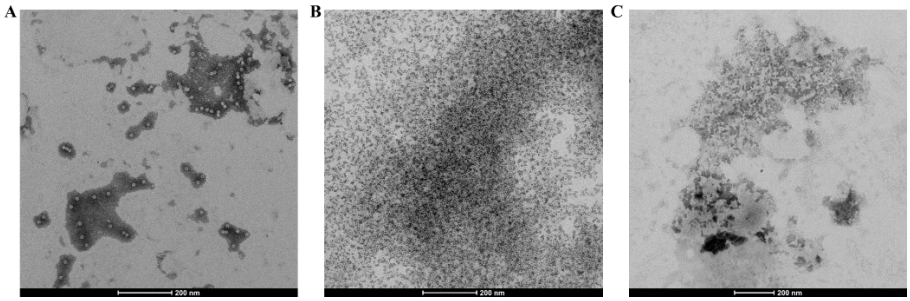

Figure 1.14. TEM bright field images (scale bar = 200 nm) of hHFt at (**A**) pH 2.5; (**B**) pH 13.0; and (**C**) 0.1% SDS. Samples were stained with 1.5% phosphotungstic acid.

Thus, based on the results of this comparative study, to perform a deep structural characterization of the hHFt nanocages obtained after the disassembly/reassembly procedure based on the treatment with 0.1% SDS, we prepared a new sample. Starting from 1 mL of a solution containing 1 mg of hHFt, after extensive washing with pure buffer in *Centricon* tubes (cut-off 100.000 Da) to remove residual SDS, the sample was concentrated to the initial volume. The final protein yield, estimated by UV absorbance, was 0.9 mg.

In addition, the behavior of hHFt in the different experimental conditions was monitored also using nuclear magnetic resonance (NMR) by acquiring 1D ^{1}H spectra. The comparison of the 1D spectra shown in **Figure 1.15** indicates that, in native conditions, hHFt signals are broad and have low intensity, and only a few signals are present, especially in the high field region, corresponding to the aliphatic side-chain protons (1-2 ppm) (**Figure 1.15 A**). This effect is consistent with the classic behavior of large proteins (50 kDa-500 kDa) in NMR spectroscopy, due to their fast transverse relaxation which causes a severe signal loss[45]. An increased intensity of the proton signals is evident in the spectra of the hHFt at both acidic and alkaline pH, indicating the presence in solution

of small-size molecular forms, while after the addition of 0.1% SDS_{d25}, only some high field signals displayed a higher intensity.

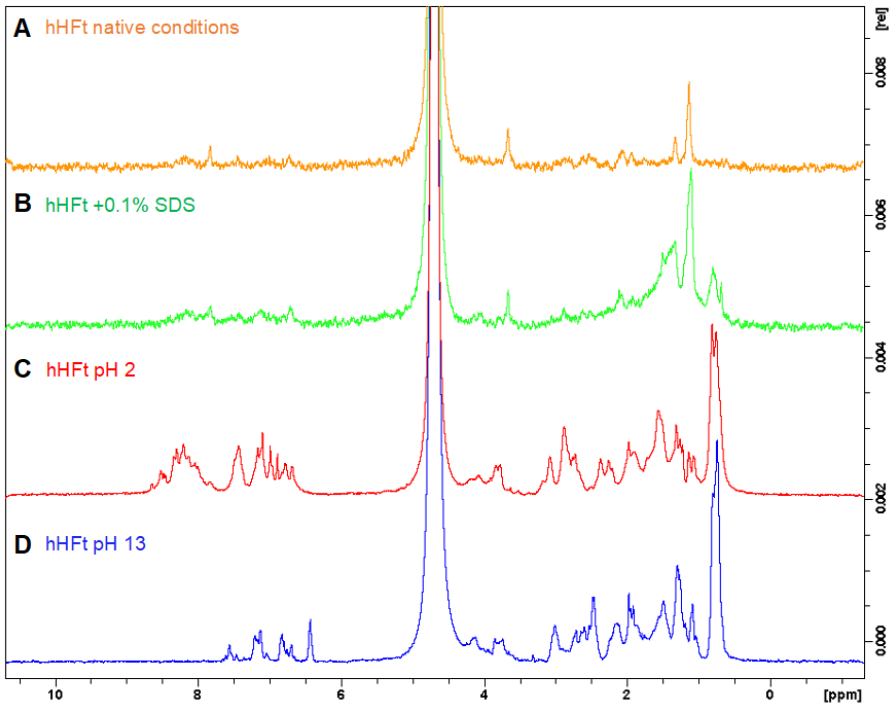

Figure 1.15. 1D ^{1}H NMR spectra of (**A**) native hHFt, (**B**) hHFt in the presence of 0.1% SDS_{d25}, (**C**) hHFt at pH 2.0 and (**D**) hHFt at pH 13.0. The hHFt concentration was held at 1.5 mg mL^{-1} in all the samples, and for each experiment 64 scans were recorded.

Thus, to better understand which aggregates are prevalent in solution, pseudo-2D DOSY experiments were recorded (**Figure 1.16)**. Moreover, to verify that the presence of 0.1% SDS do not affect the diffusion properties, DOSY spectra of the standard molecule 1,4-dioxane, were recorded by with and without 0.1% of SDS showing in both cases an

identical diffusion value of dioxane ($9.29 \pm 0.1\ 10^{-10}$ m^2/s). In the case of hHFt under native conditions, the absence of clear DOSY signals is consistent with a very slow diffusion coefficient (**Figure 1.16 A**). An increased value of the diffusion coefficient was observed in all the three disassembly conditions (**Figure 1.16 B-C-D**), indicating that smaller molecular size particles are formed in all cases. Moreover, the different values observed for the diffusion coefficient suggest dissimilar disassembly mechanisms between the protocol based on SDS and the ones based on pH-switch. In fact, the slower diffusion coefficient calculated for hHFt in SDS with the respect to hHFt at pH 2.0 and pH 13.0 suggests that the SDS treatment is able to disassembly the native nanocage but preserving same subunits interactions, in accordance with 1D NMR spectrum and TEM images. Conversely, the disassembly based on the pH changes prompts the formations of smaller aggregates but, as previously reported (*i.e.* TEM images and Native PAGE), only a few nanocages were dissociated and a very low amount of protein could be recovered upon reassembly.

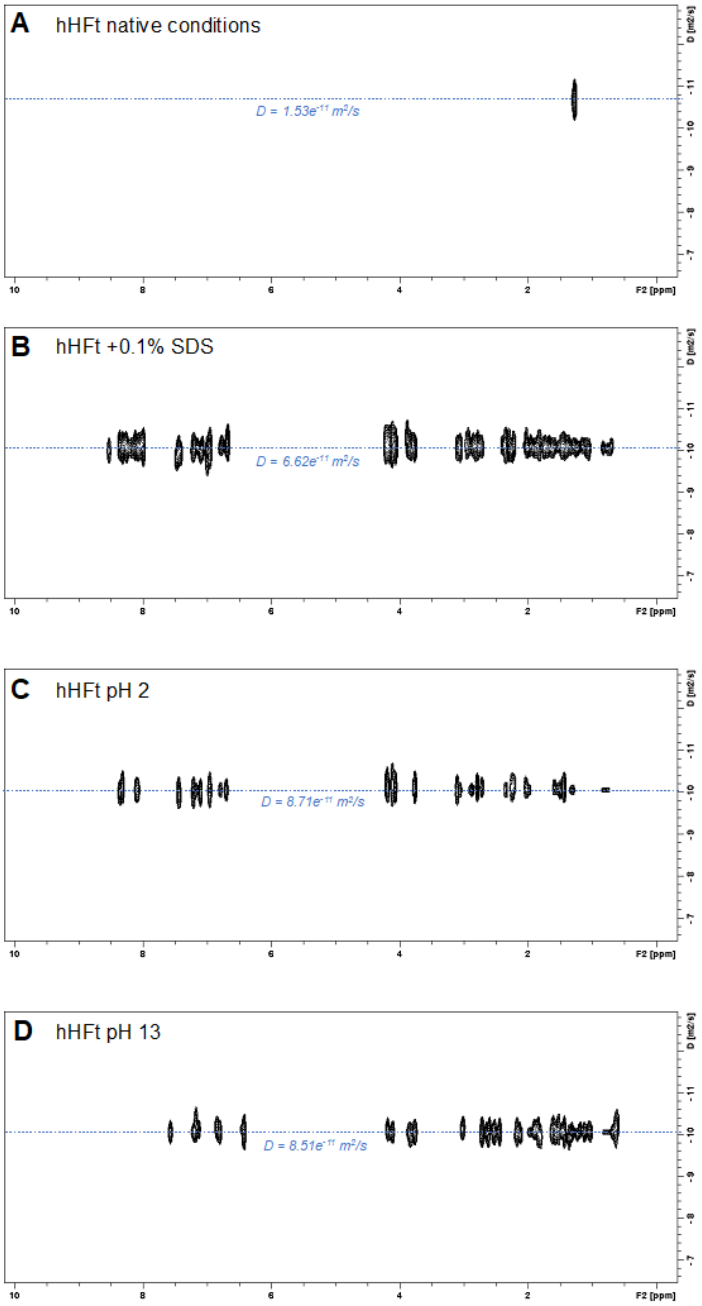

Figure 1.26. Pseudo-2D DOSY spectra correlating the chemical shifts (F2, ppm) with the diffusion values (D, m^2/s, Log_{10} scale) of (**A**) native hHFt, (**B**) hHFt in the presence of 0.1% of SDS_{d25}, (**C**) hHFt at pH 2.0, and (**D**) hHFt at pH 13.0.

CD spectra, reported in **Figure 1.17**, revealed a substantial persistence of α-helical structure in the hHFt sample treated with SDS even though a reduction of the secondary structure content is evident in the disassembled sample. Notably, it can be appreciated that the hHFt structure is fully recovered after SDS removal, since the curves of the untreated protein and of the restored one are overlapped.

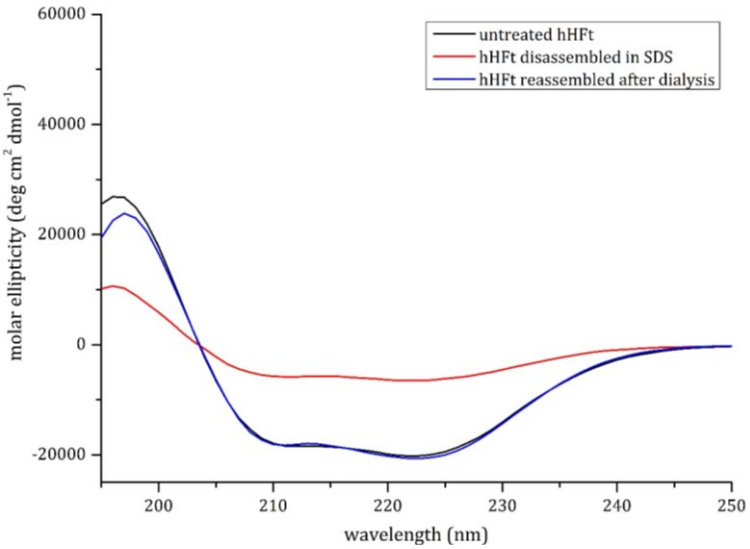

Figure 1.17. CD spectra of hHFt during the SDS treatment. *Black line*: untreated hHFt in 20 mM Tris-HCl pH 7.4; *Red line:* hHFt $_{SDS\ 0.1\%}$; *Blue line*: hHFt in 20 mM Tris-HCl pH 7.4 after SDS removal.

To further demonstrate that the protein cage was really disassembled and reversibly reassembled using the SDS protocol, TEM experiments were performed. The image of the untreated protein, clearly showing the

presence of numerous and empty hHFt nanocages, is displayed in **Figure 1.18 A**. The outer and inner diameters of the particles were 12.5 ± 0.6 nm and 7.7 ± 0.4 nm, respectively. **Figure 1.18 B** shows the efficient dissociation of the nanocages produced by 0.1% SDS, since only a few residual isolated hHFt nanocages can be observed. Finally, **Figure 1.18 C** demonstrates the correct reconstitution of the nanocages after SDS removal. Indeed, the hHFt reassociates with a morphology identical to that of the untreated sample with an outer diameter of 12.0 ± 0.4 and an inner diameter of 7.8 ± 0.4 nm, thus also this analysis further proved that the disassembly is completely reversible.

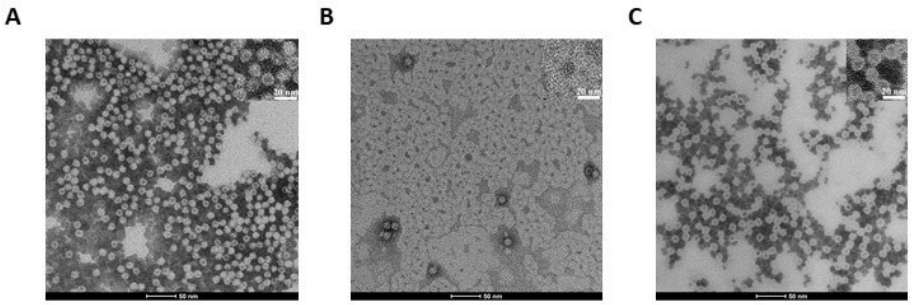

Figure 1.18. TEM bright field images ((scale bar = 50 nm, upper inset, 20 nm) of hHFt during the SDS treatment. (**A**) Reference (untreated) hHFt. (**B**) hHFt $_{SDS\ 0.1\%}$; (**C**) hHFt $_{SDS\ 0.1\%}$ reassembled after SDS removal. Samples were stained with 1.5% phosphotungstic acid. Notably, despite the use of negative staining, some hHFt nanocages appear slightly dark because of PTA absorption.

To verify that the hHFt reconstituted after SDS removal has the same features of the untreated hHFt, crystals of the protein after the SDS treatment ($hHFt_{SDS}$) were grown and the X-ray structure was solved. The structure, refined to 1.52 Å resolution (**Figure 1.19**), shows that the protein correctly reassembles after the SDS treatment, retaining all the features of the untreated sample. In particular, hHFt monomers adopt the four-helix bundle structure typical of the Ft fold (**Figure 1.19 A**) and assemble to form the hollow cage constituted by 24 molecules in 432 symmetries (**Figure 1.19 B**).

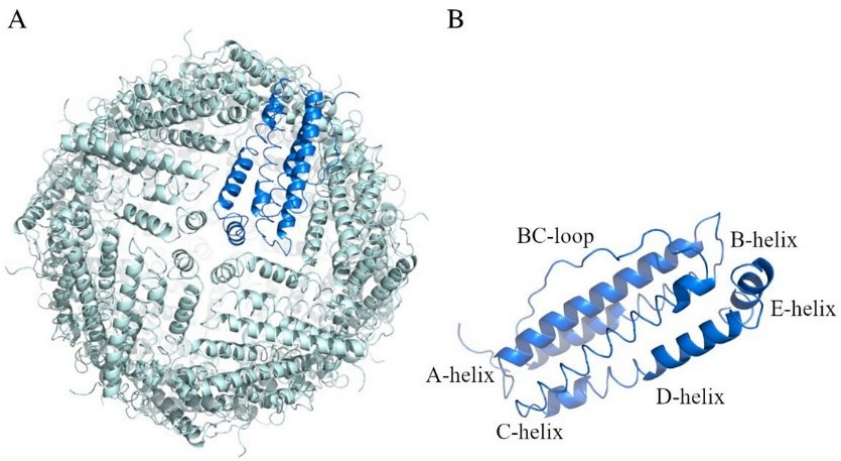

Figure 1.19. X-ray structure of the hHFt reassembled after disassembly in SDS: (**A**) the 24-mer ($hHFt_{SDS}$); (**B**) the single chain of hHFt. The asymmetric unit of the crystal contains one single chain; the 24-mer is generated by crystal symmetry. In panel **B**, the four helices (A-D), the short helix at the C-terminal tail (helix E) and the BC loop are highlighted. The structure has been deposited with the PDB code 8A5N.

The Cα r.m.s deviation of the $hHFt_{SDS}$ from that of hHFt in the starting model (PDB code 5N27) is as low as 0.61 Å. The shape, overall structure, polarity/hydrophobicity, volume, and electrostatic potential of the surface are conserved as shown in **Table 1.2**, thus unequivocally demonstrating that the cages correctly reassemble upon the SDS treatment.

Table 1.2. Structural features of ferritin treated with SDS-based encapsulation protocol in comparison with untreated ferritin (5N27)*.

Protein	**hHFt untread (downloaded from PDB)**	**$hHFt_{SDS}$ obtained using the SDS-based encapsulation protocol**
PDB code	5N27	8A5N
Total Accessible Surface Area (ASA) (Å^2)	9745.4	9863.5
ASA of backbone (Å^2)	882.3	873.4
ASA of side chains (Å^2)	8863.0	8990.1
Exposed non-polar ASA (Å^2)	5347.4	5428.5
Exposed polar ASA (Å^2)	1939.3	1897.2
Exposed charged ASA (Å^2)	2458.7	2547.8
Fraction non-polar ASA	0.55	0.55
Fraction polar ASA	0.20	0.19
Fraction charged ASA	0.25	0.26
% side ASA hydrophobic	18.87	18.84
Total volume (packing) (Å^3)	23715.7	23906.4

*determined using Vadar Server

To verify if there was residual SDS inside the nanocages or bound on the surface of the protein after the disassembly/reassembly protocol, 1D ^{1}H

NMR spectra of the hHFt reassembled after SDS removal by dialysis and filtration (**Figure 1.20 B**) in comparison with the spectrum of native hHFt (**Figure 1.20 A**) were acquired. Remarkably, the results show that the two profiles completely match and that there are no characteristic signals of the SDS, which include an intense signal around 1.25 ppm, and smaller multiples around 0.8, 1.5 and 3.7 ppm. However, to guarantee that the ferritin did not cover the signal of any SDS molecule hidden inside the bulk, an additional 1D ^{1}H NMR spectrum on the same sample but disassembled at pH 2.0 (**Figure 1.20 C**) was acquired. Also in this case, the spectrum did not show any of the characteristic signals of SDS, confirming once again the total absence of the SDS after the disassembly and the reassembly of the cages.

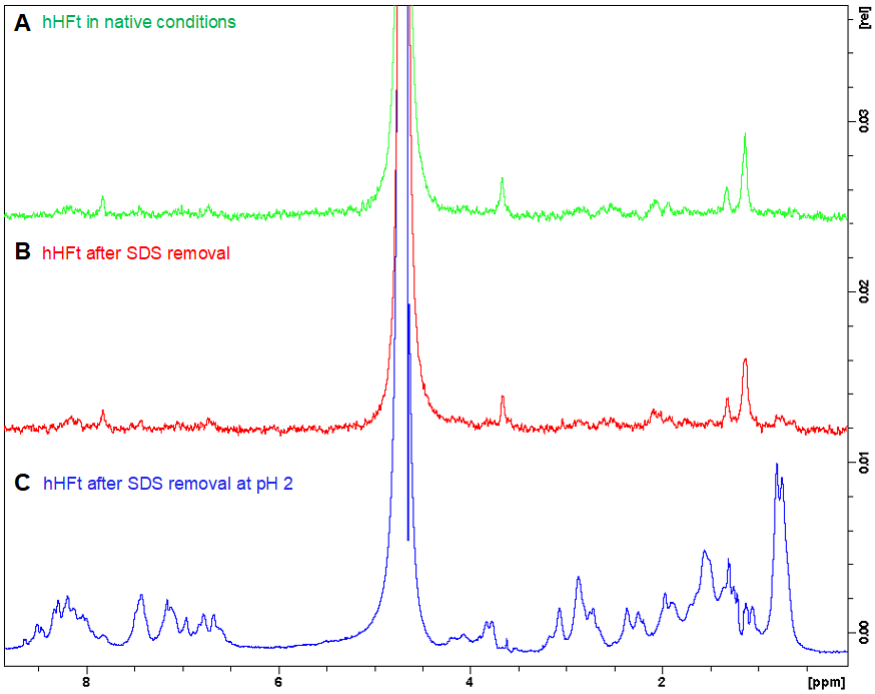

Figure 1.20. 1D ^{1}H NMR spectra of (**A**) native hHFt, (**B**) hHFt after SDS removal, and (**C**) hHFt after SDS removal at pH 2.0. The hHFt concentration was held at 1.5 mg mL^{-1} in all the samples, and for each experiment 64 scans were recorded.

Encouraged from the obtained results, we evaluated the possibility to use the SDS-based procedure to encapsulate two small molecules of different chemical composition, *i.e.,* the $[Ru(bpy)_3]^{2+}$ complex (Ru1) and a 13-residue bioactive peptide (TRIL), an analogue of the antimicrobial peptide Temporin L in hHFt.

Ru1 encapsulation

The SDS-based disassembly/reassembly protocol was used to encapsulate the metal compound Ru1 within the human H-ferritin using a 200:1 metal complex to hHFt cage molar ratio. Details of the encapsulation protocol are described in the experimental section. As indicated in **Figure 1.21 A**, after the SDS treatment the protein recovers its native structure upon reassembly. Indeed, the CD profile of the Ru1-hHFt sample was almost superimposable to that of the untreated one. The successful reassembly of the nanocages was verified by native gel electrophoresis, as reported in **Figure 1.21 B**. Indeed, the Ru1-hHFt sample (*lane 3*) shows the same profile as the untreated one (*lane 1*), while *lane 2* indicates the efficiency of the disassembly procedure. To estimate the amount of metal encapsulated within Ru1-hHFt, the UV-vis absorption spectrum was acquired in comparison with that of the untreated sample, at the same protein concentration. The Ru1-hHFt (**Figure 1.21 C**) showed an increase of the absorbance in the 400–500 nm range, confirming the presence of the Ru compound associated with the protein sample. The Ru1 concentration estimated using the absorbance at 452 nm was 26 μM, while the protein concentration

calculated using the Bradford assay was 6 μM, corresponding to a Ru1-hHFt cages molar ratio of 4:1.

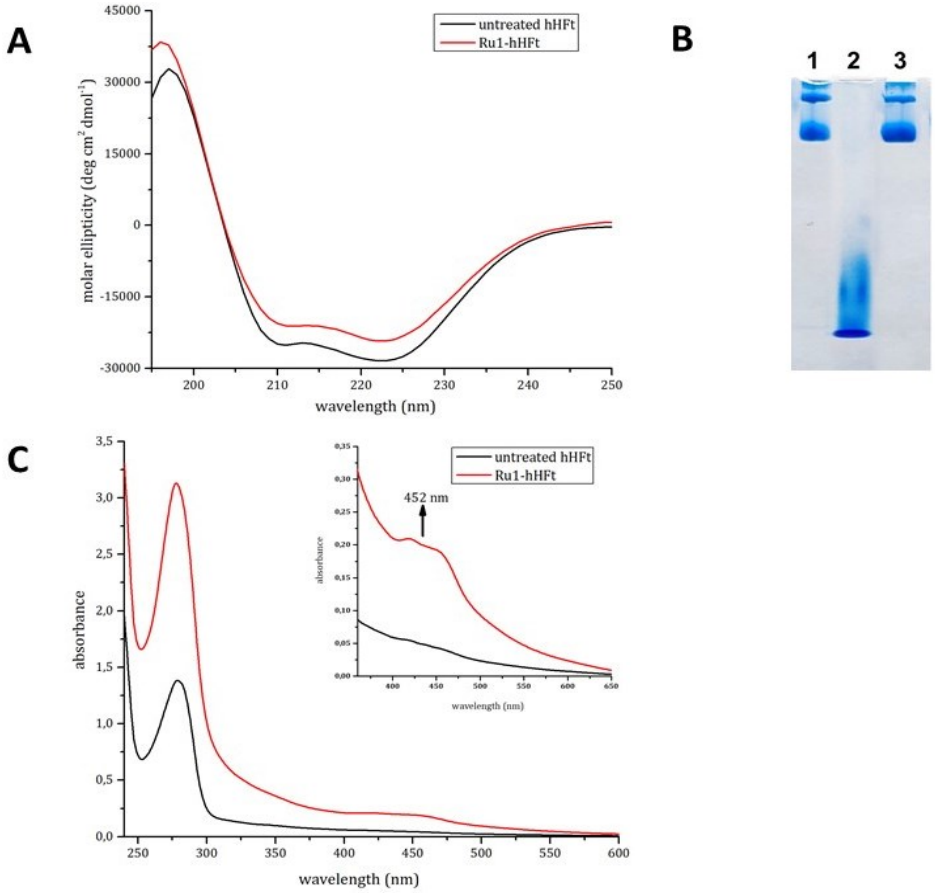

Figure 1.21. Electrophoretic and spectroscopic analysis of Ru1-hHFt. (**A**) CD spectra of reference hHFt (black line), and of Ru1-hHFt$_{SDS}$ (red line). (**B**) electrophoresis under native conditions of hHFt, lane 1 reference hHFt, lane 2 disassembled hHFt incubated with 0.1% SDS, and lane 3 Ru1-hHFt$_{SDS}$ after encapsulation. (**C**) UV-vis spectra of reference hHFt (black line), and of Ru1-hHFt$_{SDS}$ (red line). All the spectra were acquired in 20 mM Tris-HCl pH7.4.

The effective amount of the metal complex within hHFt was assessed by ICP-MS, yielding a value of 4.03 ± 0.19. This amount is comparable with the data reported by Li et al. and Conti *et al.*[46,47], through pH switch-based disassembly/reassembly protocols. Interestingly, the BCA assay allowed also to assess that more than 90% of protein was recovered after the complex encapsulation procedure.

Since CD spectra cannot provide indication on the correct cage reassembly of the Ru1-hHFt system[48], the X-ray structure of this system was also solved. The structure was refined to 1.57 Å resolution to R-factor/R_{free} values of 0.161/0.190 and compared to that of the untreated protein (PDB code 5N27)[38] and with $hHFt_{SDS}$. The structural analysis indicates that the overall conformation of hHFt in the Ru1-hHFt system formed in SDS is very similar to that of $hHFt_{SDS}$ and of the untreated protein. Notably, analysis of the electron-density map reveals that the Ru complex is not directly coordinated to the protein, neither on the inner shell nor in the outer shell, as observed when another Ru complex has been encapsulated within the horse spleen ferritin nanocage[37]. To confirm the presence of the Ru complex within the Ru1-loaded hHFt system, crystals of Ru1-loaded hHFt and of $hHFt_{SDS}$ were dissolved and analyzed spectrophotometrically. The UV-vis spectrum of Ru1-hHFt

from dissolved crystals shows a small band between 300 and 350 nm, observed also in the spectrum of the protein treated with the Ru compound in solution, but not found in the spectrum of hHFt (**Figure 1.22**). This result unambiguously demonstrates that crystals of Ru1-hHFt obtained upon the SDS-based encapsulation protocol and used for the structural determination contained the metal compound. Notably, the spectrum of dissolved Ru1-hHFt crystals does not show signals between 400 and 450 nm. The origin of this difference in the spectra is unclear, but it suggests a modification of the Ru compound structure inside the hHFt crystal, that alters its absorption properties.

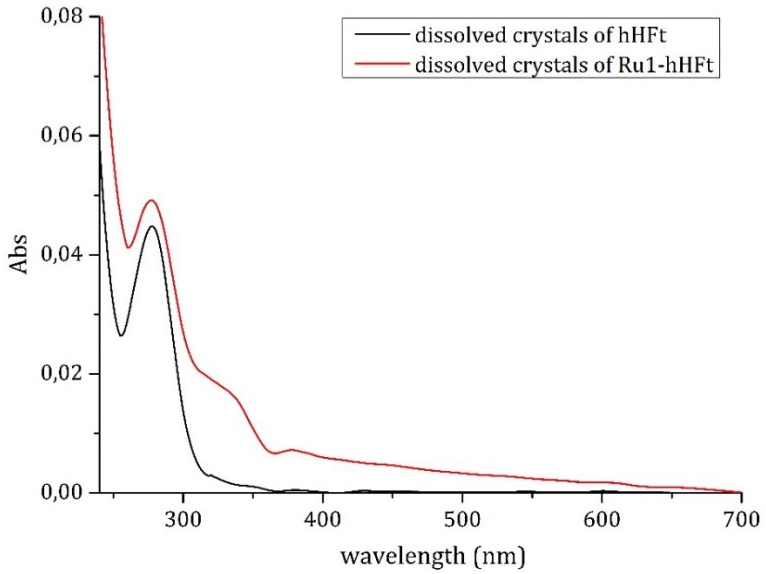

Figure1.22. UV-Vis spectra of dissolved crystals (in water) of hHFt disassembled and reassembled upon SDS treatment (hHFt, black line) and of Ru1-hHFt (red line).

Regardless the positive results, the ferritin nanocomposite loaded with Ru1 continued to be object of study with the aim to improve the loading efficiency. In particular, a modification of the SDS-based protocol was introduced: the SDS removal was carried out dialyzing Ru1-hHFt against a buffer containing the same concentration of Ru1. ICP-MS measurements showed an increase of loading capacity, from 4 to 10 Ru1 molecules encapsulated within the cage, supporting the obtained improvement.

The encapsulation of the complex Ru1 in the hHFt was observed also with 1D ^{1}H NMR spectroscopy (**Figure 1.23**). For a better comparison, spectra of Ru1-hHFt after the process of encapsulation before gel filtration (**Figure 1.23 A**), after gel filtration (**Figure 1.23 C**) and of free Ru1 (**Figure 1.23 B**) were acquired. Spectrum of hHFt in native conditions is also shown (**Figure 1.23 D**). From the results, it is possible to notice that there is a strong reduction in the intensity in several Ru1 signals when it is encapsulated in the nanocage (**Figure 1.23 C**), particularly the signals at 0.4, 1.2, 1.6, 2.2 7.4 and 7.8 ppm. The linewidth broadening in signals suggests an interaction with hHFt, which has fast relaxation and slow diffusion and can transfer these parameters to the smaller molecules that are enclosed in its core. These results provide

further evidence of the Ruthenium encapsulation within H-chain ferritin nanocages.

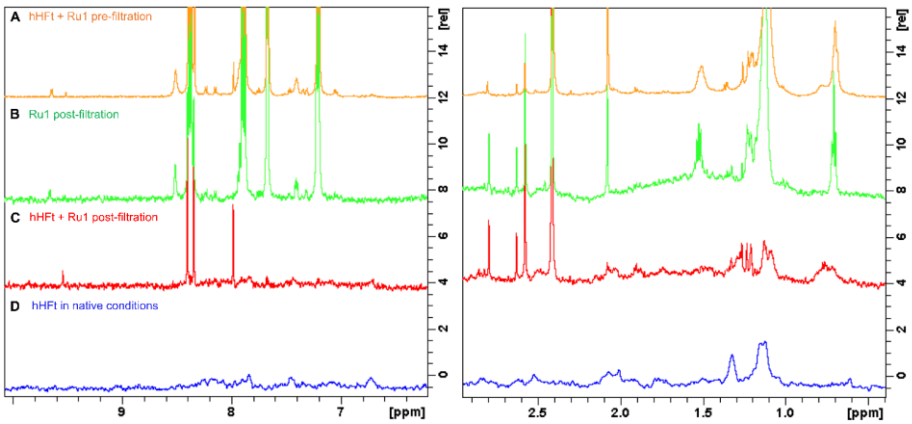

Figure1.23. 1D ^{1}H NMR spectra of (**A**) Ru1-hHFt after encapsulation protocol and before gel filtration, (**B**) free Ru1, (**C**) Ru1-hHFt after encapsulation protocol and after gel filtration, and (**D**) hHFt in native conditions.

Moreover, CRYO-EM data have been collected. Results confirmed the complete recovery of the original structure upon disassembly/reassembly. Preliminary structure of Ru1-hHFt (**Figure 1.24 A**) is reported in comparison to that of native hHFt (**Figure 1.24 B**). An overlap of both structure is also showed (**Figure 1.24 C**).

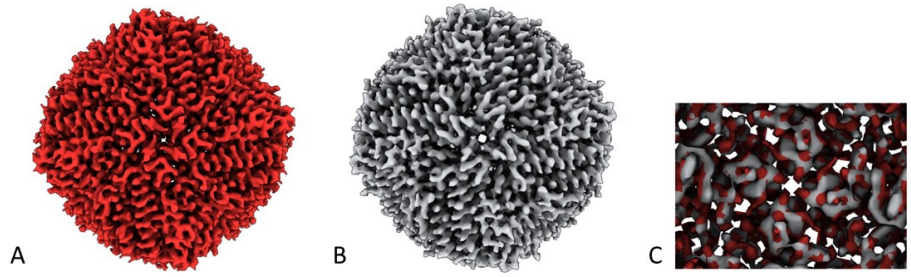

Figure 1.24. CRYO-EM structures of **A**) Ru1-hHFt, **B**) native hHFt, **C**) detail of ferritins bulk overlapped.

Peptide encapsulation

With the aim to verify if the developed disassembly/reassembly protocol can be used also to encapsulate peptides within the hHFt nanocage, TRIL and hHFt previously disassembled in SDS were mixed at a molar ratio of 1/1 peptide/protein subunit, as described in detail in the experimental section. TRIL belongs to the family of AMPs, small cationic and amphipathic molecules produced by all organisms that play a key role in the innate immune defense against viruses, bacteria, and fungi[49]. TRIL is a medium-sized peptide (FVKWFKKFLTRIL), analogue of Temporin-L (a-b-c-…), designed to improve the antibacterial activity. Temporin-like peptides have already been identified as strong anticancer agents. Recently, Temporin-1CEa was shown to exhibit a rapid cytotoxicity against human breast cancer cell lines[50], while Temporin-L was cytotoxic to three different human tumour cell lines (Hut-78, K-562 and U-937),

causing a necrosis-like cell death[51]. Remarkably, in this procedure we used a higher protein concentration, while keeping the SDS concentration of 0.1%. Upon 10 times dilution and incubation overnight, the reassembled nanocages were concentrated by ultrafiltration using *Centricon* tubes with cut-off 100.000 Da and analyzed by gel electrophoresis under native and denaturing conditions. The native gel (**Figure 1.25 A**, *lane 2*) reveals that, after the SDS treatment, the hHFt nanocages are disassembled but not completely converted into the highest electrophoretic mobility specie(s) observed when a much lower protein concentration is used, as multiple forms are detected. Also in this case, upon SDS dilution the nanocages are completely restored (*lane 3*) since the electrophoretic profile of the protein recovered is identical to that of the untreated one (*lane 1*). The denaturing gel-electrophoresis (**Figure 1.25 B**) of TRIL/hHFt (*lane 3*) was carried out by using both the untreated hHFt (*lane 1*) and TRIL (*lane 2*) as controls, confirming the presence of both hHFt subunit and peptide at the right molecular weights.

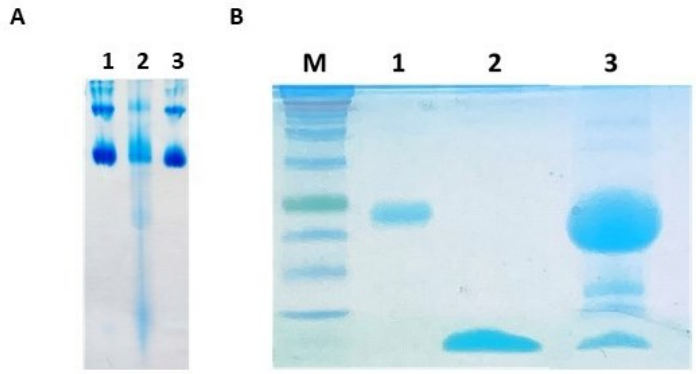

Figure 1.25. Electrophoretic and spectroscopic analysis of TRIL/hHFt: (**A**) Gel electrophoresis under native conditions of hHFt, *lane 1* reference hHFt and *lane 2* TRIL/hHFt after the encapsulation. (**B**) 15% SDS-PAGE gel of and treated samples: M proteins marker, *lane 1* reference hHFt, *lane 2* TRIL, *lane 3* TRIL/hHFt after the encapsulation.

The lowest band, corresponding to the antimicrobial peptide, was excised from the gel, and digested with trypsin. The resulting peptide mixture was directly analyzed by MALDI mass spectrometry. The mass spectrum (**Figure 1.26**) confirms the identity of the antimicrobial peptide with a 100% sequence coverage. **Table 1.3** reports the assignments of the mass signals recorded in the spectra.

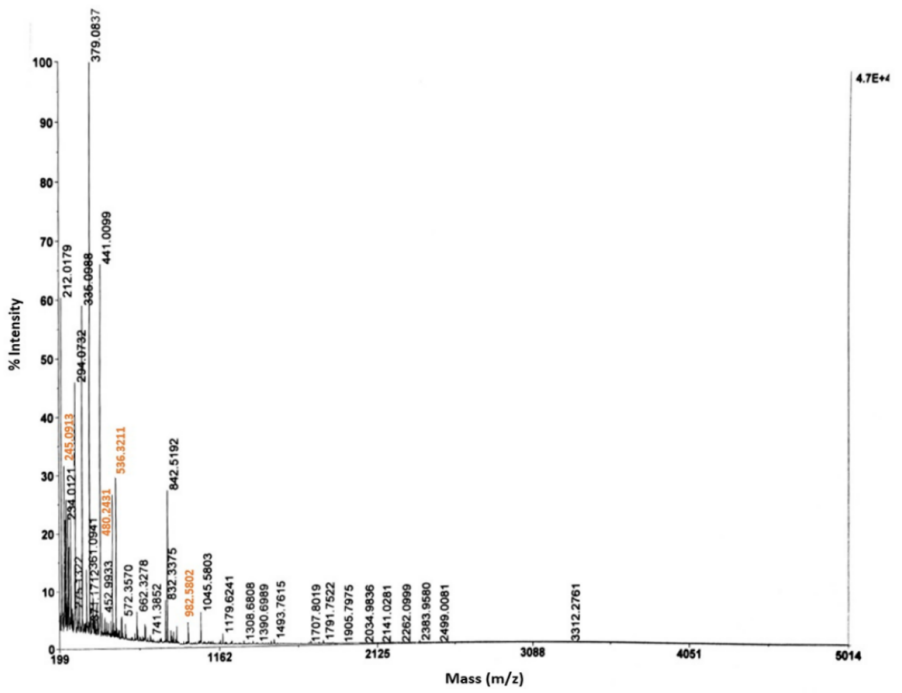

Figure 1.26. Assessment of the encapsulated peptide identity by mass spectrometry. The spectrum shows the relative abundance of ions as a function of the mass/charge (m/z) ratio. In orange the signals corresponding to peptides. The low intensity of the signals reflects the low amount of peptide obtained after extraction from the gel and hydrolysis. Notably, when a very low concentration of sample is available, like in this case, it is very common to observe some other peaks arising from the matrix (379.08, 441.00 m/z), the staining used (842.51 m/z) and the keratin (1045, 1179, 1308, 1707, 1791, 3312 m/z), often present as contaminants.

Table 1.3. Mass signals recorded in the MALDI spectra of the tryptic digest of carboxyamidomethylated peptide obtained after encapsulation (**A**) and crystallization (**B**). The corresponding peptides are reported.

Theoretical m/z	**Experimental m/z**		**Peptide sequence**
	A	**B**	
245.18	245.19	245.09	IL(-)

480.26	480.24	480.24	WFK
536.32	536.32	536.32	FLTR
982.59	982.48	982.58	(-)FVKWFKK

Also, as done in the case of the Ru complex, CD spectra (**Figure 1.27**) of hHFt/TRIL were collected. The spectra show that hHFt/TRIL possesses the same secondary structure of the untreated hHFt, thus indicating a correct protein refolding.

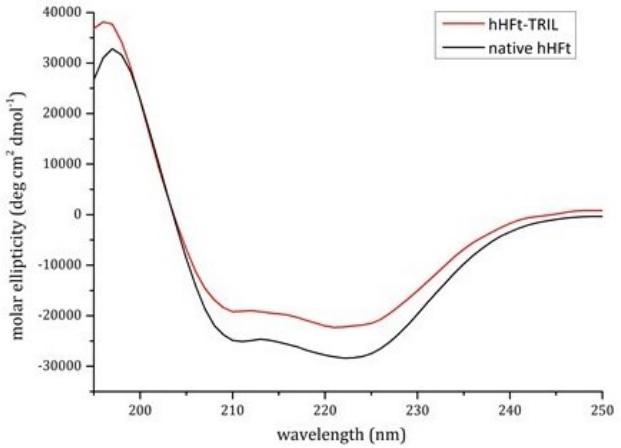

Figure 1.27. UV-vis spectra of reference hHFt (black line), and of hHFt/TRIL (red line). All the spectra were acquired in 20 mM Tris-HCl pH7.4.

Finally, to obtain a structural description of the hHFt/TRIL system, crystals were grown, and X-ray diffraction data were collected. The SDS-PAGE of the dissolved crystals (**Figure 1.28**, *panel A*) confirmed the presence of the peptide together with that of the ferritin subunit. Also

in this case, the band related to TRIL peptide was excised and analyzed by MALDI mass spectrometry (**Figure 1.28**, *panel B*; **Table 1.3**, above) reaching a total sequence coverage.

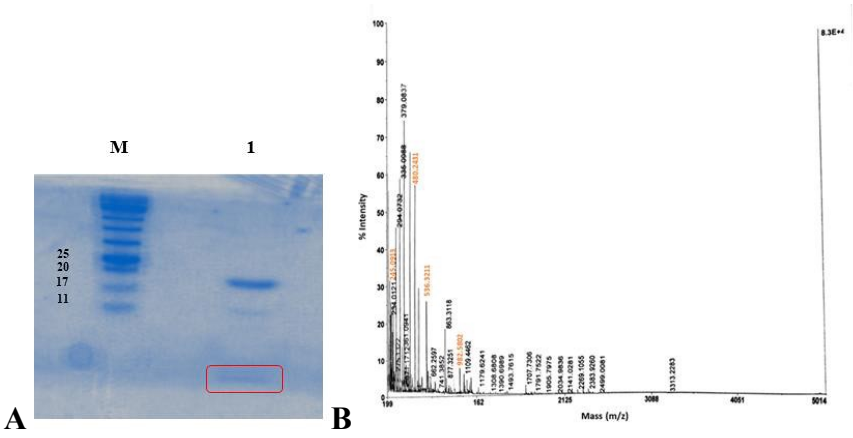

Figure 1.28. Assessment of the presence of TRIL in the dissolved crystal of hHFt/TRIL. *Panel A*: 15 % SDS-PAGE of the dissolved crystal (*lane 1*) showing the presence of the peptide (in red box) with the expected molecular weight; *Panel B*: MALDI mapping analysis of the red band excised from the gel. The spectrum shows the relative abundance of ions as a function of the mass/charge (m/z) ratio. In orange the signals corresponding to the peptide, whose attribution is reported in **Table 1.3**.

The crystals diffract X-rays to 2.3 Å resolution, *i.e.,* a resolution significantly lower than that of the Ru1-hHFt and hHFt$_{SDS}$ crystals that diffracted to 1.57 and 1.52 Å, respectively. The structure of hHFt/TRIL was solved and refined up to R-factor and R_{free} values of 0.171 and 0.223 (see **Table 1.6** in Materials and Methods section). Also in this case, the protein cage is perfectly reconstituted upon the encapsulation protocol

and the peptide is not visible in the electron density map. These findings indicate once again that the protein can correctly reassemble upon the SDS disassembly/reassembly protocol and suggest that the peptide does not simply interact with the outer protein nanocage surface.

3. Biological characterization of hHFt nanocomposite obtained with the new protocol

Based on the positive results observed upon loading Ru1 and TRIL inside hHFt cage by the new protocol based on the use of SDS, the following step was the evaluation of the effects of this treatment on the biological properties of the ferritin nanocage. The aim was to assess on one end the absence of toxicity of the empty nanocage, reconstituted upon disassembly in the presence of SDS and, on the other one, the effective capability to release the cargo in the cancer cells. As proof-of-the concept for the biological characterization the hHFt/TRIL system, previously described, has been chosen. The use on antimicrobial peptides as anticancer drug is indeed severely impaired by their absence of selectivity, which turns out into relevant side-effects, such as the haemolytic properties of Temporins

To verify if the encapsulation of TRIL is able to mask its toxicity to human cells, the haemolytic activity of the peptide was determined on human RBCs in comparison with its encapsulated form. The results reported in **Figure 1.28** indicate that the free peptide caused approximately 60% haemolysis at 64 μM (**Figure 1.28** blue bars) while encapsulation of TRIL in hHFt completely abolished its haemolytic capabilities (**Figure 1.28** red bar). Partial haemolysis could only be observed at the highest concentration tested (512 μM), but this effect was identical to that of the empty ferritin nanocages used as a control and was attributed to the empty nanoparticles ($hHFt_{SDS}$).

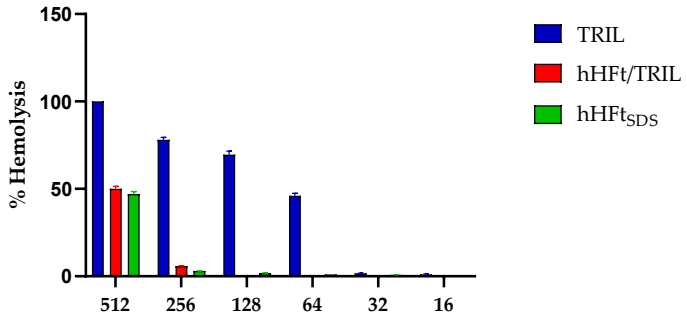

Figure1.28. Haemolytic activity of hHFt/TRIL against human red blood cells at different concentration. The peptide TRIL and $hHFt_{SDS}$ were used as control.

The potential antitumoral action of the hHFt/TRIL complex was determined by evaluating its toxicity on human MCF7 breast cancer cells

selected as suitable model since these cells show high levels of TfR1 expression owing to increased iron demand[52,53]. First, the possible toxic effect of both Ferritin in the free form (hHFt) and the empty ferritin nanocages upon disassembly by SDS and reassembly ($hHFt_{SDS}$) on cell viability was evaluated. MCF7 cultured cells were exposed for 24 hours to the either Ft or hHFt and the cell viability determined by estimation of living and dead cells through the trypan blue assay. Results reported in **Figure 1.29** clearly showed that both compounds were not able to induce cell death or to affect cell growth of MCF7 cells.

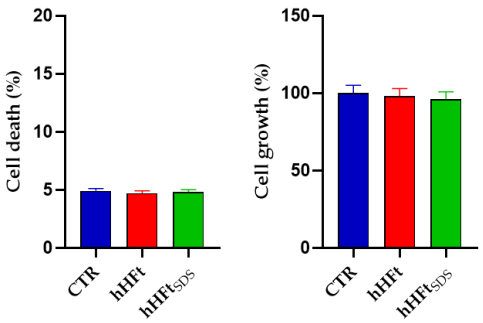

Figure 1.29. Evaluation of hHFt cytotoxicity in MCF7 cancer cells. The cell death/growth has been evaluated by Trypan blue assay in cells exposed for 24 hours to 2 μM original nanocage (hHFt) or 2 μM nanocage reconstituted after disassembly in the presence of 0.1 % SDS ($hHFt_{SDS}$). CTR represents untreated cells. Other experimental details are described in the Materials and Methods section. *** $p < 0.001$ versus CTR.

Since TRIL is endowed with both antibacterial and haemolytic activity, we tested its ability to affect cell viability in breast cancer cells and non-tumoral EA.hy926 endothelial cells. Human MCF7 and EA.hy926 endothelial cells were exposed to different TRIL concentrations (0, 2, 10, 20 μM) for 24 hours and the cell viability was evaluated by estimation of living and dead cells by the trypan blue assay (**Figure 1.30**). A marked toxicity was observed for TRIL 20 μM after 24 hours incubation with a strong increase of dead cells (2.5-fold) and a clear decrease of living cells (almost 70% reduction) while no effect was detected at lower TRIL concentrations (2 and 10 μM). However, similar results were also observed on non-tumoral endothelial cells indicating that TRIL exerted a non-specific effect on both cancer and normal cells. The toxic effect observed for TRIL on both cell line might be associated to its ability to disrupt cell membranes, being the positive charge of the peptide able to interact with the negatively charged phospholipids on the surface of cell membrane. Similar effects on MCF7 cells have also been reported for Temporin-derivate peptides at similar concentrations[50,52,54].

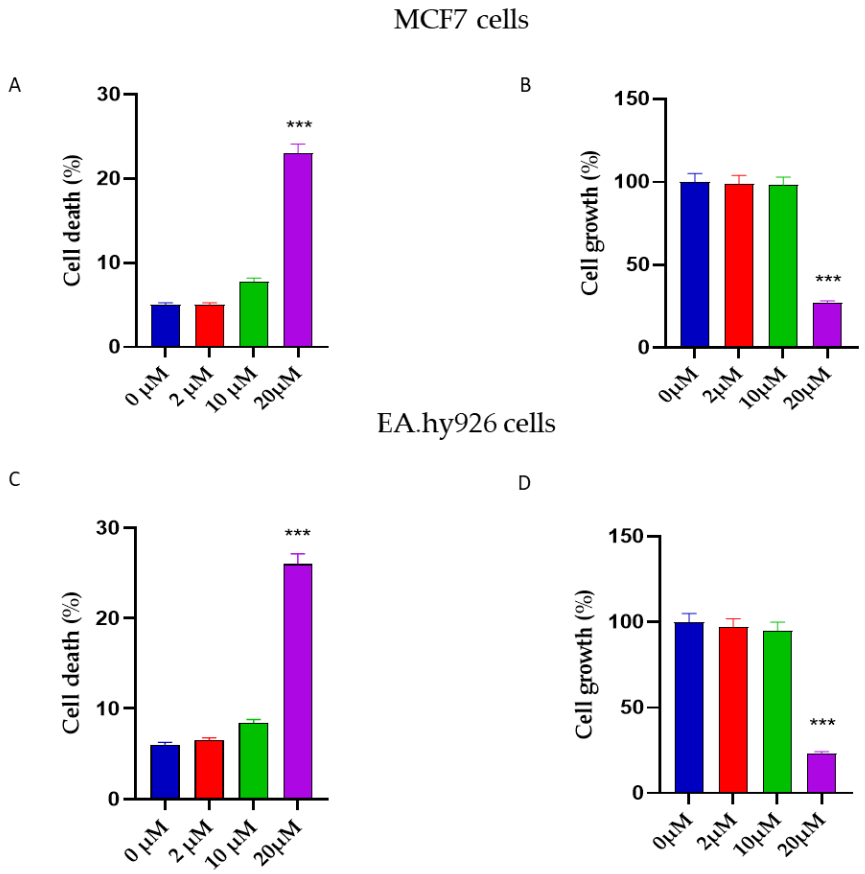

Figure 1.30. Evaluation of TRIL cytotoxicity in MCF7 cancer cells (panel **A-B**) and EA.hy926 endothelial cells **(**panel **C-D**). The cell death has been evaluated by Trypan blue assay in cells exposed for 24 hours to different concentrations of TRIL (0, 2, 10, 20 µM). Other experimental details are described in the Materials and Methods section. *** $p < 0.001$ versus CTR.

Next, we have explored the possible cytotoxic effect of encapsulated TRIL (hHFt/TRIL) on both MCF7 cancer cells and non-tumoral EA.hy926 endothelial cells in comparison with the empty nanocages ($hHFt_{SDS}$). **Figure 1.31** shows the cell viability tested at 5- and 24-hour

incubation with each compound at a 2 μM concentration and evaluated by the estimation of cell death/growth by trypan blue assay. Differently to the free TRIL peptide, its encapsulated form of the peptide showed a clear toxic effect only on the MCF7 cancer cells, with a 45% decrease of living cells and an almost 4-fold increase of dead cells compared to the control, while no effect could be detected on EA.hy926 endothelial cells. Finally, incubation with the empty nanocages ($hHFt_{SDS}$) did not affect cell growth and cell death of both cell lines compared to control.

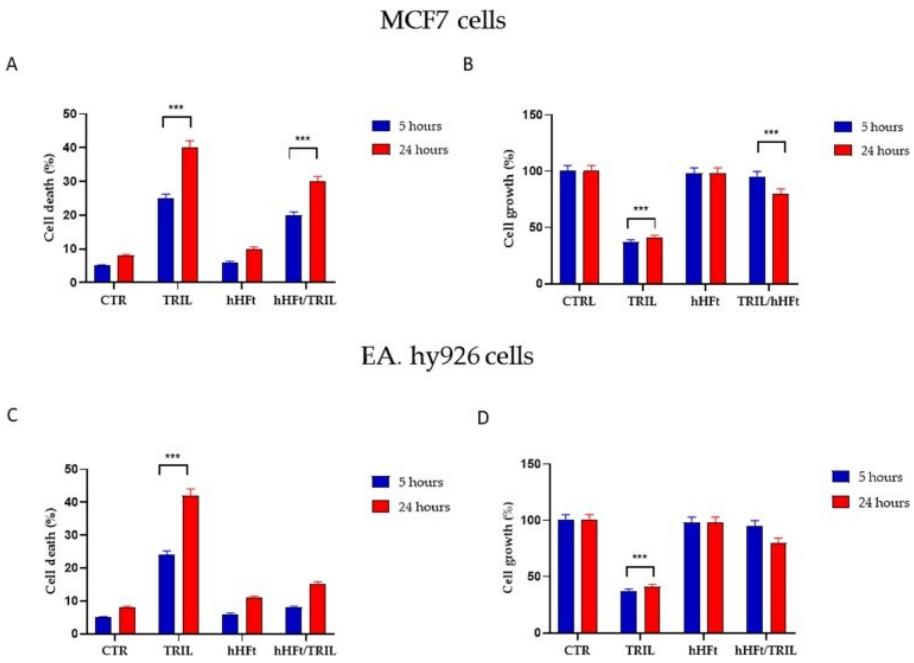

Figure 1.31. Effect of cytotoxicity in MCF7 cancer cells (panel **A-B**) and EA.hy926 human endothelial cells (panel **C-D**). The cell growth/death has been evaluated by Trypan blue assay in cells exposed for 5 and 24 hours to different treatments. CTR:

untreated cells; TRIL: incubated with 20 μM TRIL; hHFt: incubated with 2 μM hHFt; hHFt/TRIL: incubated with 2 μM hHFt/TRIL. Other experimental details are described in the Materials and Methods section. *** $p < 0.001$ versus CTR.

The overall data suggest that the free peptide clearly affect cell toxicity and growth in both tumoral and non-tumoral cell lines as showing no specificity for MCFT cells, while no effect whatsoever was observed when either tumoral or non-tumoral cell lines were incubated with the empty nanocage ($hHFt_{SDS}$). On the contrary, hHFt/TRIL seems highly selective for MCF7 tumoral cells, while no toxic effect was observed on EA.hy926 endothelial cells. This specific antitumoral activity of the encapsulated TRIL could be ascribed to the higher number of TfR1 receptors located on the tumoral cell membrane that mediate a higher affinity of hHFt for MCF7 cancer cells. This binding seems to be harmless for the empty nanocage but very toxic when the nanocage is carrying the peptide. In this respect, the nanocage could play a dual role, as it is able to protect non tumoral cells from the toxic effects of free TRIL peptide and selectively carry the cargo peptide across the cell membrane of tumoral cells.

Recently several reports have suggested that the oxidative stress induced by antimicrobial peptides might be responsible for their cytotoxic effects on cancer cells. Tigerinins and Nisin were shown to generate reactive

oxygen species (ROS) and induce oxidative stress damages in tumour cells[55,56]. We were then stimulated to investigate whether oxidative stress might play an important role in the death induced by TRIL and hHFt/TRIL on tumour cells. ROS production in cancer cells exposed to TRIL, $hHFt_{SDS}$, and hHFt/TRIL was monitored by using the redox-sensitive fluorescent dye DCFH-DA[53]. MCF7 cells were exposed for 24 hours to TRIL 20 μM, or 2 μM of $hHFt_{SDS}$ and hHFt/TRIL and to 1 mM H_2O_2 as positive control. **Figure 1.32** shows the effect of the various compounds on the production of intracellular ROS. Exposure to TRIL and hHFt/TRIL for 24 hours led to a significant increase (7-8-fold) in intracellular ROS production in cancer cells compared to control cells (**Figure 1.32 A**). This behaviour is very similar to MCF7 cells treated with H_2O_2 a well know inducer of oxidative stress that showed an almost identical increase in the ROS level. Differently, no increase in ROS production is observed in EA.hy926 cells when exposed to hHFt/TRIL and hHFt and this is consistent with the absence of toxicity observed in this cell line (**Figure 1.32 B**). At the same time, TRIL promotes ROS production also in endothelial cells. No increase in ROS production was observed in cells exposed to hHFt thus confirming the absence of toxicity

for the empty nanocage, even after the SDS-based disassembly and reassembly process.

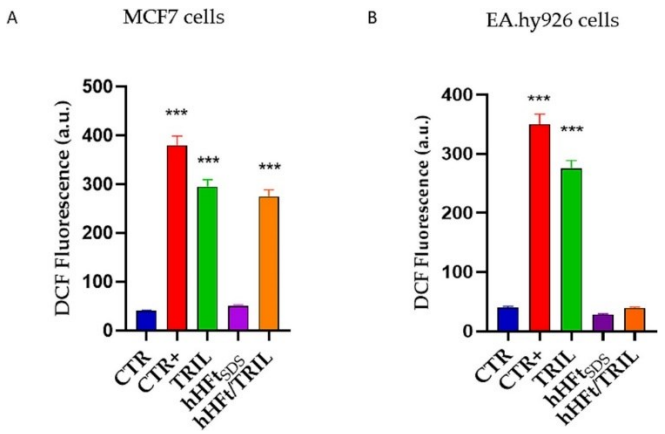

Figure 1.32. Effect of TRIL and hHFt/TRIL on ROS production in cancer cells MCF7 (panel A) and EA.hy926 (panel B) cells. Levels of ROS were evaluated by the DCFH-DA assay as described in Material and methods section. Mcf7 were exposed to different treatments for 24 hours. CTR: untreated cells; CTR+: cells treated with 1 mM H_2O_2; TRIL: incubated with 20 µM TRIL; $hHFt_{SDS}$: incubated with 2µM hHFt upon disassembly and reassembly; hHFt/TRIL: 2µM. Other experimental conditions are described in the Materials and methods section. *** $p < 0.001$ versus CTR.

Although further studies will be needed to better clarify the molecular mechanisms underlying the cytotoxicity induced by TRIL and hHFt/TRIL, these data suggest that oxidative stress might play an important role in mediating their toxicity mechanism in cancer cells. However, it should be underlined that ROS production might either be the triggering factor or the final event in the cell death induced by TRIL

and hHFt/TRIL. The evaluation of ROS levels in cultured cells has never been performed for Temporin peptides and the results observed for TRIL might then be useful to rationalize the toxic effect of Temporin and Temporin-like peptides on cancer cells.

Hereby, a new disassembly/reassembly procedure has been developed and compared with the one already reported in literature. The comparison underlined, the relevant drawbacks of the currently available protocols. For instance, when the protein disassembly is achieved by exposure to extreme pH (either acidic or alkaline) the final protein recovery and homogeneity are not satisfactory. On the contrary, the new protocol allows the quantitative disassembly and the high-yield recovery of hHFt nanocages whose structural properties are identical to those of the untreated form. The new protocol was also applied to load two small molecules within the protein nanocage, since drug encapsulation in hHFt can have significant advantages, *i.e.,* it increases the solubility of the small molecules in aqueous media and/or their thermal stability, decreases the immunogenicity, allows a selective targeting towards tumor cells, and prevents other possible side effects of the drug. Using Ru1 as model, it was possible to demonstrate that the SDS-based protocol allows the encapsulation of metal complexes within hHFt

nanocage. The encapsulation of TRIL, a 13-residue antimicrobial peptide, was also performed, demonstrating that polypeptides can also be loaded within the nanocage obtaining nanoparticles amenable for further structural and functional studies. In both cases the obtained nanocomposites have been analyzed by means of different techniques confirming an efficient encapsulation. To remove the residual SDS, alternating steps of ultrafiltration and dilution with pure buffer, using *Centricon* tubes with cut-off 100.000 Da, were used. This procedure allows an easy and quantitative control of the protein recovery. However, single protein subunits or aggregated forms with a molecular size below 100.000 Da could be lost during the ultrafiltration procedure. Moreover, the reduction of the SDS concentration below 0.1% can be achieved also by means of an extensive dialysis against the pure buffer. This procedure can be useful when big volumes of buffer are required to allow the reassembly. As a matter of fact, the dialysis was applied only to reassemble the hHFt disassembled in the presence of the highest SDS concentrations. Notably, despite the extensive wash of the reassembled nanocages with pure buffer, it cannot be excluded the presence of traces of SDS (below 0.01%) trapped in the bulk inside the cages. However, no SDS was detected in both X-ray and NMR studies of hHFt reconstituted

after disassembly and reassembly, and the reconstituted, empty nanocages was not toxic for cells viability. More interesting, the hHFt shell endows hHFt/TRIL complex with a selective cytotoxic activity against MCF7 tumoral cells without affecting EA.hy926 endothelial cells, while the free form of TRIL peptide was unable to distinguish between tumour and non-tumour cells as it displays the same cytotoxic effect against both cell types. The toxicity of the positively charged peptide on both cell lines might be associated to its ability to interact with the negatively charged phospholipids on the cell thus disrupting the cell membranes. On the contrary, the encapsulated form of the peptide is selectively addressed to cancer cells. Notably, while the toxicity of the free peptide is mediated by a destructive interaction with the external membrane of different cellular lines, the hHFt nanocage carries the peptide inside the tumour cell through a receptor-mediated endocytosis mechanism, inducing the cellular death by a different route, while assuring a specificity for malignant cells.

MATERIALS AND METHODS

1. Materials

The horse spleen ferritin and Auranofin were purchased by Sigma Aldrich and used without further purification. [Ru (bipyridyl)$_3$]$^{2+}$ metal complex (Ru1) was kindly provided by Professor Paola Manini (Department of Chemical Sciences, University of Naples Federico II) and the 13- residue antimicrobial peptide dubbed (FVKWFKKFLTRIL), an analogue of Temporin-L[57] was purchased from BioFab Research.

2. Expression of human H chain ferritin

Human H-chain ferritin was expressed in *E. coli* BL21(DE3). Bacterial cells were transformed with plasmid pET22b+ transferring the gene encoding for the protein. Cells were cultured on LB/Agar containing ampicillin (Amp) 100 mg L-1 over night at 37 °C. Afterwards, a single colony was resuspended in LB medium with the same antibiotic overnight at 37 °C, then the starter culture was diluted 1:100 (v/v) into LB/Amp and incubated at 37 °C. Protein expression was induced at 0.8 OD_{600}/mL by adding IPTG 0.4 mM and carried for 3 hours at 37 °C.

Finally, the cells were harvested by centrifugation (4 °C, 8000 rpm, 30'), washed with pure water and stored frozen until protein purification.

3. Purification of human H-chain ferritin

To extract and purify the protein, cells were resuspended in TRIS-HCl 20 mM at pH 7.4 and sonicated on ice, after the addition of anti-protease agents (anti protease Cocktail, Sigma Aldrich, one tablet per 30 mL) with a Microson Ultrasonic Homogenizer XL2000 for 30' (30'' on 30'' off). Since these proteins are soluble and very stable thermally, after sonication, the supernatant was heated at 75 °C for 10 min and centrifuged (4 °C, 12 000 rpm, 30') to remove the precipitated proteins. After that, the solution containing protein, was incubated with 75 μg/mL of DNase and RNase solutions (Sigma Aldrich) for 30' at 37 °C, centrifuged and loaded on a DEAE anionic exchange column pre-equilibrated with 20 mM Tris-HCl pH 7.4. The column was eluted with a linear gradient of NaCl (0–1.0 M) in the same buffer at a flow rate of 1.0 mL/min. The chromatography was monitored by UV absorbance at 280 nm. The fractions containing proteins were pooled and loaded on Sepharose 6B column (2.5 × 24 cm) equilibrated and eluted with TRIS-HCl 20 mM at pH 7.4. Then, the fractions containing the assembled hHFt

nanocages were concentrated by ultrafiltration (cut-off 100.000 Da) and stored ad 4 °C. Purity of hHFt was assessed by SDS Polyacrylamide Gel Electrophoresis. Protein yield was estimated by UV absorbance at 280 nm and corresponds to about 25 mg per liter of LB medium.

4. Disassembly/assembly protocols

Auranofin encapsulation

Encapsulation of AF inside the Ft cages was obtained by first disassembling both Fts into subunits at pH 13 by gently adding 2.0 M NaOH, and then reconstituting them at neutral pH by using 1.0 M sodium phosphate buffer pH 7.4 for $_{AF}$hsFt and 1.0 M Tris HCl pH 7.4 for $_{AF}$hHFt. Specifically, protein samples of concentration 20 mg mL^{-1} dissociated at pH 13 were incubated in the presence of AF in a protein chain to metallodrug molar ratio of 1:20 for 1h under stirring. After incubation, the pH was raised to the physiological value to let the cages reassemble. After half an hour, samples were centrifuged for 10 min at 5000 rpm to remove possible precipitates, then ultracentrifuged at 10.000 rpm on *Centricon* filters (cut-off 50.000 Da), to remove the unbound drug, and washed with 10 mM sodium phosphate buffer pH 7.4 and 20

mM Tris HCl pH 7.4, respectively. Fts concentrations were determined with the BCA protein assay (BCATM Protein Assay Kit, Pierce)[58].

SDS-based encapsulation protocol

The purified hHFt was disassembled by SDS treatment. The optimization of the protocol is reported in the Results section. To allow the reassembly, the SDS concentration was decreased below 0.01% using two different approaches, *i.e.,* by alternating steps of ultrafiltration and dilution with pure buffer or by extensive dialysis, as described in detail in the Results section. For comparison, disassembly/reassembly protocols following literature procedures based on pH switch were also applied[35,59], starting from four identical aliquots of hHFt (0.5 mg/mL, 1 mL). Briefly, the pH of two aliquots was slowly adjusted to 1.5 or 2.0 by gentle addition of 0.1 M HCl ($hHFt_{pH2->7.4}$) and the pH of the two remaining was slowly adjusted to 12.0 or 13.0 by gentle addition of 0.1 M NaOH ($hHFt_{pH13->7.4}$). The four solutions were incubated for 2 h at room temperature, then the pH was restored to 7.4 by 30 times dilution with 20 mM Tris-HCl pH 7.4. After incubation overnight at 4°C to allow the reassembly, the samples were concentrated by ultrafiltration on *Centricon* tubes (cut-off 100.000 Da). Assembly and disassembly states of hHFt samples were evaluated by non-denaturing (native) PAGE on a

6% polyacrylamide gel for the separation, using 25 mM Tris/glycine pH 8.4 as running buffer[60]. The gels were run for 3.5 h at a constant voltage of 100 V, at 4°C. Coomassie Brilliant Blue G-250 was used as staining agent.

The disassembly/reassembly protocol was applied to encapsulate Ru1 and TRIL.

Ru1 and TRIL encapsulation

For the ruthenium compound, 800 µL of Ru1 solution (1 mM in 20 mM Tris-HCl pH 7.4) were added to 2 mg of hHFt (0.5 mg/mL, 4 mL, dissolved in the same buffer) dissociated in the presence of 0.1% SDS ($hHFt_{SDS}$), according to the protocol optimized as reported in the Results section. The mixture was stirred for 30 min at room temperature (RT), then the sample was diluted 10 times with the buffer (20 mM Tris-HCl pH 7.4) to decrease the SDS concentration, and the solution was incubated at 4°C overnight. Free Ru1 and residual SDS were removed by ultrafiltration on *Centricon* tubes with cut-off of 100.000 Da and extensive washing with Tris-HCl buffer up to a final volume of 550 µL. The protein concentration before and after the treatments was assessed by using the Bradford assay kit (Sigma), using BSA as a standard[58].

For the encapsulation of the peptide, a slightly different procedure was adopted, using a higher protein concentration in the dissociation step and a 1/1 cargo/ferritin subunit molar ratio. 180 μL of a TRIL solution (2.0 mg/mL, equivalent to 1.2 mM, dissolved in 20 mM Tris- HCl pH 7.4) were added to 5.6 mg of hHFt (11.2 mg/mL, 500 μL) disassembled with 0.1% SDS, as previously described, and incubated overnight at RT. The solution was diluted 10 times with 20 mM Tris- HCl at pH 7.4 and incubated overnight at 4 °C to allow the reassembly. The protein solution was concentrated by ultrafiltration using *Centricon* tubes with cut-off 100.000 Da and extensively washed with the buffer to remove any residual trace of SDS and the free peptide. Also in this case, the aggregation state of the nanocages reassembled in the presence of TRIL (hHFt/TRIL) was assessed by native PAGE. The presence of the peptide in the high molecular weight fraction (*i.e.,* > 100.000) was assessed by SDS-PAGE and mass spectrometry, as described below.

5. Spectroscopic characterization

UV-vis absorption spectra of $_{AF}$hsFt and $_{AF}$hHFt were recorded using a 0.1 cm optical path-length quartz cell on a JASCO V-560 UV-vis spectrophotometer in the range of 240–700 nm, using a protein

concentration of 0.25 mg mL^{-1} in 10 mM sodium phosphate buffer pH 7.4 and 20 mM Tris HCl pH 7.4, respectively. Other experimental parameters were bandwidth 2.0 nm, scanning speed 200 nm min^{-1} and data pitch 1.0 nm.

Far-UV CD spectra were recorded on a Jasco J-715 spectropolarimeter equipped with a Peltier thermostatic cell holder (Model PTC-348WI) in the range of 190–250 nm, using protein concentration of 0.05–0.03 mg mL^{-1} in 10 mM sodium phosphate buffer pH 7.4 and 20 mM Tris HCl pH 7.4, and a 0.1 cm path length quartz cuvette. Each spectrum was obtained by averaging three scans and converting the signal to mean residue ellipticity in units of deg cm^2 $dmol^{-1}$. Other experimental settings were scanning speed 50 nm min^{-1}, bandwidth 2.0 nm, resolution 1.0 nm, sensitivity 50 mdeg and response 2 s.

6. NMR spectroscopy

For the acquisition of the NMR spectra, hHFt samples were at concentration of 1.5 mg/mL and the addition of 10% (v/v) of D2O to the final solution of 500 µL. 1D, 2D (1H-1H-TOCSY and 1H-1H-NOESY), and pseudo-2D diffusion ordered spectroscopy (DOSY) experiments were recorded at 25 ◦C on a Bruker Avance 600 MHz spectrometer

equipped with a 5 mm triple resonance 1H, 13C and 15N, z-axis pulsed-field gradient probe head. For 1D 1H experiments, the water signal was suppressed using the excitation sculpting gradient pulse (zgesgp)[61], using a D1 of 2 s, 64 scans, and a spectral width of 12 ppm. All the spectra were transformed and visualized in TopSpin 4.0.9 (Bruker Biospin). For pseudo-2D DOSY spectra, we used a sequence of stimulated echo bipolar pulse field gradient that incorporates the solvent suppression with WATERGATE (stebpgp1s19)[62]. A total of 32 spectra with gradient strengths ranging from 2% to 98% of the maximum value were recorded. A diffusion time Δ of 60 ms and gradient length δ of 1.0 ms were used in all the experiments. The spectra were analyzed using TopSpin Dynamics Center (Bruker, Fällanden, Switzerland). The diffusion values were obtained by fitting the peak intensity decays using the Stejskal-Tanner equation[63].

7. ICP-AES Measurements

Auranofin-loaded ferritins

The determination of metal concentration in the $_{AF}$hsFt and $_{AF}$hHFt nanocages was performed using a Varian 720-ES inductively coupled plasma-atomic emission spectrometer equipped with a CETAC U5000

AT+ ultrasonic nebulizer, in order to increase the method sensitivity. An amount of 200 µL of each sample was used. The samples were transferred into polyethylene vials and digested in a thermo-reactor at 80 °C for 8 h with 2 mL of HNO_3 69.5% suprapure grade. Ultrapure water (≤18 MΩ) was added to the vials containing the $_{AF}$hsFt and $_{AF}$hHFt solutions until a final volume of 6 mL. All the samples were spiked with 1 ppm of Ge used as an internal standard and analyzed. Calibration standards were prepared by gravimetric serial dilution from a commercial standard solution of Au at 1000 mg L^{-1}. The following wavelengths were used: 242.795 and 267.595 nm for Au and 209.426 nm for Ge. The operating conditions were optimized to obtain maximum signal intensity, and between each sample, a rinsed solution of 2.0 mL of HNO_3 69.5% suprapure grade and 4.0 mL of ultrapure water was used to avoid any "memory effect".

Ru1-loaded ferritin

The amount of Ru1 encapsulated within hHFt was before estimated by the absorbance at 452 nm, using a molar extinction coefficient of 1.46×10^4 (M^{-1} cm^{-1})[46] and then measured by multi-element analysis performed by the Inductively Coupled Plasma - Mass Spectrometer

(ICP-MS Aurora M90, Bruker, Germany) conducted at the laboratory of Analytical Chemistry for the Environment of the University of Naples Federico II. Nitric acid (HNO_3, 69% v/v Ultratrace$^{@}$ ppb-trace analysis grade) was provided by Scharlau (Barcelona, Spain). Multi-component solution of 30 elements (10 mg/L each one) was of ultrapure grade for ICP, TraceCERT® and was purchased by Merck (Darmstadt, Germany); ruthenium solution (1,000 mg/L) was of ultrapure grade for ICP, TraceCERT® and was purchased by ROMIL. The analysis was performed in Normal Sensitivity mode. All standards used for analysis in ICP-MS were prepared in HNO_3 solution (2%, v/v). The internal standards were ^{89}Y and ^{115}In for both calibration curve and sample analysis. All the analyses were performed as triplicates.

8. MALDI spectra

A MALDI Voyager-DE STR spectrometer from Applied Biosystems was used for the acquisition of MALDI spectra. The sample co-crystallizes with an excess of matrix, α-cyano-4- hydroxycinnamic acid, equal to 10 mg/mL on a metallic support and it is ionized by a laser pulse (λ = 337 nm) in the MALDI source. The analysis was performed in positive mode

using the TOF analyzer in reflection mode and a mass range of 200–5,000 m/z.

9. Transmission electron microscopy (TEM) analysis

Samples for TEM analysis were prepared by placing a drop of a protein solution (typical concentration 0.5 mg mL^{-1}) on a carbon- coated copper TEM grid and allowing the solvent (water) to evaporate. To enhance the contrast, negative staining with 1.5% phosphotungstic acid (PTA) solution at pH 7.0 was carried out by depositing a drop of PTA solution on the grid containing the sample for 4 min (contact between sample and PTA) and then the excess fluid was drained off with filter paper. The grid was allowed to dry, and images were collected using a FEI TECNAI G2 S-twin apparatus operating at 120 kV (LaB6 source).

10. Crystallization, X-ray Diffraction Data Collection, Structure Solution and Refinement

Crystals of $_{AF}$hsFt were grown through the hanging drop vapor diffusion method using a reservoir solution of 0.6–0.8 M $(NH_4)_2SO_4$, 0.1 M Tris HCl pH 7.4–7.7, 50–60 mM $CdSO_4$ and protein concentration of 7.0 mg

mL^{-1}. Crystals of $_{AF}$hHFt, hHFt restored after the SDS dissociation ($hHFt_{SDS,}$), Ru1-hHFt and hHFt/TRIL systems were grown using the same method and a reservoir solution containing 2.0 M $MgCl_2$ and 0.1 M Bicine buffer pH 9.0, and a protein concentration of 19.0 mg mL^{-1} ($_{AF}$hHFt) and 5.0-10.0 mg mL^{-1}. Diffraction data were registered at 100 K at the XRD2 beamline of Elettra synchrotron, Trieste, Italy, using λ = 1.00 Å, at 1.24 and 1.17 Å resolution on crystals of $_{AF}$hsFt and $_{AF}$hHFt, respectively, and to 1.52, 1.57, and 2.30 Å resolution for the $hHFt_{SDS}$, Ru1-hHFt and hHFt/TRIL systems obtained in SDS. Crystals were cryoprotected using a solution of the reservoir with 25% glycerol. Data were indexed, integrated, and scaled using Autoproc[64]. Data collection statistics are reported in **Tables 1.5** and **1.6**. The phase problem was solved by molecular replacement using the ferritin structures deposited in the PDB under the accession codes 5ERK[35] for hsFt and 5N27[38] for hHFt as the starting models. The crystals belong to the space group F432, with one Ft chain in the asymmetric unit. The structures refine to R-factor and R_{free} values are reported in the tables of statistics (**Table 1.5-1.6**). Several rounds of restrained energy minimization and individual or mixed anisotropic/isotropic B-factor refinements were carried out using Refmac5[65]. Refinement cycles were followed by manual intervention

based on observation of the electron density map carried out using Coot[66]. Refinement statistics are reported in **Table 1.5-1.6**. Model geometry was validated using the PDB validation server. Figures with electron density maps were drawn with PyMOL (DeLano Scientific LLC, San Carlos, CA, USA). X-ray structures of $_{AF}$hsFt and $_{AF}$hHFt were deposited in the PDB under the accession codes 8B7L and 8B7O, respectively, and 8A5N, 8A2M and 8A2L for hHFt$_{SDS,}$ Ru1-hHFt and hHFt/TRIL.

Table 1.5. Data collection and refinement statistics of $_{AF}$hsFt and $_{AF}$hHFt.

Data collection statistics		
Protein	$_{AF}$hHFt	$_{AF}$hsFt
PDB code	8B7O	8B7L
Space group	F432	F432
Unit cell parameters a, b, c (Å)	180.03	181.99
Molecules in the asymmetric unit	1	1
Observed reflections	6523319 (300927)	5410903 (265838)
Unique reflections	90295 (4445)	73628 (3593)
Resolution (Å)	46.01-1.17 (1.19-1.17)	64.34-1.24 (1.26-1.24)
Completeness (%)	100.0 (100.0)	100.0 (100.0)
Rmerge	0.156 (3.112)	0.122 (3.122)
Rpim	0.018 (0.378)	0.014 (0.364)
Rmeas	0.157 (3.135)	0.123 (3.1444)
I/I(σ)	26.6 (2.1)	34.9 (2.1)

Multiplicity	72.2 (67.7)	73.5 (74.0)
$CC_{1/2}$	1.000 (0.777)	1.000 (0.777)
Refinement statistics		
Resolution (Å)	46.01-1.17	64.34-1.24
N° reflection (working set)	85177	84436
N° reflection (test set)	4431	4449
N° non-H atoms (refinement)	20630	1964
R-factor/R_{free}	0.150/0.166	0.160-0.180
r.m.s.d. from ideality		
r.m.s.d. bonds	0.017	0.020
r.m.s.d. angles (°)	2.14	2.24
Ramachandran values (%)		
Most favored	98.28	96.08
Outliers	0.00	0.00

†Rmerge= Σ hΣi |I(h,i)-<I(h)>|/ Σ hΣi I(h,i), where I(h,i) is the intensity of the ith measurement of reflection h and <I(h)> is the mean value of the intensity of reflection h. Criteria used in determination of resolution cut: Rpim <= 0.6000; I/σI >= 2.00; $CC_{(1/2)}$ >= 0.3000
* Values in parenthesis refer to highest resolution shell

Table 1.6. Data collection and refinement statistics of $hHFt_{SDS,}$ Ru1-hHFt and hHFt/TRIL.

Data collection statistics			
Protein	$hHFt_{SDS,}$	Ru1-hHFt	hHFt/TRIL
PDB code	8A5N	8A2M	8A2L
Space group	F432	F432	F432
Unit cell parameters a, b, c (Å)	183.9	193.77	193.06
Molecules in the asymmetric unit	1	1	1

Observed reflections	5748728 (294577)	254356 (120863)	1695326 (83457)
Unique reflections	41264 (2030)	37411 (1836)	12141 (607)
Resolution (Å)	1006.18-152 (1.552-152)	106.10-1.57 (1.59-1.57)	105.69-2.30 (2.34-2.30)
Completeness (%)	99.5 (100.0)	99.4 (100.0)	99.9 (100.0)
Rmerge	0.185 (4.027)	0.248 (3.076)	0.709 (4.363)
Rpim	0.016 (0.334)	0.030 (0.380)	0.059 (0.371)
Rmeas	0.185 (4.040)	0.250 (3.099)	0.711 (4.379)
I/I(σ)	41.2 (2.4)	15.0 (2.1)	13.0 (2.2)
Multiplicity	193.3 (145.1)	68.8 (65.8)	139.6 (137.5)
$CC_{1/2}$	1.00 (0.859)	0.998 (0.846)	0.998 (0.827)
Refinement statistics			
Resolution (Å)	106.18-1.52	105.69-1.57	105.69-2.30
N° reflection (working set)	2056	2571	829
N° reflection (test set)	153	137	603
N° non-H atoms (refinement)	1920	1848	1635
R-factor/R_{free}	0.153/0.190	0.161/0.190	0.171/0.223
r.m.s.d. from ideality			
r.m.s.d. bonds	0.013	0.013	0.013
r.m.s.d. angles (°)	1.64	1.63	1.64
Ramachandran values (%)			
Most favoured	96.45	96.69	96.21
Outliers	1	1	1

†Rmerge= Σ hΣi |I(h,i)-<I(h)>|/ Σ hΣi I(h,i), where I(h,i) is the intensity of the i^{th} measurement of reflection h and <I(h)> is the mean value of the intensity of reflection

h. Criteria used in determination of resolution cut: Rpim <= 0.6000; I/σI >= 2.00; $CC_{(1/2)}$ >= 0.3000
* Values in parenthesis refer to highest resolution shell

11. Cytotoxicity Experiments

Auranofin-loaded ferritins

Immortalized human keratinocytes (HaCaT) were from Innoprot (Biscay, Spain) and human epidermoid carcinoma cells (A431 cells) were obtained from ATCC. Cells were cultured in Dulbecco's modified Eagle's medium (DMEM) (Sigma-Aldrich, St Louis, MO, USA), supplemented with 10% fetal bovine serum (HyClone), 2 mM L-glutamine and antibiotics (Sigma-Aldrich), under a 5% CO_2 humidified atmosphere at 37 °C. For cytotoxic analyses, cells were seeded in 96-well plates at a density of 2.5×10^3 cells per well. Then, 24 h after seeding, increasing concentrations of AF, $_{AF}$hHFt and $_{AF}$hsFt were added to the cells. After 48 h incubation, cell viability was assessed via the MTT (3-(4,5-dimethylthiazol-2-yl)-2,5-diphenyltetrazolium bromide) assay[39].

TRIL-loaded ferritin

Human MCF7 breast cancer cells (HTB-22) and human endothelial EA.hy926 cells (CRL-2922) were purchased by ATCC (Virginia, USA) and cultured in Dulbecco's Minimum Essential Medium (DMEM)

(AL007, Microgem) supplemented with 10% FBS, 2.0 mM glutamine (X0550, Microgem), 100 units/mL penicillin and 100 mg/mL streptomycin (A001, Himedia) in a 5.0% CO_2 humidified environment at 37 °C. Cells were grown for 18 hours before treatments.

To determine the number of dead cells in the experimental groups, Trypan Blue assay was employed. Trypan Blue is a cell membrane-impermeable dye and, therefore, its presence inside the cells is due to damaged membranes. Upon the entry into the cells, Trypan Blue renders the cells dark blue. Briefly, cells were seeded in 10% FBS-containing medium in a 6-well plate at a density of $6x10^5$ cell/well for 18 h at 37 °C and then treated as above described. After 24 h of treatment, cells were collected, and cell counting was performed by mixing 10 µL of cell suspension with an equal volume of Trypan Blue (0.4%, v/v). The number of blue stained cells (dead cells), also not-stained cells (viable cells) were counted. Trypan Blue experiments were performed three times (in replicates of six wells for each data point in each experiment). Data are presented as means ± standard deviation for a representative experiment.

12. Oxidative Stress Analysis

Auranofin-loaded ferritins

To estimate ROS production, the protocol described by Petruk[67] was followed. Briefly, HaCaT and A431 cells were incubated with AF and $_{AF}$hHFt for different lengths of time (1–48 h) and then incubated with 2',7'-dichlorodihydrofluorescein diacetate (H_2-DCFDA, Sigma-Aldrich). Fluorescence intensity was measured using a PerkinElmer LS50 spectrofluorometer (525 nm emission wavelength, 488 nm excitation wavelength, 300 nm min^{-1} scanning speed and 5 nm slit width for both excitation and emission). ROS production was expressed as a percentage of DCF fluorescence intensity of the sample under test, with respect to the untreated sample. Each value was assessed by three independent experiments, each with three determinations. Significance was determined by Student's t-test.

The variation in the mitochondrial membrane potential ($\Delta\psi m$) was measured as described by Monti *et al.*[40]. Cells were plated at a density of 2×10^4 cells per well and were treated after 2, 4, 8, 16 and 24 h, as described above. Subsequently, the cells were incubated with 200 nM cationic lipophilic dye tetramethylrhodamine ethyl ester (TMRE) for 20 min at 37 °C. Then, the cells were gently washed with 0.2% BSA in PBS

three times and the fluorescence was measured in a microplate reader with peak Ex/Em = 549/575 nm. Each value is the mean of three independent experiments, with three measurements for each experiment. Significance was determined by Student's t-test.

TRIL-loaded ferritin

Intracellular ROS were detected by means of an oxidation-sensitive fluorescent probe 2',7'-dichlorofluorescin diacetate (DCFH-DA)[53]. Cells were grown in 12-well plates, pre-incubated with DCFH-DA for 30 min before treatment. Control experiments were performed using untreated cells and cells exposed to a 1 mM H_2O_2. After incubation, cells were washed twice with PBS buffer and then lysed with Tris-HCl 0.5 M, pH 7.6, 1% SDS. The non-fluorescent DCFH-DA is converted, by oxidation, to the fluorescent molecule 2',7'-dichlorofluorescein (DCF). DCF fluorescence intensity was quantified on a Perkin Elmer Life Sciences LS 55 spectrofluorometer using an ex-citation wavelength of 488 nm and an emission wavelength of 530 nm. Data are expressed as average ±S.D. from three independent experiments carried out in triplicate.

13. Minimum inhibitory concentration

The antibacterial activity of TRIL was tested against the reference strain *E. coli BL21*. Minimum inhibitory concentration (MIC) values were determined using a broth microdilution susceptibility test. Serial two-fold dilutions of hHFt/TRIL, $hHFt_{SDS}$, and standard TRIL from 300 to 0 μM were prepared (final volume of 50 μl) in 96-well polypropylene microtiter plates with LB broth. In a control experiments, the MIC of the peptide recovered hHFt/TRIL was also measured by the same test. Each dilution series included control wells without peptide. A total of 50 μl of the adjusted inoculum (approximately 5×10^5 cells/ml in MH broth) was added to each well. The MIC was taken as the lowest concentration of antimicrobial peptide resulting in the complete inhibition of visible growth after 24 h of incubation at 37 °C.

14. Haemolytic assays

The *in vitro* haemolytic activity of TRIL on human erythrocytes taken from a healthy donor was determined by monitoring the haemoglobin release at 540 nm in the plasma. All experimental protocols were approved by the Research Ethics Review Board of UAEU and informed

consent was obtained from donor. Aliquot of 4% erythrocyte suspension in PBS 1X were incubated at 37 °C for 60 min with serial two-fold dilutions of hHFt/TRIL, $hHFt_{SDS}$ and standard TRIL from 512 to 16 μM were prepared (final volume of 100 μl) in 96-well polypropylene microtiter plates. 100% haemolysis was determined by addition of Triton X-100 at 0.1% final concentration (positive control), 0% haemolysis was determined by addition of PBS 1X (negative control). The reduced haemolyticity of TRIL was assessed by comparing its activity with a standard solution of TRIL not encapsulated in the nanocage.

15. Statistical analysis

Statistical analyses were performed using Stata software (Version 13.0; StataCorp LP., College Station, TX, USA). Tukey's post hoc test was used if the treatment was significant on analysis of variance (ANOVA). All data are represented as the mean ± SE. Statistical significance was set at $p < 0.05$.

REFERENCES

(1) Doll, T. A. P. F.; Raman, S.; Dey, R.; Burkhard, P. Nanoscale Assemblies and Their Biomedical Applications. *J. R. Soc. Interface.* **2013**, *10* (80), 20120740. https://doi.org/10.1098/rsif.2012.0740.

(2) Lee, L.; Wang, Q. Adaptations of Nanoscale Viruses and Other Protein Cages for Medical Applications. *Nanomedicine: Nanotechnology, Biology and Medicine* **2006**, *2* (3), 137–149. https://doi.org/10.1016/j.nano.2006.07.009.

(3) MaHam, A.; Tang, Z.; Wu, H.; Wang, J.; Lin, Y. Protein-Based Nanomedicine Platforms for Drug Delivery. *Small* **2009**, *5* (15), 1706–1721. https://doi.org/10.1002/smll.200801602.

(4) Andrews, S. C. The Ferritin-like Superfamily: Evolution of the Biological Iron Storeman from a Rubrerythrin-like Ancestor. *Biochimica et Biophysica Acta (BBA) - General Subjects* **2010**, *1800* (8), 691–705. https://doi.org/10.1016/j.bbagen.2010.05.010.

(5) Chasteen, N. D.; Harrison, P. M. Mineralization in Ferritin: An Efficient Means of Iron Storage. *Journal of Structural Biology* **1999**, *126* (3), 182–194. https://doi.org/10.1006/jsbi.1999.4118.

(6) Le Brun, N. E.; Crow, A.; Murphy, M. E. P.; Mauk, A. G.; Moore, G. R. Iron Core Mineralisation in Prokaryotic Ferritins. *Biochimica et Biophysica Acta (BBA) - General Subjects* **2010**, *1800* (8), 732–744. https://doi.org/10.1016/j.bbagen.2010.04.002.

(7) Bertini, I.; Lalli, D.; Mangani, S.; Pozzi, C.; Rosa, C.; Theil, E. C.; Turano, P. Structural Insights into the Ferroxidase Site of Ferritins from Higher Eukaryotes. *J. Am. Chem. Soc.* **2012**, *134* (14), 6169–6176. https://doi.org/10.1021/ja210084n.

(8) Pfaffen, S.; Abdulqadir, R.; Le Brun, N. E.; Murphy, M. E. P. Mechanism of Ferrous Iron Binding and Oxidation by Ferritin from a Pennate Diatom. *Journal of Biological Chemistry* **2013**, *288* (21), 14917–14925. https://doi.org/10.1074/jbc.M113.454496.

(9) Drysdale, J. W. Ferritin Phenotypes: Structure and Metabolism. In *Novartis Foundation Symposia*; Porter, R., Fitzsimons, D. W., Eds.;

Wiley, 1977; pp 41–78. https://doi.org/10.1002/9780470720325.ch3.

(10) Levi, S.; Yewdall, S. J.; Harrison, P. M.; Santambrogio, P.; Cozzi, A.; Rovida, E.; Albertini, A.; Arosio, P. Evidence of H- and L-Chains Have Co-Operative Roles in the Iron-Uptake Mechanism of Human Ferritin. *Biochemical Journal* **1992**, *288* (2), 591–596. https://doi.org/10.1042/bj2880591.

(11) Reutovich, A. A.; Srivastava, A. K.; Arosio, P.; Bou-Abdallah, F. Ferritin Nanocages as Efficient Nanocarriers and Promising Platforms for COVID-19 and Other Vaccines Development. *Biochimica et Biophysica Acta (BBA) - General Subjects* **2023**, *1867* (3), 130288. https://doi.org/10.1016/j.bbagen.2022.130288.

(12) Wu, Y.; Huo, C.; Ming, T.; Liu, Y.; Su, C.; Qiu, X.; Lu, C.; Zhou, J.; Li, Y.; Zhang, Z.; Han, J.; Feng, Y.; Su, X. Structural and Functional Insights into the Roles of Potential Metal-Binding Sites in Apostichopus Japonicus Ferritin. *Polymers* **2022**, *14* (24), 5378. https://doi.org/10.3390/polym14245378.

(13) Guo, M.; Gao, M.; Liu, J.; Xu, N.; Wang, H. Bacterioferritin Nanocage: Structure, Biological Function, Catalytic Mechanism, Self-Assembly and Potential Applications. *Biotechnology Advances* **2022**, *61*, 108057. https://doi.org/10.1016/j.biotechadv.2022.108057.

(14) Rivera, M. Bacterioferritin: Structure, Dynamics, and Protein–Protein Interactions at Play in Iron Storage and Mobilization. *Acc. Chem. Res.* **2017**, *50* (2), 331–340. https://doi.org/10.1021/acs.accounts.6b00514.

(15) Chakraborti, S.; Chakrabarti, P. Self-Assembly of Ferritin: Structure, Biological Function and Potential Applications in Nanotechnology. In *Biological and Bio-inspired Nanomaterials*; Perrett, S., Buell, A. K., Knowles, T. P. J., Eds.; Advances in Experimental Medicine and Biology; Springer Singapore: Singapore, 2019; Vol. 1174, pp 313–329. https://doi.org/10.1007/978-981-13-9791-2_10.

(16) Grant, R. A.; Filman, D. J.; Finkel, S. E.; Kolter, R.; Hogle, J. M. The Crystal Structure of Dps, a Ferritin Homolog That Binds and

Protects DNA. *Nat Struct Mol Biol* **1998**, *5* (4), 294–303. https://doi.org/10.1038/nsb0498-294.

(17) Martinez, A.; Kolter, R. Protection of DNA during Oxidative Stress by the Nonspecific DNA-Binding Protein Dps. *J Bacteriol* **1997**, *179* (16), 5188–5194. https://doi.org/10.1128/jb.179.16.5188-5194.1997.

(18) Haikarainen, T.; Thanassoulas, A.; Stavros, P.; Nounesis, G.; Haataja, S.; Papageorgiou, A. C. Structural and Thermodynamic Characterization of Metal Ion Binding in Streptococcus Suis Dpr. *Journal of Molecular Biology* **2011**, *405* (2), 448–460. https://doi.org/10.1016/j.jmb.2010.10.058.

(19) Pead, S.; Durrant, E.; Webb, B.; Larsen, C.; Heaton, D.; Johnson, J.; Watt, G. D. Metal Ion Binding to Apo, Holo, and Reconstituted Horse Spleen Ferritin. *Journal of Inorganic Biochemistry* **1995**, *59* (1), 15–27. https://doi.org/10.1016/0162-0134(94)00050-K.

(20) Abe, S.; Niemeyer, J.; Abe, M.; Takezawa, Y.; Ueno, T.; Hikage, T.; Erker, G.; Watanabe, Y. Control of the Coordination Structure of Organometallic Palladium Complexes in an Apo-Ferritin Cage. *J.*

Am. Chem. Soc. **2008**, *130* (32), 10512–10514. https://doi.org/10.1021/ja802463a.

(21) Klem, M. T.; Mosolf, J.; Young, M.; Douglas, T. Photochemical Mineralization of Europium, Titanium, and Iron Oxyhydroxide Nanoparticles in the Ferritin Protein Cage. *Inorg. Chem.* **2008**, *47* (7), 2237–2239. https://doi.org/10.1021/ic701740q.

(22) Wang, Q.; Mercogliano, C. P.; Löwe, J. A Ferritin-Based Label for Cellular Electron Cryotomography. *Structure* **2011**, *19* (2), 147–154. https://doi.org/10.1016/j.str.2010.12.002.

(23) Vande Velde, G.; Rangarajan, J. R.; Toelen, J.; Dresselaers, T.; Ibrahimi, A.; Krylychkina, O.; Vreys, R.; Van Der Linden, A.; Maes, F.; Debyser, Z.; Himmelreich, U.; Baekelandt, V. Evaluation of the Specificity and Sensitivity of Ferritin as an MRI Reporter Gene in the Mouse Brain Using Lentiviral and Adeno-Associated Viral Vectors. *Gene Ther* **2011**, *18* (6), 594–605. https://doi.org/10.1038/gt.2011.2.

(24) Shen, Y.; Li, X.; Dong, D.; Zhang, B.; Xue, Y.; Shang, P. Transferrin Receptor 1 in Cancer: A New Sight for Cancer Therapy. *Am J Cancer Res* **2018**, *8* (6), 916–931.

(25) Li, L.; Fang, C. J.; Ryan, J. C.; Niemi, E. C.; Lebrón, J. A.; Björkman, P. J.; Arase, H.; Torti, F. M.; Torti, S. V.; Nakamura, M. C.; Seaman, W. E. Binding and Uptake of H-Ferritin Are Mediated by Human Transferrin Receptor-1. *Proc. Natl. Acad. Sci. U.S.A.* **2010**, *107* (8), 3505–3510. https://doi.org/10.1073/pnas.0913192107.

(26) Yu, B.; Cheng, C.; Wu, Y.; Guo, L.; Kong, D.; Zhang, Z.; Wang, Y.; Zheng, E.; Liu, Y.; He, Y. Interactions of Ferritin with Scavenger Receptor Class A Members. *Journal of Biological Chemistry* **2020**, *295* (46), 15727–15741. https://doi.org/10.1074/jbc.RA120.014690.

(27) Zhen, Z.; Tang, W.; Chen, H.; Lin, X.; Todd, T.; Wang, G.; Cowger, T.; Chen, X.; Xie, J. RGD-Modified Apoferritin Nanoparticles for Efficient Drug Delivery to Tumors. *ACS Nano* **2013**, *7* (6), 4830–4837. https://doi.org/10.1021/nn305791q.

(28) Ji, X.-T.; Huang, L.; Huang, H.-Q. Construction of Nanometer Cisplatin Core-Ferritin (NCC-F) and Proteomic Analysis of Gastric Cancer Cell Apoptosis Induced with Cisplatin Released from the NCC-F. *Journal of Proteomics* **2012**, *75* (11), 3145–3157. https://doi.org/10.1016/j.jprot.2012.03.013.

(29) Domínguez-Vera, J. M. Iron(III) Complexation of Desferrioxamine B Encapsulated in Apoferritin. *Journal of Inorganic Biochemistry* **2004**, *98* (3), 469–472. https://doi.org/10.1016/j.jinorgbio.2003.12.015.

(30) Roder, C.; Thomson, M. J. Auranofin: Repurposing an Old Drug for a Golden New Age. *Drugs R D* **2015**, *15* (1), 13–20. https://doi.org/10.1007/s40268-015-0083-y.

(31) Park, S.-H. G.; Lee, J. G.; Berek, J. S.; Hu, M. Y. C.-T. Auranofin Displays Anticancer Activity against Ovarian Cancer Cells through FOXO3 Activation Independent of P53. *International Journal of Oncology* **2014**, *45* (4), 1691–1698. https://doi.org/10.3892/ijo.2014.2579.

(32) Freire Boullosa, L.; Van Loenhout, J.; Flieswasser, T.; De Waele, J.; Hermans, C.; Lambrechts, H.; Cuypers, B.; Laukens, K.; Bartholomeus, E.; Siozopoulou, V.; De Vos, W. H.; Peeters, M.; Smits, E. L. J.; Deben, C. Auranofin Reveals Therapeutic Anticancer Potential by Triggering Distinct Molecular Cell Death Mechanisms and Innate Immunity in Mutant P53 Non-Small Cell Lung Cancer. *Redox Biology* **2021**, *42*, 101949. https://doi.org/10.1016/j.redox.2021.101949.

(33) Gamberi, T.; Chiappetta, G.; Fiaschi, T.; Modesti, A.; Sorbi, F.; Magherini, F. Upgrade of an Old Drug: Auranofin in Innovative Cancer Therapies to Overcome Drug Resistance and to Increase Drug Effectiveness. *Medicinal Research Reviews* **2022**, *42* (3), 1111–1146. https://doi.org/10.1002/med.21872.

(34) Chiappetta, G.; Gamberi, T.; Faienza, F.; Limaj, X.; Rizza, S.; Messori, L.; Filomeni, G.; Modesti, A.; Vinh, J. Redox Proteome Analysis of Auranofin Exposed Ovarian Cancer Cells (A2780). *Redox Biology* **2022**, *52*, 102294. https://doi.org/10.1016/j.redox.2022.102294.

(35) Pontillo, N.; Pane, F.; Messori, L.; Amoresano, A.; Merlino, A. Cisplatin Encapsulation within a Ferritin Nanocage: A High-Resolution Crystallographic Study. *Chem. Commun.* **2016**, *52* (22), 4136–4139. https://doi.org/10.1039/C5CC10365G.

(36) Ferraro, G.; Monti, D. M.; Amoresano, A.; Pontillo, N.; Petruk, G.; Pane, F.; Cinellu, M. A.; Merlino, A. Gold-Based Drug Encapsulation within a Ferritin Nanocage: X-Ray Structure and Biological Evaluation as a Potential Anticancer Agent of the Auoxo3-Loaded Protein. *Chem. Commun.* **2016**, *52* (61), 9518–9521. https://doi.org/10.1039/C6CC02516A.

(37) Petruk, G.; Monti, D. M.; Ferraro, G.; Pica, A.; D'Elia, L.; Pane, F.; Amoresano, A.; Furrer, J.; Kowalski, K.; Merlino, A. Encapsulation of the Dinuclear Trithiolato-Bridged Arene Ruthenium Complex Diruthenium-1 in an Apoferritin Nanocage: Structure and Cytotoxicity. *ChemMedChem* **2019**, *14* (5), 594–602. https://doi.org/10.1002/cmdc.201800805.

(38) Ferraro, G.; Ciambellotti, S.; Messori, L.; Merlino, A. Cisplatin Binding Sites in Human H-Chain Ferritin. *Inorg. Chem.* **2017**, *56* (15), 9064–9070. https://doi.org/10.1021/acs.inorgchem.7b01072.

(39) Stockert, J. C.; Blázquez-Castro, A.; Cañete, M.; Horobin, R. W.; Villanueva, Á. MTT Assay for Cell Viability: Intracellular Localization of the Formazan Product Is in Lipid Droplets. *Acta Histochemica* **2012**, *114* (8), 785–796. https://doi.org/10.1016/j.acthis.2012.01.006.

(40) Monti, D. M.; Ferraro, G.; Merlino, A. Ferritin-Based Anticancer Metallodrug Delivery: Crystallographic, Analytical and Cytotoxicity Studies. *Nanomedicine: Nanotechnology, Biology and Medicine* **2019**, *20*, 101997. https://doi.org/10.1016/j.nano.2019.04.001.

(41) Petrosillo, G.; Ruggiero, F. M.; Paradies, G. Role of Reactive Oxygen Species and Cardiolipin in the Release of Cytochrome c from Mitochondria. *FASEB J* **2003**, *17* (15), 2202–2208. https://doi.org/10.1096/fj.03-0012com.

(42) Piao, Y.; Kim, H. G.; Oh, M. S.; Pak, Y. K. Overexpression of TFAM, NRF-1 and Myr-AKT Protects the MPP(+)-Induced Mitochondrial Dysfunctions in Neuronal Cells. *Biochim Biophys Acta* **2012**, *1820* (5), 577–585. https://doi.org/10.1016/j.bbagen.2011.08.007.

(43) Liang, M.; Fan, K.; Zhou, M.; Duan, D.; Zheng, J.; Yang, D.; Feng, J.; Yan, X. H-Ferritin–Nanocaged Doxorubicin Nanoparticles Specifically Target and Kill Tumors with a Single-Dose Injection. *Proc. Natl. Acad. Sci. U.S.A.* **2014**, *111* (41), 14900–14905. https://doi.org/10.1073/pnas.1407808111.

(44) Monti, D. M.; Ferraro, G.; Petruk, G.; Maiore, L.; Pane, F.; Amoresano, A.; Cinellu, M. A.; Merlino, A. Ferritin Nanocages Loaded with Gold Ions Induce Oxidative Stress and Apoptosis in MCF-7 Human Breast Cancer Cells. *Dalton Trans.* **2017**, *46* (44), 15354–15362. https://doi.org/10.1039/C7DT02370G.

(45) Kreishman-Deitrick, M.; Egile, C.; Hoyt, D. W.; Ford, J. J.; Li, R.; Rosen, M. K. NMR Analysis of Methyl Groups at 100−500 kDa: Model Systems and Arp2/3 Complex. *Biochemistry* **2003**, *42* (28), 8579–8586. https://doi.org/10.1021/bi034536j.

(46) Li, X.; Zhang, Y.; Chen, H.; Sun, J.; Feng, F. Protein Nanocages for Delivery and Release of Luminescent Ruthenium(II) Polypyridyl Complexes. *ACS Appl. Mater. Interfaces* **2016**, *8* (35), 22756–22761. https://doi.org/10.1021/acsami.6b07038.

(47) Conti, L.; Ciambellotti, S.; Giacomazzo, G. E.; Ghini, V.; Cosottini, L.; Puliti, E.; Severi, M.; Fratini, E.; Cencetti, F.; Bruni, P.; Valtancoli, B.; Giorgi, C.; Turano, P. Ferritin Nanocomposites for the Selective Delivery of Photosensitizing Ruthenium-Polypyridyl Compounds to Cancer Cells. *Inorg. Chem. Front.* **2022**, *9* (6), 1070–1081. https://doi.org/10.1039/D1QI01268A.

(48) Belletti, D.; Pederzoli, F.; Forni, F.; Vandelli, M. A.; Tosi, G.; Ruozi, B. Protein Cage Nanostructure as Drug Delivery System: Magnifying Glass on Apoferritin. *Expert Opinion on Drug Delivery* **2017**, *14* (7), 825–840. https://doi.org/10.1080/17425247.2017.1243528.

(49) Di Somma, A.; Moretta, A.; Canè, C.; Cirillo, A.; Duilio, A. Antimicrobial and Antibiofilm Peptides. *Biomolecules* **2020**, *10* (4), 652. https://doi.org/10.3390/biom10040652.

(50) Wang, C.; Li, H.-B.; Li, S.; Tian, L.-L.; Shang, D.-J. Antitumor Effects and Cell Selectivity of Temporin-1CEa, an Antimicrobial Peptide from the Skin Secretions of the Chinese Brown Frog (Rana Chensinensis). *Biochimie* **2012**, *94* (2), 434–441. https://doi.org/10.1016/j.biochi.2011.08.011.

(51) Rinaldi, A. C.; Mangoni, M. L.; Rufo, A.; Luzi, C.; Barra, D.; Zhao, H.; Kinnunen, P. K. J.; Bozzi, A.; Giulio, A. D.; Simmaco, M. Temporin L: Antimicrobial, Haemolytic and Cytotoxic Activities, and Effects on Membrane Permeabilization in Lipid Vesicles. *Biochemical Journal* **2002**, *368* (1), 91–100. https://doi.org/10.1042/bj20020806.

(52) Rychtarcikova, Z.; Lettlova, S.; Tomkova, V.; Korenkova, V.; Langerova, L.; Simonova, E.; Zjablovskaja, P.; Alberich-Jorda, M.; Neuzil, J.; Truksa, J. Tumor-Initiating Cells of Breast and Prostate Origin Show Alterations in the Expression of Genes Related to Iron Metabolism. *Oncotarget* **2017**, *8* (4), 6376–6398. https://doi.org/10.18632/oncotarget.14093.

(53) Aranda, A.; Sequedo, L.; Tolosa, L.; Quintas, G.; Burello, E.; Castell, J. V.; Gombau, L. Dichloro-Dihydro-Fluorescein Diacetate (DCFH-DA) Assay: A Quantitative Method for Oxidative Stress Assessment of Nanoparticle-Treated Cells. *Toxicology in Vitro* **2013**, *27* (2), 954–963. https://doi.org/10.1016/j.tiv.2013.01.016.

(54) Wang, B.; Zhang, J.; Song, F.; Tian, M.; Shi, B.; Jiang, H.; Xu, W.; Wang, H.; Zhou, M.; Pan, X.; Gu, J.; Yang, S.; Jiang, L.; Li, Z.

EGFR Regulates Iron Homeostasis to Promote Cancer Growth through Redistribution of Transferrin Receptor 1. *Cancer Letters* **2016**, *381* (2), 331–340. https://doi.org/10.1016/j.canlet.2016.08.006.

(55) Wang, C.; Tian, L.-L.; Li, S.; Li, H.-B.; Zhou, Y.; Wang, H.; Yang, Q.-Z.; Ma, L.-J.; Shang, D.-J. Rapid Cytotoxicity of Antimicrobial Peptide Tempoprin-1CEa in Breast Cancer Cells through Membrane Destruction and Intracellular Calcium Mechanism. *PLoS ONE* **2013**, *8* (4), e60462. https://doi.org/10.1371/journal.pone.0060462.

(56) Antony, A.; Olakkaran, S.; Purayil, A. K.; Shekh, S.; Gowd, K. H.; Gurushankara, H. P. Antitumor Activity of Tigerinin-1: Necroptosis Mediates Toxicity in A549 Cells. *Biochimica et Biophysica Acta (BBA) - General Subjects* **2022**, *1866* (9), 130182. https://doi.org/10.1016/j.bbagen.2022.130182.

(57) Di Somma, A.; Avitabile, C.; Cirillo, A.; Moretta, A.; Merlino, A.; Paduano, L.; Duilio, A.; Romanelli, A. The Antimicrobial Peptide Temporin L Impairs E. Coli Cell Division by Interacting with FtsZ and the Divisome Complex. *Biochimica et Biophysica Acta (BBA)*

- *General Subjects* **2020**, *1864* (7), 129606. https://doi.org/10.1016/j.bbagen.2020.129606.

(58) Bradford, M. M. A Rapid and Sensitive Method for the Quantitation of Microgram Quantities of Protein Utilizing the Principle of Protein-Dye Binding. *Analytical Biochemistry* **1976**, *72* (1–2), 248–254. https://doi.org/10.1016/0003-2697(76)90527-3.

(59) Yang, Z.; Wang, X.; Diao, H.; Zhang, J.; Li, H.; Sun, H.; Guo, Z. Encapsulation of Platinum Anticancer Drugs by Apoferritin. *Chem. Commun.* **2007**, No. 33, 3453. https://doi.org/10.1039/b705326f.

(60) Petrák, J.; Vyoral, D. Detection of Iron-Containing Proteins Contributing to the Cellular Labile Iron Pool by a Native Electrophoresis Metal Blotting Technique. *Journal of Inorganic Biochemistry* **2001**, *86* (4), 669–675. https://doi.org/10.1016/S0162-0134(01)00232-X.

(61) Parella, T.; Adell, P.; Sánchez-Ferrando, F.; Virgili, A. Effective Multiple-Solvent Suppression Scheme Using the Excitation Sculpting Principle. *Magn. Reson. Chem.* **1998**, *36* (4), 245–249.

https://doi.org/10.1002/(SICI)1097-458X(199804)36:4<245::AID-OMR264>3.0.CO;2-J.

(62) Piotto, M.; Saudek, V.; Sklenář, V. Gradient-Tailored Excitation for Single-Quantum NMR Spectroscopy of Aqueous Solutions. *J Biomol NMR* **1992**, *2* (6), 661–665. https://doi.org/10.1007/BF02192855.

(63) Stejskal, E. O.; Tanner, J. E. Spin Diffusion Measurements: Spin Echoes in the Presence of a Time-Dependent Field Gradient. *The Journal of Chemical Physics* **1965**, *42* (1), 288–292. https://doi.org/10.1063/1.1695690.

(64) Vonrhein, C.; Flensburg, C.; Keller, P.; Sharff, A.; Smart, O.; Paciorek, W.; Womack, T.; Bricogne, G. Data Processing and Analysis with the autoPROC Toolbox. *Acta Crystallogr D Biol Crystallogr* **2011**, *67* (4), 293–302. https://doi.org/10.1107/S0907444911007773.

(65) Murshudov, G. N.; Skubák, P.; Lebedev, A. A.; Pannu, N. S.; Steiner, R. A.; Nicholls, R. A.; Winn, M. D.; Long, F.; Vagin, A. A. REFMAC 5 for the Refinement of Macromolecular Crystal

Structures. *Acta Crystallogr D Biol Crystallogr* **2011**, *67* (4), 355–367. https://doi.org/10.1107/S0907444911001314.

(66) Emsley, P.; Lohkamp, B.; Scott, W. G.; Cowtan, K. Features and Development of Coot. *Acta Crystallogr D Biol Crystallogr* **2010**, *66* (4), 486–501. https://doi.org/10.1107/S0907444910007493.

(67) Petruk, G.; Raiola, A.; Del Giudice, R.; Barone, A.; Frusciante, L.; Rigano, M. M.; Monti, D. M. An Ascorbic Acid-Enriched Tomato Genotype to Fight UVA-Induced Oxidative Stress in Normal Human Keratinocytes. *Journal of Photochemistry and Photobiology B: Biology* **2016**, *163*, 284–289. https://doi.org/10.1016/j.jphotobiol.2016.08.047.

CHAPTER 2

MNEI mutants: design, stability, and aggregation properties

STATE OF ART

The protein fibrillation mechanism has been often studied with reference to several human diseases that are characterized by the formation of amyloid deposits[1]. The term "amyloid" was used for the first time by Rudolf Virchow to describe a structured mass in human tissues, which was considered to be a cellulose-containing substance based on its ability to be stained by iodine[2]. Later, direct chemical analysis showed that the main component of amyloids is protein. Now, amyloid fibrils refer to elongated protein aggregates characterized by long and relatively straight morphologies, cross-β diffraction patterns, specific dye binding properties and rigid core structures[3]. Indeed, amyloid fibers show a characteristic X-ray diffraction pattern[4] with 4.8 Å meridional reflections and 10 Å equatorial reflections (**Figure 2.1**).

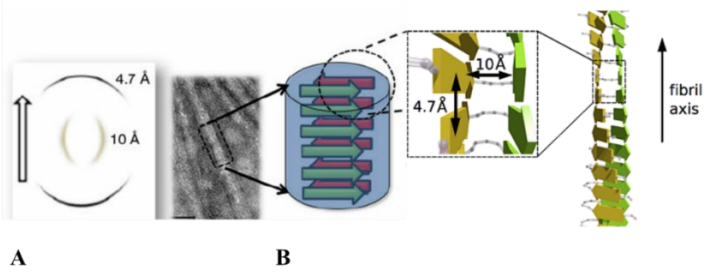

Figure 2.1. A) Schematic representation of the cross- β X-ray diffraction pattern typically produced by the amyloid fibrils. **B**) Scheme of the cross-β structure of a

mature amyloid fibril with a densely packed two-layer β-sheet structure. Each β-sheet is indicated by yellow or green color and shows a parallel alignment of the β-strands (yellow and green arrows).

They bind to and alter the spectroscopic properties of congo-red[5] and thioflavin dyes[6]. Hydrogen exchange experiments coupled with mass spectrometry (HX-MS)[7] or with nuclear magnetic resonance (HX-NMR)[8] have suggested that amyloid fibrils possess extensively hydrogen-bonded β-sheet core structures, which confer to them remarkably stability and resistance to protease cleavage[9]. Moreover, transmission electron microscopy (TEM) and atomic force microscopy (AFM) have revealed that the fibrils usually consist of a number (typically 2–6) of protofilaments, each about 2–5 nm in diameter[10]. These protofilaments twist together to form rope-like fibrils that are typically 7–13 nm wide[10,11] or associate laterally to form long ribbons that are 2–5 nm thick and up to 30 nm wide[12,13]. X-ray fiber diffraction data have shown that in each individual protofilament the protein or peptide molecules are arranged so that the polypeptide chain forms β-strands that run perpendicular to the long axis of the fibril[11] (**Figure 2.2**).

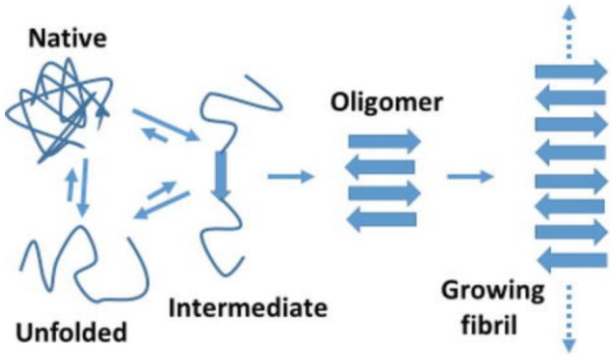

Figure 2.2. Steps of mature amyloid fibrils formation.

It is widely established that amyloid fibril formation has many characteristics of a "nucleated growth" mechanism. The time course of the conversion of a peptide or protein into its fibrillar form typically includes a lag phase that is followed by a rapid exponential growth phase[14,15]. The lag phase is assumed to be the time required for "nuclei" to form. Once a nucleus is formed, fibril growth is thought to proceed rapidly by further association of either monomers or oligomers with the nucleus. As with many other processes dependent on a nucleation step, addition of preformed fibrillar species to a sample of a protein under aggregation conditions ("seeding") causes the lag phase to be shortened and ultimately abolished because the rate of the aggregation process is no longer limited by the need for nucleation[16,17]. It has been shown also that changes in experimental conditions, or certain types of mutations,

can also reduce or eliminate the length of the lag phase[18,19]. Furthermore, it is generally believed that globular proteins need to unfold, at least partially, to aggregate into amyloid fibrils[20–22] and have an increased propensity to aggregate under conditions that promote their partial unfolding. Indeed, there is a strong correlation between a decreased conformational stability of the native state and an increased propensity to aggregate into amyloid-like structures. In fact, the ability of proteins to form fibrils is an intricate process and is influenced by different parameters, extrinsic or intrinsic to the protein. Extrinsic factors include physico-chemical parameters, such as pH, temperature, ionic strength, and protein concentration[23–25]. The pH may be positively correlated to the rate of aggregation: the increased positive charge that proteins tend to have at low pH is expected to disfavor aggregation, but such an effect is more than counterbalanced by the lowering of the stability of most proteins with decreasing pH[26]. Several authors have proposed the existence of a critical concentration for amyloid formation, which is specific for each system[27]. Other factors, such as temperature, stirring and native state stability, are known to influence amyloid aggregation rates significantly. High temperatures are generally found to lead to faster aggregation rates[25,28], even if in some cases may lead to

denaturation and formation of amorphous aggregates. Conversely, the intrinsic factors refer to the features defining a specific protein, such as charge, hydrophobicity, patterns of polar and non-polar residues, and also the propensity to adopt different secondary structure motifs. In a globular protein the polypeptide main chain and the hydrophobic side chains are largely buried within the folded structure. When they are exposed, for example when the protein is partly unfolded, the conversion of protein molecules into aggregated structures will have a higher probability to occur[29]. One important determinant of the aggregation of an unfolded polypeptide chain is the hydrophobicity of the side chains. Amino acid substitutions within regions of the sequence that play a crucial role in the behaviour of the whole sequence can reduce or increase the aggregation propensity of a protein when they decrease or increase the hydrophobicity at the site of mutation[30,31]. In fact, hhydrophobic interactions have long been suggested to play a significant role in amyloid formation: an increased hydrophobicity leads to increased aggregation[32]. Another property likely to be a key factor in protein aggregation is the charge, as a high net charge either globally or locally may hinder self-association[33]. Mutations decreasing the positive net charge of the protein resulted in an accelerated formation of β-sheet

containing aggregates. In addition to charge and hydrophobicity, a low propensity to form α-helical structure and a high propensity to form β-sheet structure are also likely to be important factors encouraging amyloid formation[34,35]. Patterns of alternating hydrophilic and hydrophobic residues have been shown to be less frequent in natural proteins than expected on a random basis, suggesting that evolutionary selection has reduced the probability of such sequence patterns that favour β-sheet formation[35].

Thus, protein aggregation varies with the sequence, since it influences protein behavior in case of both folding and misfolding[31]. For this reason, the stability of the native state plays a key role in the aggregation process. Specific regions of the protein, known as aggregation-prone regions, have a central role in the formation of stable fibrillar aggregates[36,37]. The existence of aggregation-prone regions could suggest the way in which rational mutagenesis can be used to design protein mutants able to form ordered intermolecular assemblies that can be easily isolated and replicated.

Generally, two types of mutational approaches can be used for this scope: punctual mutation and circular permutation.

Punctual mutation is a method of altering the nucleotide sequence of a gene at a specified location. It is a highly versatile technology that can be used to engineer proteins. Prediction of mutant protein stability with accuracy is desired for uncovering the molecular aspects of the design of novel proteins. Many advanced computational approaches have been developed over the years to predict the stability and function of a mutated protein[38]. These approaches based on structure, sequence features and combined features provide reasonably accurate estimation of the impact of amino acid substitution on stability and function of protein. Changing single nucleotides in the DNA sequence, point mutagenesis allows to draw different mutants and analyze one by one the effect of the mutation on the protein properties.

On the other hand, circular permutation can be the result of evolutionary events, post-translational modifications, or artificially engineered mutations. The result is a protein structure with different connectivity, but overall similar three-dimensional shape[39]. This protein modification was discovered in 1979 by Bruce Cunningham and his colleagues who identified the first instance of a circularly permuted protein in nature[40]. After the discovery of a natural circularly permuted protein, researchers looked for a way to emulate this process. In 1983, David Goldenberg and

Thomas Creighton were able to create a circularly permuted version of a protein by chemically ligating the termini to create a cyclic protein, then introducing new termini elsewhere using trypsin[41]. In 1989, Karolin Luger and her colleagues introduced a genetic method for making circular permutations by carefully fragmenting and ligating DNA[42]. This method allowed for permutations to be introduced at arbitrary sites and is still used today to design circularly permuted proteins in the lab. Today, circular permutations are generated routinely in the lab using standard genetics techniques[42]. Although some permutation sites prevent the protein from folding correctly, many permutants have been created with nearly identical structure and function to the original protein[39]. The motivation for creating a circular permutant of a protein can vary. Scientists may want to improve some property of the protein, such as: reduce proteolytic susceptibility, improve catalytic activity, alter substrate or ligand binding, improve thermostability, making proteins active over a wider range of temperatures and conditions can improve their utility.

It has been widely demonstrated that a huge number of proteins, unrelated to any known disease, can form amyloid structures *in vitro* in appropriate conditions[10,43,44]. In fact, self-assembling proteins became

popular not only for their implication in pathological conditions, but also for their potential as building block to obtain protein-based nanomaterials. Protein-based nanomaterials present several advantages, such as biodegradability, long-term stability, non-immunogenicity[45]. An example of fibrils applications is the use as delivery systems or diagnostic tools for targeted drug delivery, cancer therapy or vaccine development[45–47].

The understanding of the dynamics and the determinants of the structural modifications responsible for protein aggregation could be of help for the design of proteins able to produce fibrils suitable for potential biotechnological applications.

A recognized model to study this process is an intensely sweet, small plant protein, MNEI. It is a monellin single chain derivative, being designed to produce a sweeter and more stable protein compared to the parent one. MNEI is composed of a sole α-helix packed against a 5-stranded β-sheet in a β-grasp fold. Besides its potential as protein-based sweetener, this globular protein also represents a good model for protein self-assembly studies. Indeed, the folding and unfolding reactions of MNEI have been deeply characterized[48,49] and appear to be multistate. In fact, parallel pathways are populated by multiple intermediates[49]. Jha and

coworkers[50] demonstrated that MNEI unfolding process initiates with the protein expansion into a dry molten globular state in which the single α-helix moves out from the native state gradually[50]. It has been recently reported a systematic study of the aggregation mechanisms of this protein[51–53] showing MNEI as a model protein for studies on fibrils formation. In fact, under mild denaturing conditions/early unfolding stages, it can be converted into insoluble, amyloid state, giving rice to linear or branched structures. In particular, these structures can be observed at acidic pH, where the prolonged incubation of the protein, at a temperature far below its melting temperature, prompts the formation of aggregates with the typical features of amyloid fibrils. On the contrary, at neutral pH (pH = 6.8), only amorphous aggregates can be detected[51], suggesting that pH is the main switch between amyloid and amorphous aggregation. Furthermore, the presence of salts, particularly chlorides, accelerates fibrils formation[52]. Due to its great potential, many studies have been conducted to improve MNEI features. In particular, most of these studies have been focused to the rational design of mutants with higher resistance and thermal and chemical stability, even at neutral pH. Both the approaches described above have been applied for the drawing of new mutants of MNEI. Especially, this PhD work puts the attention

on the analysis of the stability and the fibrillation abilities of two different mutated MNEI systems:

i) a mutant designed by the research group upon the mutation of four aminoacidic residues, named Mut9, and

ii) three mutants obtained by circular permutation in the laboratory of Professor Lars Oliver Essen of Marburg University (Germany), named Perm 1, Perm 2, and Perm 3.

Both mutants have been deeply studied from a biophysical, biochemical, and structural point of view to investigate their stability and fibrillation capability in comparison to the mother protein MNEI.

RESULTS AND DISCUSSION

1. Mut9: a super stable MNEI mutant

Speaking of site-directed mutagenesis, Liu and co-workers by this technique were able to point out that many mutations enhancing MNEI thermostability were distributed at the two ends of α-helix[54]. They showed how the replacement of unpartnered ionizable residue Glu23 from the hydrophobic core of the protein with an alanine (E23A) can stabilize the native state of the protein. In addition, they proved that C41

residue, located at the second β-strand, can contribute to thermostability improvement playing a concerted role with E23 to account for the pH dependent stability of the protein at pH > 8[54]. Rega et al. designed and produced Y65R-MNEI, a mutant significantly sweeter than the parent protein, predicted to interact more efficiently with the sweet receptor T1R2:T1R3[55].

Based on these findings, recently my research group has designed a new mutant selecting the most promising point mutations: Y65R, E23A, C41A and S76Y[56]. This protein is Mut9.

Mut9 has been defined a "super stable" mutant due to its uncommon features[56]. The new protein showed high stability in acidic and neutral environments, a higher melting temperature (over 20 °C) than that of MNEI and resulted twice sweeter than MNEI. Notably, it preserved its structure and function even after 10 minutes boiling, in particular at pH 6.8, and a shelf-life higher than 6-month in different pH conditions. This protein is the proof that multiple mutations of different residues can lead to an additive performance with both improved sweetness and stability, suggesting that the sweetness and stability could be modulated by independent molecular mechanisms.

Inspired by these features, the aim of this project was to carry out a comparative study between Mut9 and its parent protein to understand the structural grounds of the high stability of the protein. The analysis of the effect of single point mutations on Mut9 stability has been evaluated by X-ray crystallography and circular dichroism spectroscopy. In addition, Mut9 aggregation tendency at two different pHs was evaluated and the morphology of the obtained fibrils was analyzed. In particular, the kinetics of aggregation and the parallel changes of the protein structure, under different experimental conditions, have been studied by ThT assay and FTIR spectroscopy respectively, while fibrils morphology has been investigated by TEM.

To study the effect of the mutations on Mut9 stability, its melting temperatures, in the experimental conditions used to obtain MNEI fibrils[51], *i.e.* pH 2.5 and pH 6.8 in the presence and in the absence of sodium chloride, have been calculated by circular dichroism spectroscopy, following the CD signal at 215 nm as function of temperature (**Table 2.1**). As discussed in the previous paragraphs, it has been demonstrated that the mutation Y65R prompts a thermal stability decrease of the protein, lowering the T_m of about 4-8 degrees, with respect to MNEI[51] (**Table 2.1**), due to the increased distances between

residues Tyr63 and Phe94, which cut off some stabilizing interactions. In contrast, in Mut9, the mutation Y65R does not affect the thermal stability, which appears even higher than that of MNEI, increasing at pH 6.8, by almost twenty degrees.

Table 2.1. Values of T_m characterizing the thermal-induced denaturation of Mut9 in different experimental conditions. The T_m of MNEI and Y65R-MNEI are also reported for comparison. Errors on T_m are within 1 °C.

	Mut9	***MNEI***[51]	***Y65R-MNEI***[51]
pH 2.5	87	*73*	*66*
pH 2.5 + 0.1 M NaCl	86	*77*	*69*
pH 6.8	92	*75*	*71*
pH 6.8 + 0.1 M NaCl	92	*75*	*71*

These findings suggest that the overall stability of the protein is not related to a single residue but may depend on a network of interactions involving residues located in different sites of the protein.

The structures of MNEI and Mut9 from isomorphic crystals possess 2032 and 1976 atoms, respectively. The X-ray structures (**Figure 2.3**), obtained from crystals with two molecules in the asymmetric unit (chain A and chain B), have been refined at a resolution of 1.19 and 1.50 Å, and to R-factor and R_{free} values within the range 0.218/0.256 and 0.223/0.274, respectively.

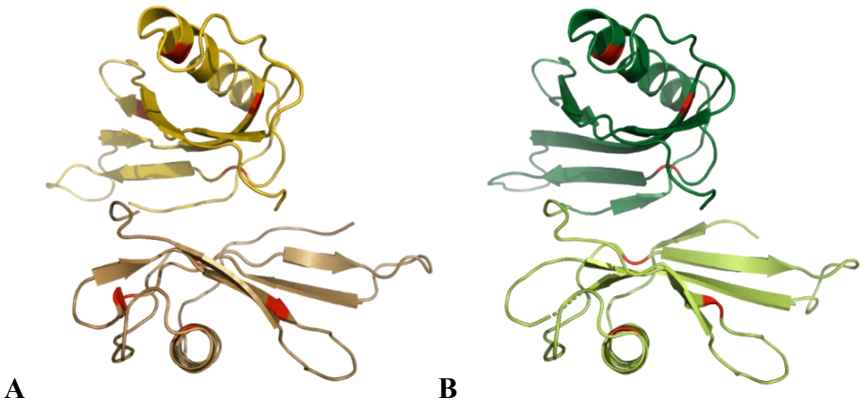

Figure 2.3. Cartoon representation of the X-ray structures of MNEI (A) and Mut9 (B). The two molecules of the asymmetric unit are shown in dark yellow and gold for MNEI and in light and dark green for Mut9. The position of the mutated residues is indicated in red.

Both structures are very similar to each other, as revealed by the analysis of the values of the root mean square deviations of the distances between the Cα (RMSD, **Table 2.2**), and to the structures of MNEI and its mutants reported in literature (**Table 2.3**).

Table 2.2. r.m.s.d. (Å) between the two chains A and B of MNEI and Mut9.

		MNEI		**Mut9**	
		chain A	chain B	chain A	chain B
MNEI	chain A	-			
	chain B	0.299	-		
Mut9	chain A	0.236	0.317	-	
	chain B	0.335	0.311	0.236	-

Table 2.3. r.m.s.d. (Å) between the two A and B chains of MNEI and Mut9, and of the crystallographic structures of MNEI and its mutants reported in literature.

PDB code	mutation	chain	MNEI		Mut9	
			chain A	chain B	chain A	chain B
2O9U	//	X	0.579	0.505	0.526	0.546
3PXM	V37A	A	0.332	0.47	0.452	0.557
		B	0.587	0.446	0.682	0.599
3PYJ	G16A	A	0.433	0.621	0.461	0.567
3Q2P	G16A; V38A	A	0.307	0.399	0.375	0.38
		B	0.34	0.357	0.41	0.386
		C	0.341	0.504	0.35	0.379
		D	0.328	0.373	0.335	0.389
5LC6	Q28K; C41S; Y65R	A	0.459	0.671	0.423	0.525
		B	0.327	0.365	0.271	0.361
5LC7	E23Q; Q28K; C41S; Y65R	A	0.288	0.234	0.244	0.231
		B	0.201	0.301	0.229	0.291
5O7K	Y65R	A	0.423	0.6	0.445	0.569
		B	0.361	0.341	0.316	0.385
5O7L	Y65R	A	0.498	0.723	0.48	0.606
		B	0.37	0.382	0.33	0.416
5O7Q	Y65R	A	0.342	0.492	0.376	0.461
		B	0.457	0.468	0.448	0.515
5O7R	Y65R	A	0.323	0.314	0.371	0.349
		B	0.314	0.421	0.322	0.388
5O7S	Y65R	A	0.345	0.35	0.365	0.387
		B	0.327	0.465	0.424	0.442
5Z1P	E3N; E24A	A	0.354	0.341	0.347	0.364
		B	0.324	0.432	0.352	0.372

		C	0.358	0.521	0.404	0.43
		D	0.349	0.327	0.329	0.355

In fact, the graphs of B-relative (obtained by normalization of B-factors[57] reported as a function of residue of MNEI and Mut9 (**Figure 2.4**) are very similar, except for the region between residues 45-60, where Mut9 shows higher B-relative values than MNEI.

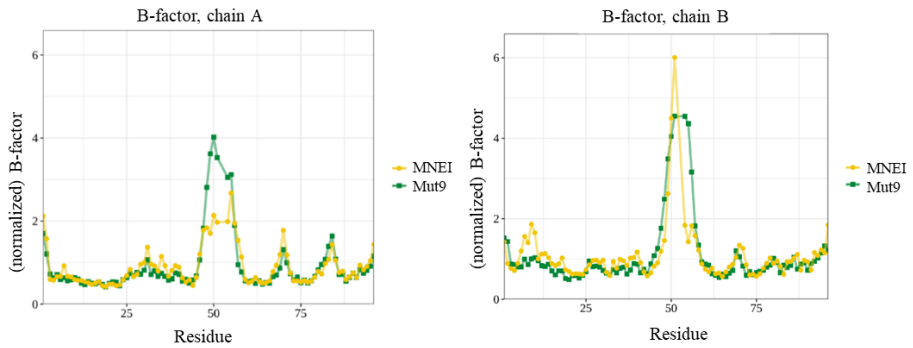

Figure 2.4. Graphic representations of B-relative trend as a function of residue in chains A and B of MNEI and Mut9.

This difference could be related to the L23 loop located in this region (residues 47-56) which, in all the structures reported for MNEI and its derivatives, is generally highly flexible or disordered. Indeed, in the structure of Mut9 the electron density map in this region is not well defined.

To understand the determinants of the different thermal stability of MNEI and Mut9, the structural features of each molecule of the asymmetric unit were analyzed and compared. MNEI and Mut9 possess a comparable number of hydrogen bonds and salt bridges, similar solvent-accessible surfaces and hidden regions, and similar volume (**Table 2.4**).

Table 2.4. Structural features of each molecule of the asymmetric unit found in MNEI and Mut9 crystals.

Protein	MNEI		Mut9	
Chain	A	B	A	B
Number of hydrogen bonds (main chain)*	57	60	58	54
Number of hydrogen bonds (side chains)*	26	20	19	19
Number of salt bridges*	0	0	0	0
Solvent accessible surface (Total ASA)* (Å^2)	6086.4	5976.9	6064.4	6068.9
Non-polar surface* (Å^2)	3496.7	3402.4	3417.2	3416.2
Polar surface* (Å^2)	1127.6	1116.5	1144.5	1095.7
Charged surface* Errore. Il segnalibro non è definito. **(Å^2)**	1462.1	1458.0	1502.8	1557.0
Volume* (Å^3)	13116.2	13080.6	13178.5	13329.6
Compactness*	2.2629	2.2262	2.2476	2.2323
Hidden surface between the two molecules of the a.u.§ (Å^2)	865.748		903.476	

*Calculated with WHAT_IF[58] - §Calculated with UCSF Chimera[59]

Thus, the two proteins show similar structural features, suggesting that the presence of the mutation sites do not introduce variations of general protein conformation, as also suggested by their capability to recognize the same receptors, eliciting the sweet taste. Therefore, we have analyzed one by one the single point mutations to investigate the reasons for the increased Mut9 stability with respect to MNEI.

Y65R mutation

The mutation Y65R introduces a positive charge on the surface of MNEI associated with a sweetness increase[60] and a thermal stability decrease of the protein[51]. Crystallographic studies revealed that the mutation induces structural changes in the C-terminal region of the protein, responsible for the lower stability of Y65R mutant to the respect of MNEI[51]. In particular, the Arg65 side chain in Y65R mutant appears disordered. The disorder of this residue affects the conformation of the residue Tyr63, which, in the structure of MNEI, interacts with the residue Phe94 at the C-terminus. Consequently, in the Y65R mutant, the distances between Tyr63 and Phe94 are slightly greater than those observed in MNEI[51]. This difference could contribute to the lower thermal stability of the mutant compared to that of MNEI. In contrast, in

the two chains of the asymmetric unit of MNEI and Mut9, the electron density map of residue 65 is well defined (**Figure 2.5**).

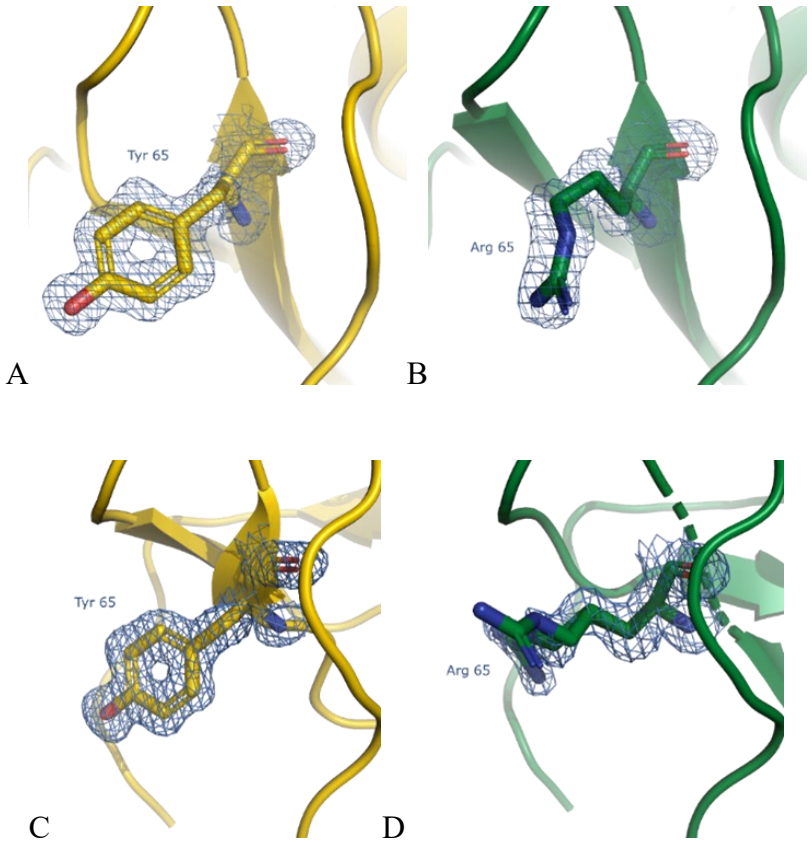

Figure 2.5. 2Fo-Fc electron density map of residue 65 in MNEI (yellow) and Mut9 (green). Chains A are reported in panels A and B, chains B in panel C and D. Electron density is contoured at 1σ.

The analysis of the distances between residues 63 and 94 shows that the neighborhood of residue 65 in Mut9 is more similar to MNEI than to

Y65R, suggesting that in this mutant the Y65R mutation is less destabilizing than in Y65R-MNEI (**Table 2.5**, **Figure 2.6**).

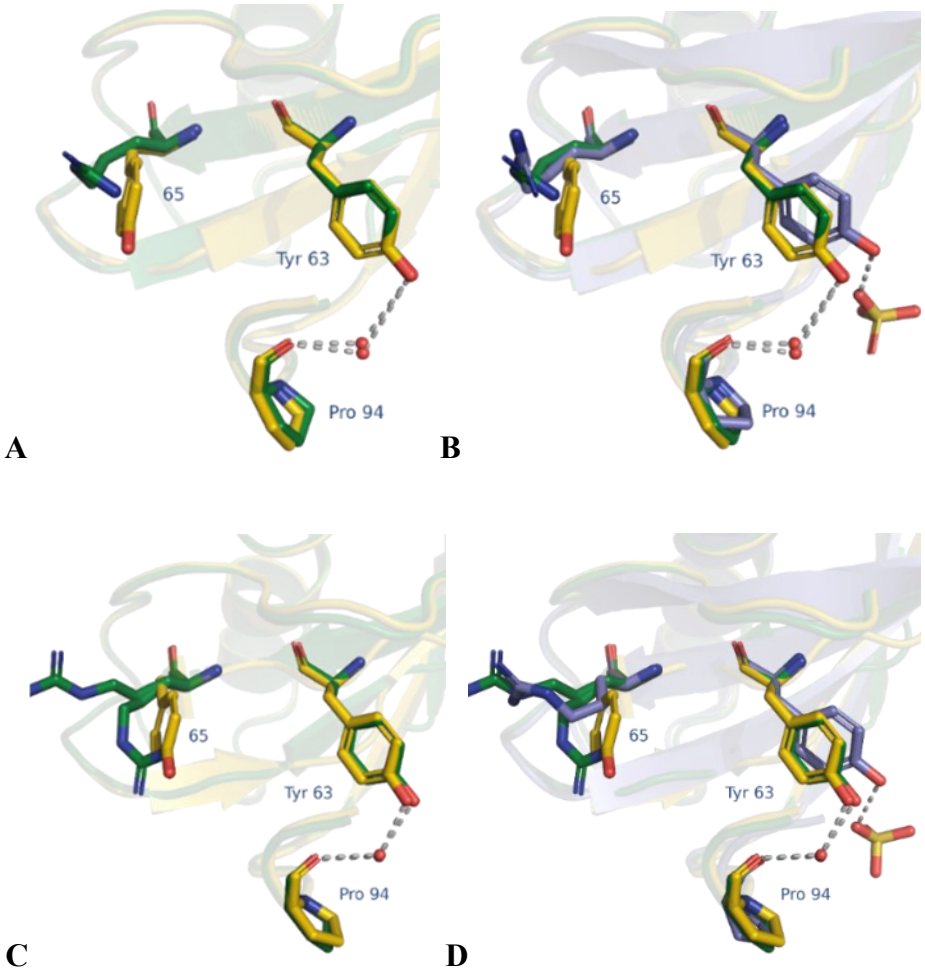

Figure 2.6. Neighborhood of residue 65. The interactions of residues 63 and 94, which have been hypothesized to play an important role in protein stability, are highlighted. In yellow MNEI, in green Mut9 and in blue Y65R. Chains A in panels A and B, chains B in panels C and D.

Table 2.5. Distances (Å) between residues 63 and 94 in both molecules of the asymmetric unit of MNEI and Mut9. The distances have been calculated also for Y65R structures by Pica et al.[51] for comparison.

PDB code	**Mutation**	**pH**	**Distance (Å)**			
			Y63, OH - P94, O (chain A)	***Y63, OH - X - P94, O (chain A)***	***Y63, OH - P94, O (chain B)***	***Y63, OH - X - P94, O (chain B)***
MNEI	//	4.6	5.28	3.56---H_2O---2.85	4.45	2.60---H_2O---2.65
Mut9	E23A; C41A; Y65R; S76Y	4.6	5.25	3.29---H_2O---2.70	4.85	2.76---H_2O---2.80
5O7L	Y65R	4.6	6.53	2.66---SO_4---5.74	6.06	2.79--- SO_4---4.96
1MOL (WT)	//	7.4	5.15	-	5.59	3.72---H_2O---2.70
2O9U* (WT)	//	5.6	4.04	2.65---H_2O---2.67	4.76	2.65---H_2O---2.80
5O7K	Y65R	2	5.83	2.77---H_2O---5.17	5.73	2.49---SO_4---5.24
5O7Q	Y65R	5.5	5.94	4.14---H_2O---2.44	5.73	4.10---H_2O---2.78
5O7R	Y65R	6.5	5.69	3.87---H_2O---2.58	5.67	4.12---H_2O---2.41
5O7S	Y65R	8.3	5.4	2.73---H_2O---3.09	5.57	3.52---H_2O---2.53

C41A mutation

The C41A mutation is related to the sweetness decrease and the thermal stability increase of MNEI[54]. This residue is located in a hydrophobic pocket formed by residues Ile6, Thr12, Leu15, Val37 and Leu62. In both molecules of the asymmetric unit of MNEI crystals, the sulfur atom of Cys41 forms unfavorable interactions with the residues of this pocket. In Mut9 the C41A substitution eliminates the unfavorable MNEI-Cys41 interactions, thus stabilizing the structure of the mutant. In fact, the side chain of the alanine is less bulky than that of cysteine. In this way the surrounding residues have much more space. The comparison between the structures of MNEI and Mut9 also shows a conformational change of Leu62 side chain due to the mutation. Leu62 occupies part of the empty space introduced by the C→A substitution (**Figure 2.7**).

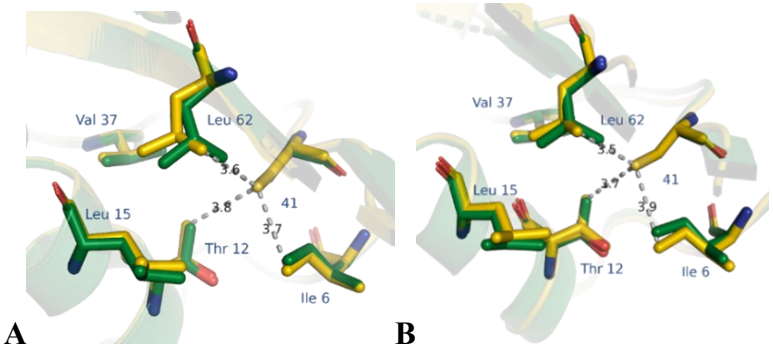

Figure 2.7. Details of the interactions of residue 41 with the surrounding residues in the structures of MNEI (yellow) and Mut9 (green). Chains A are reported in panel A, chains B in panel B. The distances are represented by grey dashes.

This conformational variation is observed in both molecules of the asymmetric unit. In the two chains of the asymmetric unit of MNEI and Mut9, the electron density map of residue 41 is well defined (**Figure 2.8**).

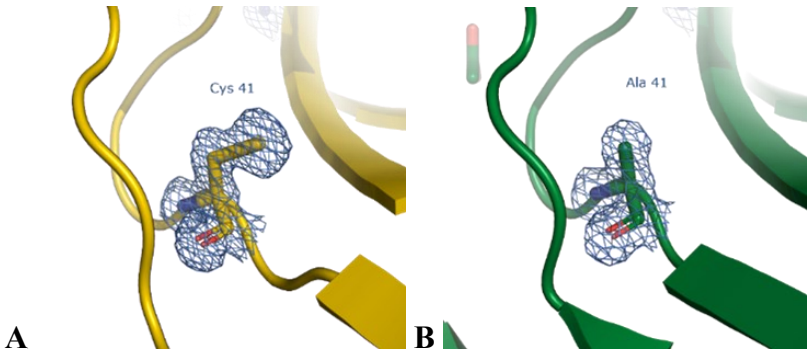

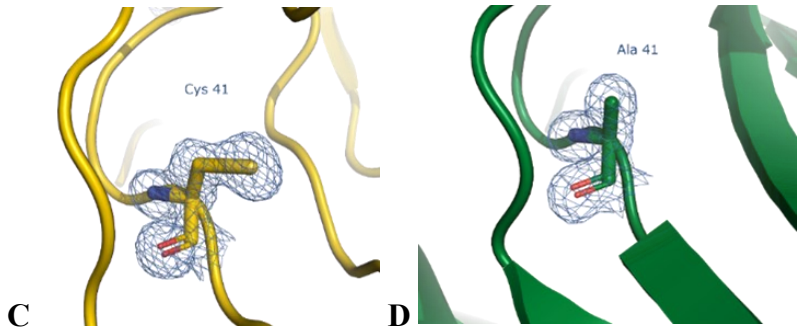

Figure 2.8. 2Fo-Fc electron density map of residue 41 in MNEI (yellow) and Mut9 (green). Chains A are reported in panels A and B, chains B in panel C and D. Electron density is contoured at 1σ.

Details of the distances between residue 41 and residue 62 are reported in **Table 2.6**.

Table 2.6. Distances (Å) between residues 41 and 62 in both molecules of the asymmetric unit of MNEI and Mut9.

	Distance (Å)			
	Residue 41, CA - L62, CA (chain A)	***Residue 41, CB - L62, CD (chain A)***	***Residue 41, CA - L62, CA (chain B)***	***Residue 41, CB - L62, CD (chain B)***
MNEI	5.23	5.04	4.98	5.01
Mut9	5.11	3.66	5.01	3.60

E23A mutation

The E23A mutation is related to a strong increase in thermal stability[61]. pH plays an important role in modulating the stability of MNEI and its mutants. It has been demonstrated that residue E23, buried in a hydrophobic pocket of the protein at one end of the alpha helix, is responsible for a pH dependent stability of the protein, due to its anomalous pKa. In the two chains of the asymmetric unit of MNEI and Mut9, the electron density map of residue 23 is well defined (**Figure 2.9**).

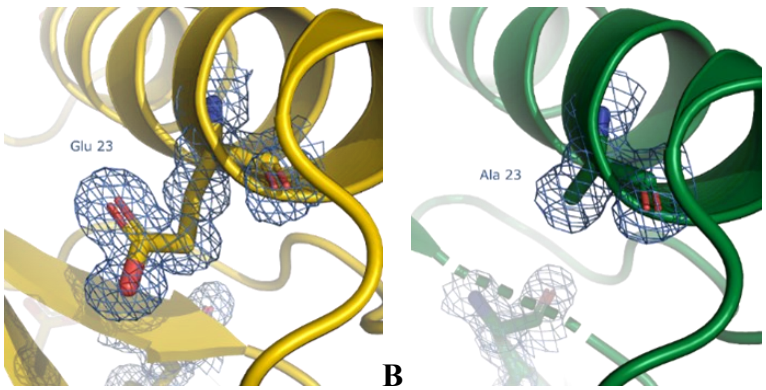

A **B**

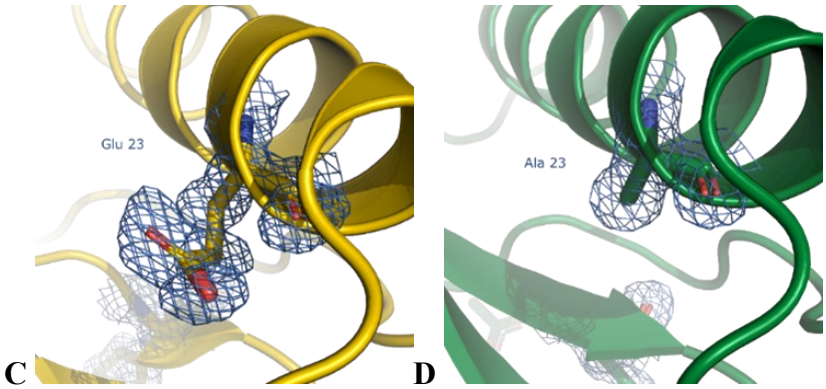

Figure 2.9. 2Fo-Fc electron density map of residue 23 in MNEI (yellow) and Mut9 (green). Chains A are reported in panels A and B, chains B in panel C and D. Electron density is contoured at 1σ.

MNEI structure, notably, shows that the Glu23 side chain is in contact with the residues Ile26, Phe89, Leu86, Tyr29 e Gln28 (**Figure 2.10**) in both molecules of the asymmetric unit, but these interactions are energetically unfavorable. The substitution E23A in Mut9 removes these unfavorable interactions and introduces an empty space around residue 23, which is partly occupied by small displacements of the residues of the hydrophobic pocket.

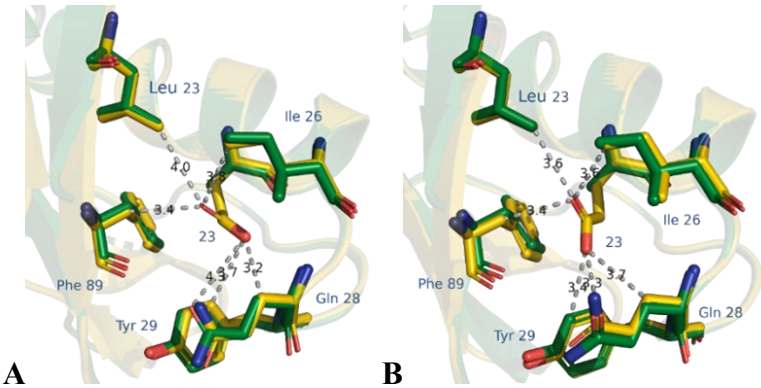

Figure 2.10. Details of the interactions of residue 23 with the surrounding residues in the structures of MNEI (yellow) and Mut9 (green). Chains A are reported in panel A, chains B in panel B. The distances are represented by grey dashes.

The comparison of the distances between Phe89 and A/Glu23 residues are reported in **Table 2.7**. This could contribute to the increased stability of Mut9 with respect to MNEI.

Table 2.7. Distances (Å) between residues 23 and 89 in both molecules of the asymmetric unit of MNEI and Mut9.

	Distance (Å)	
	Residue 23, CA - F89, CA (chain A)	***Residue 23, CA - F89, CA (chain B)***
MNEI	7.12	6.95
Mut9	6.61	6.63

S76Y mutation

Residue 76 is located within the β3 sheet of the protein. Literature results demonstrate that replacing Ser76 with Tyr increases the stability of the protein[62]. Residue 76 is well defined in the electron density maps of MNEI and Mut9 (**Figure 2.11**).

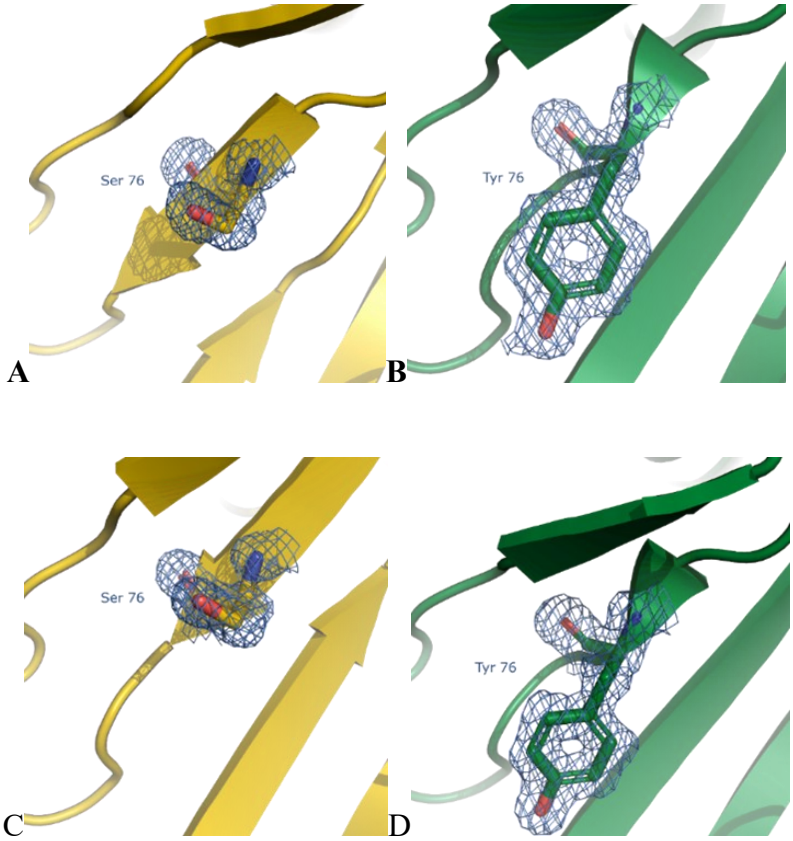

Figure 2.11. 2Fo-Fc electron density map of residue 76 in MNEI (yellow) and Mut9 (green). Chains A are reported in panels A and B, chains B in panel C and D. Electron density is contoured at 1σ.

In the two molecules of MNEI structure, serine forms an unfavorable interaction with the Lys85 atoms and a hydrogen bond with a water molecule (**Figure 2.12**). In the Mut9 structure, the tyrosine side chain forms a hydrogen bond with the carbonyl oxygen of Lys56 and with the side chain of Asp78, although in one of the two molecules of the asymmetric unit this interaction is mediated by the presence of a water molecule (**Figure 2.12**). Tyr76 side chain forms van der Waals interactions with carbon atoms of the residues Ile46, Lys56, Lys85 and Leu87, which are in its neighborhood. All these interactions can make an important contribution in increasing the stability of the mutant with respect to MNEI.

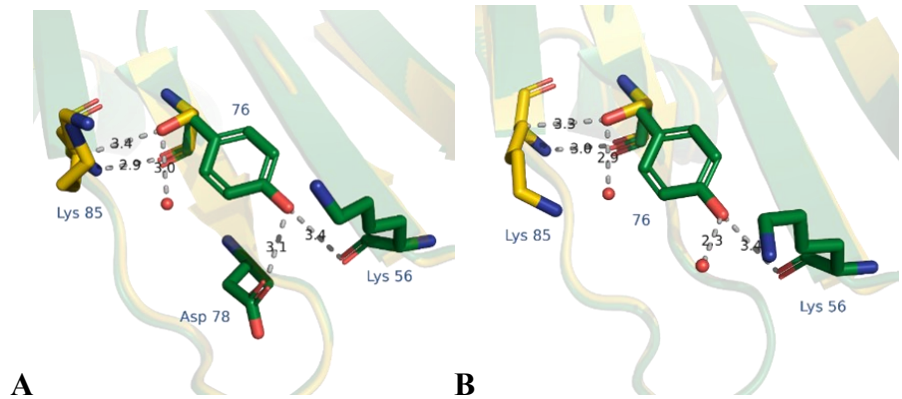

Figure 2.12. Details of the interactions of residue 76 with the surrounding residues in the structures of MNEI (yellow) and Mut9 (green). Chains A are reported in panel A, chains B in panel B. The distances are represented by grey dashes.

The punctual analysis of the additional interactions in Mut9 accounts for the increased thermal stability observed for the protein with respect to the parent MNEI both at acidic and neutral pH[56]. Indeed, the network of stabilizing interactions located in different protein areas counteracts the 4-8 degrees decrease of the melting temperature associated to the mutation Y65R[51], due to the increased distances between residues Tyr63 and Phe94.

The aggregation tendency of Mut9 was studied by standard ThT fluorescence assay and compared to literature data reported for MNEI[51]. The protein was incubated, with and without NaCl, at pH 2.5 and 6.8, at 75 and 90 °C, respectively, *i.e.,* at temperatures corresponding to the early unfolding stages, according to the thermal denaturation study previously reported[56]. Indeed, it has been shown that the partial protein unfolding is a preliminary step for the formation of amyloid-like protein fibrils[63]. The aggregation kinetics was followed for two days, at pH 6.8, and for four days, at pH 2.5, monitoring the ThT fluorescence signal until a stationary phase was reached (**Figure 2.13 A**). The data reported in **Figure 2.13** indicated that ThT fluorescence intensity increases as function of time for all the analyzed samples, but the pH drastically influences ThT binding. Particularly, i) at neutral pH, the signal reached

the plateau after only one day of incubation, and the intensity is lower in comparison with that obtained at acidic pH; ii) at pH 2.5, the *plateau* was reached after two days of incubation. The curves from all the samples show a sigmoidal line-shape, more evident at acidic pH, as expected for amyloid fibrils formation mechanism, which involves three phases, *i.e.*, lag, elongation, and *plateau*[63]. Interestingly, at both pHs, the aggregation process occurs also without NaCl. Nevertheless, the ionic strength affects the kinetic in an opposite way in these two conditions. In fact, at acidic pH the kinetic in the presence of NaCl is faster than that in the absence of NaCl, while, at neutral pH, the ionic strength delays the kinetics. Anyway, quite a high response to ThT assay, under all conditions, suggests the possible presence of fibrillar aggregates. To confirm this hypothesis and to investigate the morphology of the aggregates formed by Mut9, aliquots of the samples incubated for two days at neutral pH and for four days at acidic pH were analyzed by TEM. Representative images of the taken samples are reported in **Figure 2.13** (from **B** to **E**). Differently from MNEI, Mut9 aggregates showed a fibrillar organization at both acidic and neutral pH, independently on the presence of NaCl. However, the quantity and the morphology of the fibrils are influenced by NaCl at both pHs, reflecting the different ThT

fluorescence intensity. In fact, at pH 2.5, in the presence of NaCl the ThT emission is much more intense, suggesting the presence of a higher number of amyloid fibrils. This hypothesis is confirmed by TEM. In fact, as observed in **Figure 2.13 C**, there are more fibrils, and they are more branched in comparison to the fibrils of the sample without salt (**Figure 2.13 B**). On average, the fibrils formed in the presence and in absence of sodium chloride have a diameter of 22 ± 1 nm, while the branches, when present, have a diameter of 14 ± 1 nm. The length of fibrils is about 4 ± 1 μm. On the other hand, at pH 6.8, in the absence and in the presence of NaCl only few, very long fibrils, more branched in the absence of NaCl, can be detected. In fact, as suggested by ThT binding assays, the fluorescence intensity is much lower than that observed at acidic pH. Thus, fibrils dimensions are comparable to those obtained at acidic pH (**Figures 2.13 D-E**).

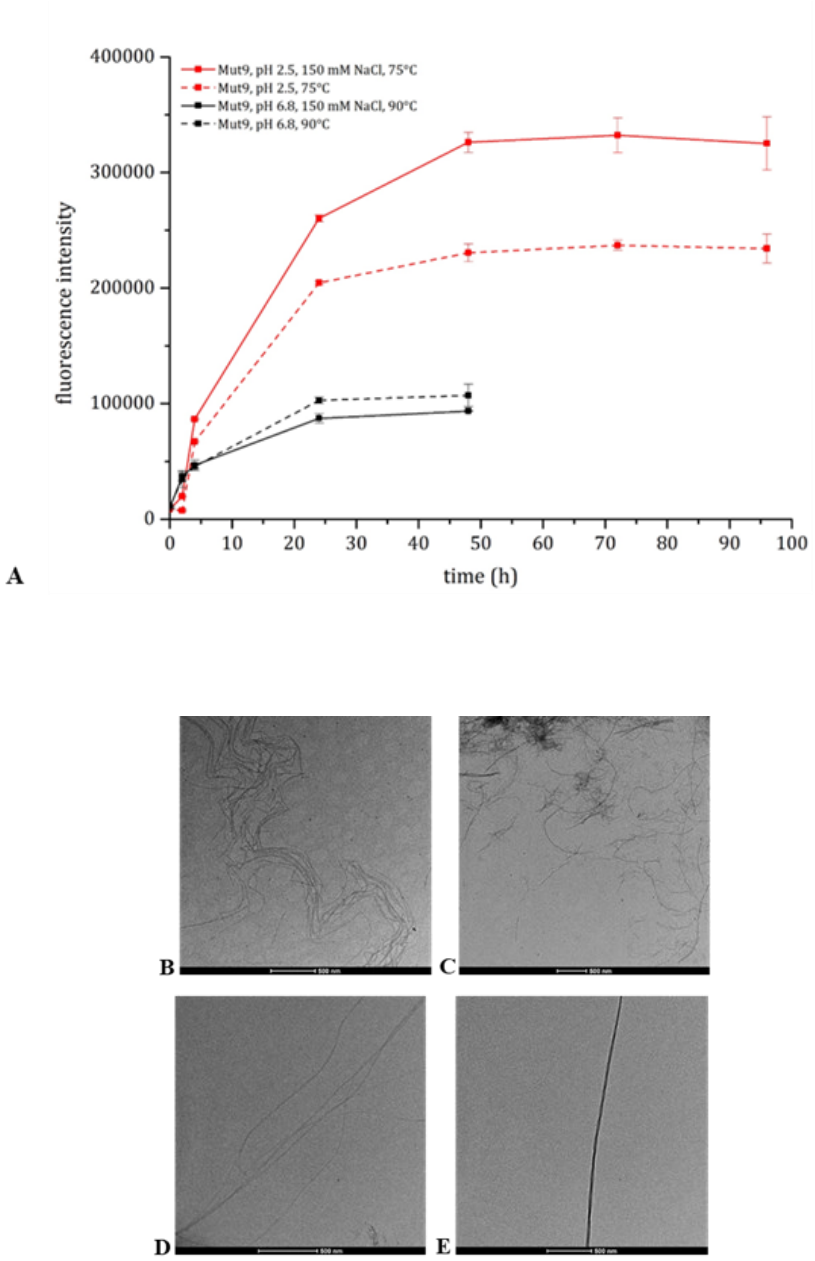

Figure 2.13. ThT binding assay of Mut9 (panel **A**). Fluorescence intensity values are reported as function of time for: Mut9, pH 2.5, NaCl, 75 °C (solid red line), Mut9, pH 2.5, 75 °C (dotted red line), Mut9, pH 6.8, NaCl, 90 °C (solid black line) and Mut9, pH

6.8, 90 °C (dotted black line). Transmission electron images of Mut9 (panels **B-E**). Samples incubated in 20 mM phosphate buffer pH 2.5 at 75 °C after 96 h without (**B**) and with (**C**) 150 mM sodium chloride, and in 20 mM phosphate buffer pH 6.8 at 90 °C after 48 h without (**D**) and with (**E**) 150 mM of sodium chloride. The samples were observed without any staining procedure; therefore, protein fibrils appear darker with respect to the background. The scale bars are 500 nm.

A possible explanation is that in these conditions the net charge of the protein is positive and, upon partially unfolding, at low ionic strength only limited protein orientations exist and lead to an ordered polymerization, making the process slower. High concentrations of NaCl reduce the repulsion between the positively charged side chains on the protein surface, increasing the number of possible relative orientations, and accelerating the aggregation process. At neutral pH the protein net charge is significantly decreased, as the deprotonation of acidic side chains occurs. Under these conditions the influence of the ionic strength on both morphology and microstructure is reduced, as both positive and negative charges are present on the protein surface. Interestingly, less fibrils are observed, probably due to the high incubation temperature necessary to partial unfold the protein and to prompt the aggregation.

The presence of fibrillary aggregates was also investigated by FTIR spectroscopy, which allows to detect the presence of intermolecular β-sheet structures, universally accepted hallmarks of amyloid aggregates[31].

The aggregation kinetics of Mut9 incubated under different conditions, *i.e.* at pH 2.5 and at pH 6.8, both in the absence and in the presence of NaCl, is reported in **Figure 2.14**. At the beginning of incubations (time 0 h), the second derivative spectra of Mut9 (**Figure 2.14 B**) display, in all the reported conditions, the following peaks that were assigned to the secondary structures of the native protein, in agreement with our previous works[53,64]: ~1635 cm^{-1} and ~1691 cm^{-1}, due to intramolecular β-sheets; ~ 1659 cm^{-1}, mainly due to α-helices, with contribution of random coils; ~ 1679 cm^{-1}, assigned to β-turns. During incubation, a downshift of the main Amide I peak (at 1635 cm^{-1}) is observed in all the absorption spectra (**Figure 2.14 A**), albeit with a dissimilar kinetics in the different conditions. As shown in the second derivative spectra (**Figure 2.14 B**), in the samples incubated at pH 6.8 and 90 °C, the components assigned to the native protein structures completely disappear already after 2 and 4 hours in the absence and in the presence of NaCl, respectively. Moreover, two new peaks at around 1695 cm^{-1} and ~ 1618 cm^{-1} appear. These components are unequivocally assigned to the formation of intermolecular β-sheet structures typical of protein aggregates. In the samples incubated at pH 2.5 and 75 °C, starting from 24 hours the ~1635 cm^{-1} peak assigned to the native protein structures

downshifts to ~1625 cm^{-1}, while the ~1691 cm^{-1} peak upshifts to ~1695 cm^{-1}. In the samples incubated at pH 2.5, 150 mM NaCl, the IR signal of the native structure disappears between 4 and 24 hours, and new components at ~1695 cm^{-1} and between 1625-1618 cm^{-1} arise, which can be assigned to the β-sheet structures of the protein aggregates (**Figure 2.14 B**). The second derivative spectra of the protein pellets collected after 48 hours of incubation display similar spectral features for the samples at pH 6.8 and 90 °C in the presence and absence of 150 mM NaCl and for the sample at pH 2.5, 150 mM NaCl at 75 °C. The sample incubated at pH 2.5 and 75 °C displays a different position of the main Amide I peak and a reduced intensity of the ~1695 cm^{-1} peak. For a quantitative comparison, the β-index was evaluated from the second derivative spectra. This index is related to the orientation of the β-strands and it was suggested that it is proportional to the percentage of anti-parallel vs. parallel organization of the β-strands[65]. A lower β-index value (**Figure 2.14 C**) was obtained for the sample at pH 2.5 and 75°C, indicating differences in the internal structures of this aggregates compared to those obtained under the other conditions. In particular, the lower value of the β-index might suggest a higher presence of parallel β-sheet structures in the final aggregates[65]. Moreover, the absorption

spectrum of the final aggregates obtained at pH 2.5 and 75 °C displays a lower absorption around 1660 cm^{-1} (**Figure 2.14 A**), indicating a lower content of disordered structures compared to the aggregates obtained in the other tested conditions.

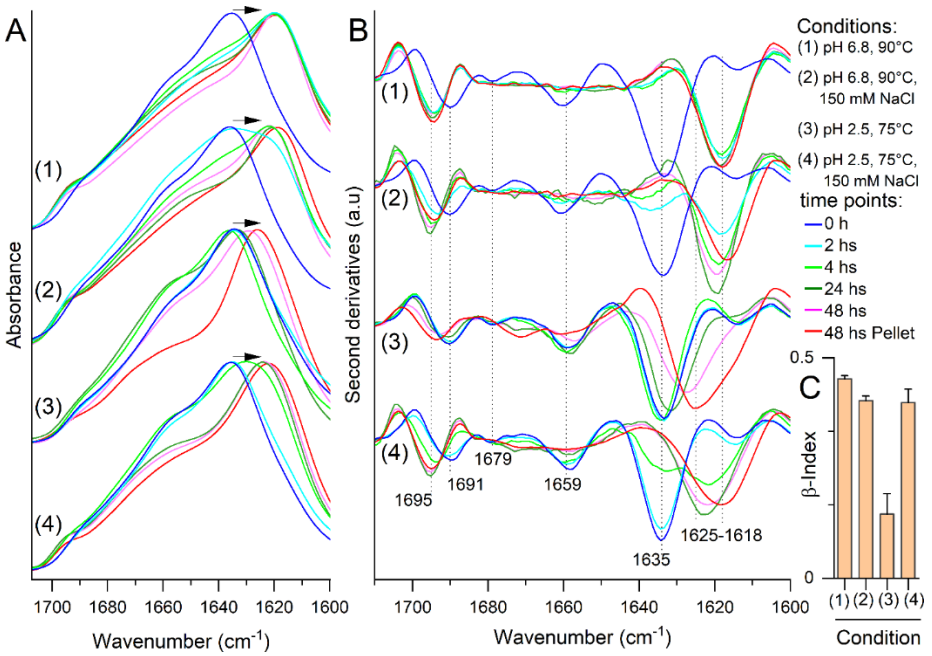

Figure 2.14. Mut9 aggregation characterized by FTIR spectroscopy. **A, B)** Absorption and second derivative spectra of Mut9 incubated under different conditions, specified as (1) to (4), for different times, as indicated. After 48 h of incubation, the spectra of the pellet were also collected. **C)** The β-index of the final aggregates is evaluated from the intensities of the second derivative spectra of the pellets. In particular, the ratio of the ~1695 cm^{-1} peak intensity to that of the maximum peak between 1625-1618 cm^{-1} was reported.

An important result, obtained for the first time for monellin single chain derivatives, is that the fibrils have macroscopic dimensions. In fact, as shown in **Figure 2.15**, Mut9 fibrils are visible to the human eye.

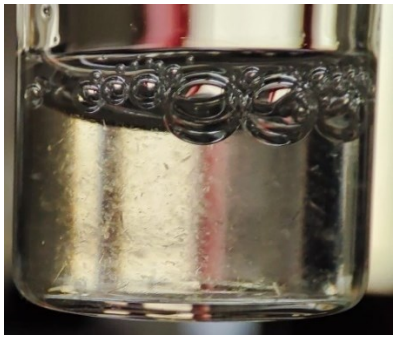

Figure 2.15. Picture of the vial with Mut9 fibrils.

Indeed, thanks to big dimensions, protein fibrils were suitable for SEM data collection. Images reported in **Figure 2.16** show a well-defined fibril long about 400 µm and with a diameter between 14 and 15 µm.

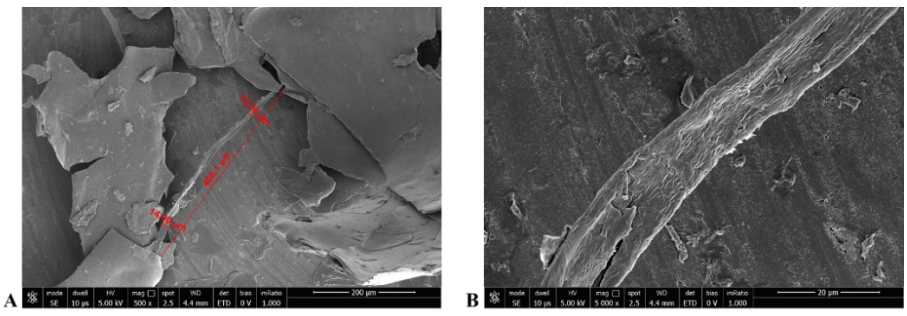

Figure 2.16. SEM images of isolated Mut9 fibrils. In panel **A** length and width dimensions are also reported.

2. Perm1, Perm2, Perm3: circularly permutated MNEI mutants

To evaluate the effect of modifications of the backbone on the folding properties, stability and aggregation propensity of MNEI derivatives, three new mutants, dubbed Perm1, Perm2 and Perm3, were obtained by another approach, *i.e.* circular permutation. The application of this methodology allows the study of the functional significance of specific protein regions, as well as to design proteins with desired properties and to gain insight into the structural consequences of sequence rearrangements, such as reduced proteolytic susceptibility, enhanced catalytic activity, altered substrate or ligand binding, and improved thermostability. In these proteins new termini were introduced through the cleavage of the bond between Gly50 and Phe51 situated in the loop that connect β2 and β3 strands, while the old N and C termini were connected through three different linkers: GGSGG, GGSG and GSG, respectively (**Figure 2.17**).

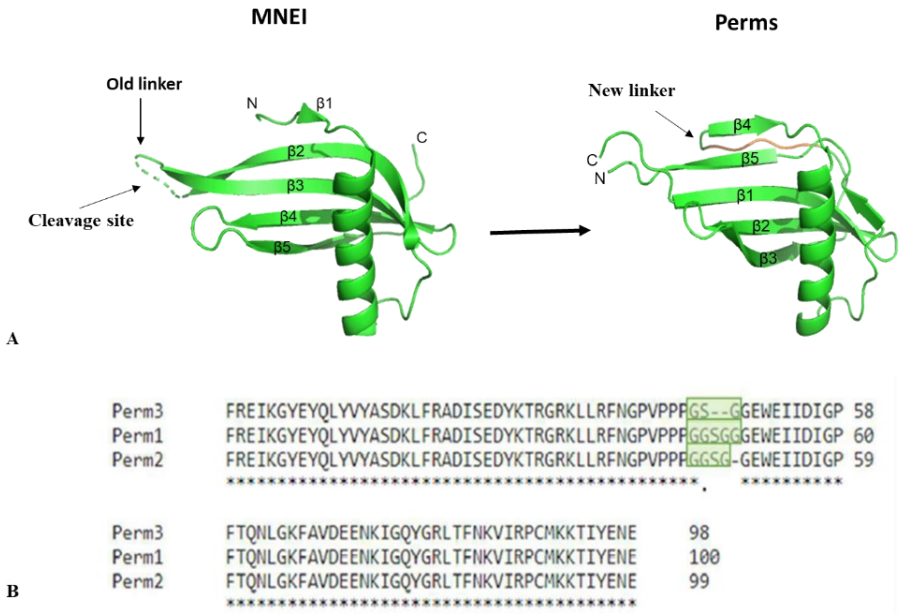

Figure 2.17. A) Schematic representation of the design of Perm1, Perm2 and Perm3. In green is represented the linker that connects the old termini. **B)** Amino acidic sequence of Perm1, Perm2 and Perm3 mutants. In green are highlighted the residues of the different linkers.

The three designed mutants were expressed, purified, and characterized in the laboratory of Professor L.O. Essen at Marburg University, in Germany. Gel filtration chromatograms of the three Perm mutants, reported in **Figure 2.18**, revealed differences in their tendency to spontaneously form dimeric or higher oligomeric forms, in particular in the case of Perm3. Indeed, Perm1 was isolated as a pure monomer as showed by the presence of a single peak in its chromatogram (**Figure 2.18 A**). In Perm2, only a very small percentage of protein was eluted as

dimer with respect to the respect to the monomer (**Figure 2.18 B**). While Perm3 displayed the highest propensity to oligomerize since almost equal quantities of monomer and dimer were obtained together with a small amount of oligomeric species of higher molecular weight (**Figure 2.18 C**).

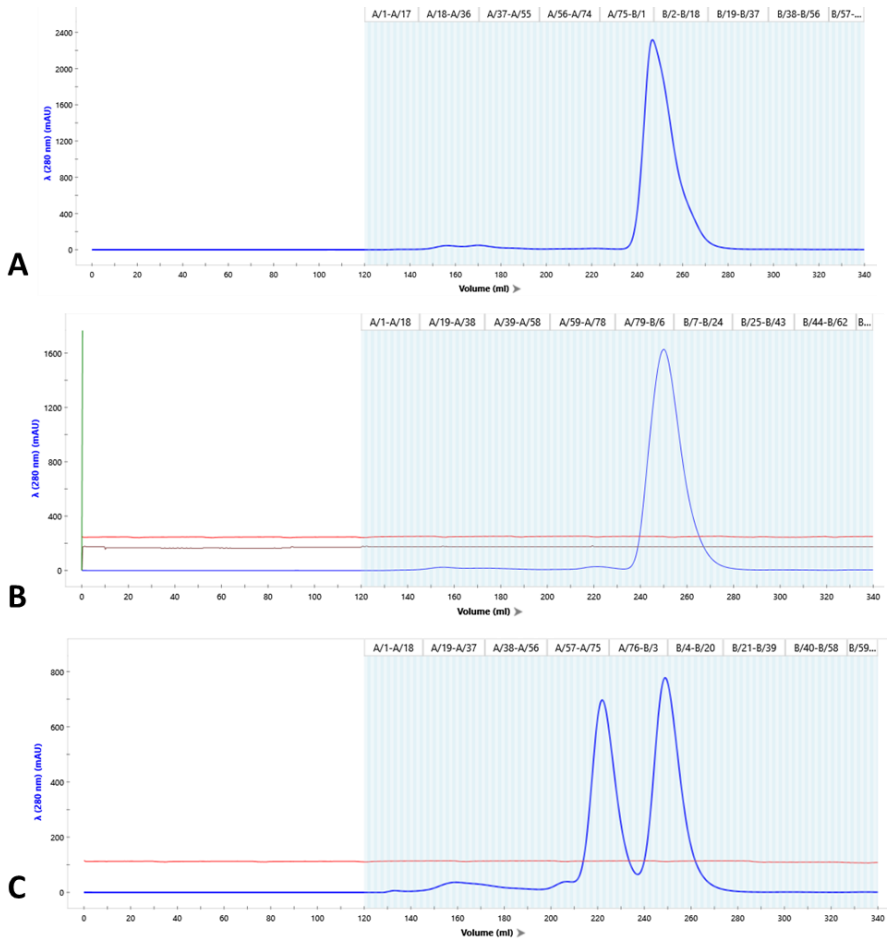

Figure 2.18. Gel filtration chromatogram on a Superdex 75 26/60 of **A)** Perm1, **B)** Perm2, and **C)** Perm3 in 50 mM sodium acetate buffer pH 5.5 and 150 mM NaCl.

As in the case of Mut9, has been run for the Perm proteins, the grounds of their different propensity to form dimers or oligomeric species have been searched by investigating their stability, both in solution and at solid state, by circular dichroism spectroscopy and X-ray crystallography. In addition, the interconversion from monomer to dimer/oligomer was investigated for all three proteins. The analysis of the thermal stability is a preliminary step to define the experimental conditions useful for protein fibrils formation. To allow a direct comparison with the parent protein, the thermal stability of Perm mutants has been evaluated at pH 2.5 in presence of 150 mM of NaCl (**Figure 2.19**), *i.e.* in the condition already used to obtain MNEI fibrils.

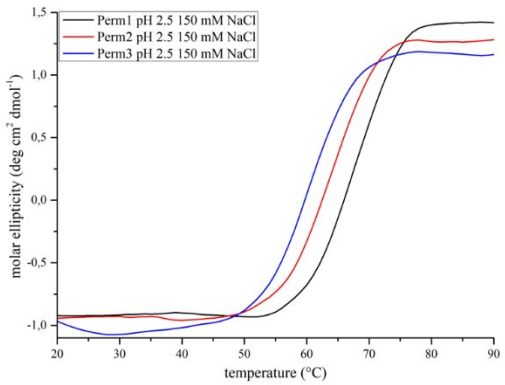

	T_m (°C)
MNEI	72 ± 1
Perm1	67 ± 1
Perm2	61 ± 1
Perm3	58 ± 1

Figure 2.19. Thermal denaturation profiles of Perm1, Perm2 and Perm3 at pH 2.5 in the presence of 150 mM NaCl. Comparison between the denaturation temperatures of MNEI and Perm mutants are reported in the table.

Firstly, the three perms were incubated at 55°C in presence of salt. In these experimental conditions, each protein has an unfolding percentage between 10 and 25%. For comparison, also MNEI was incubated in the same experimental conditions, even though is completely folded at this value of temperature. The aggregation kinetics was followed for 4 days taking sample aliquots at different times and analyzing them via ThT binding assay (**Figure 2.20**). As expected, the assay showed that MNEI had the lowest emission fluorescence intensity compared to those of its mutants. Thus, the lag-phase of Perm1 is comparable to that of MNEI, as the ThT fluorescence emission increases only slightly during the first 2 hours. In contrast, at the same time-interval, the intensity of the ThT emission upon binding to Perm2 and Perm3 reached about 50% of the plateau point. Although the aggregation kinetics of MNEI and Perm1 are comparable, the ThT fluorescence of Perm1 reached highest values. All mutants reached the plateau within 24 hours of incubation.

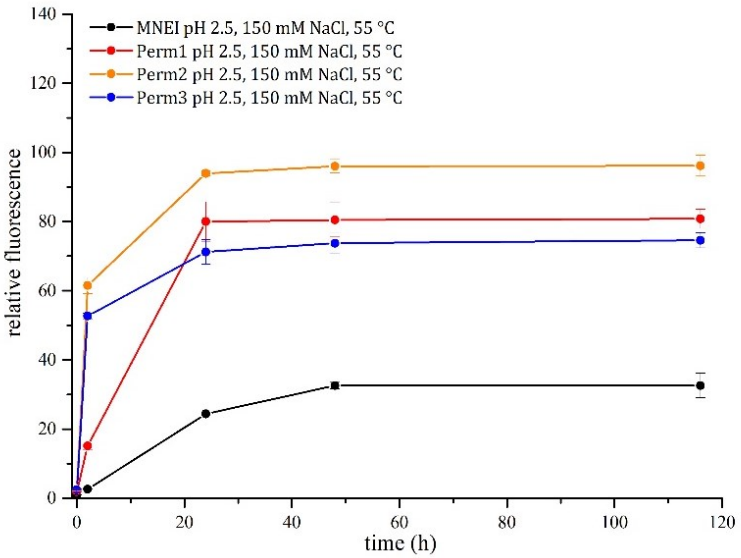

Figure 2.20. Time course of ThT binding assay of MNEI and Perm mutants incubated at 55°C. Fluorescence emission was recorded at 485 nm at the indicated times. The reported fluorescence curves represent the mean calculated on the values obtained by a sample triplicate. The error bars represent the standard deviation.

The morphology of Perm aggregates was characterized via transmission electron microscopy (TEM). Sample aliquots were taken at the end of the kinetic. The results (**Figure 2.21**) highlighted different types of aggregates. Interestingly only Perm1 produced mature fibrils, very long and, in each filament, the fibrils pair to each other (**Figure 2.21 A**). Perm2 and Perm3 form mostly amorphous aggregates. However, for Perm2, a few short fibrils emerge from the amorphous aggregates (**Figure 2.21 B**), while for Perm3, the amount of isolated fibrils is even lower (**Figure 2.21 C**).

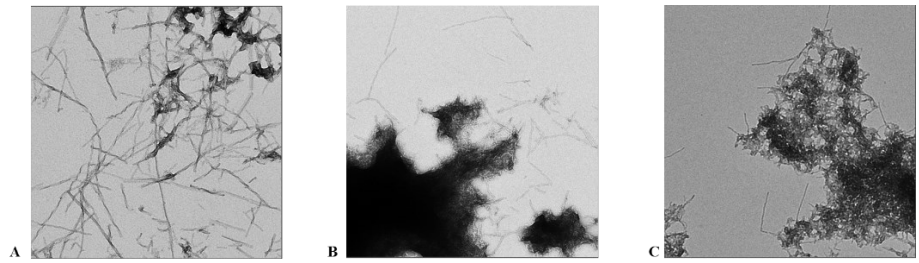

Figure 2.21. Transmission electron microscopy images of Perm1 (**A**), Perm2 (**B**), and Perm3 (**C**) after 96 hours of incubation, at 55°C in 20 mM sodium phosphate buffer containing 150 mM NaCl. The samples were prepared using uranyl acetate as negative staining at 1 %.

To better understand the different results obtained by ThT assay and TEM for Perm1 to the respect of Perm2 and Perm3, a kinetic study of the interconversion of each protein from monomer to dimer was conducted. In particular, the three proteins were incubated at 55 °C and pH 2.5 in the presence of 150 mM NaCl. Aliquots of each sample were taken after different incubation times and analyzed by size exclusion chromatography (**Figure 2.22**). The chromatogram of Perm1 (**Figure 2.22 A**) showed that the protein stays as a monomer for the first four hours of incubation at least, while after 24 h no soluble form can be detected in the chromatogram, suggesting a quantitative conversion in the fibrillar aggregates, observed by ThT assays and TEM images. In the case of Perm2 and Perm3 (**Figure 2.22 B-C**), just after 2 h incubation, most of the protein in solution precipitates, preventing further measures.

This result, combined with ThT and TEM results, suggests a fast unfolding, which is responsible for the presence of a consistent quantity of amorphous aggregates and only few dispersed fibrils.

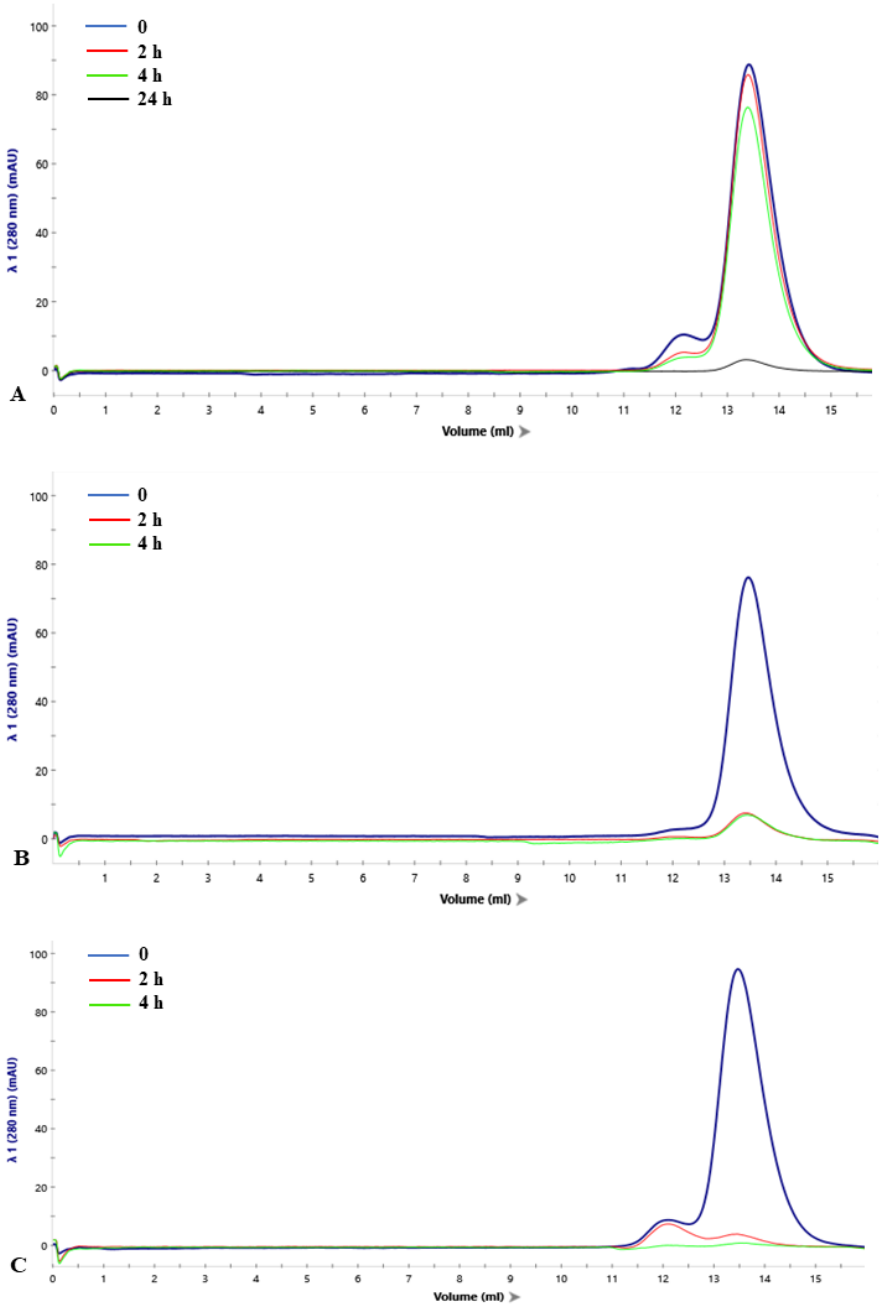

Figure 2.22. Gel filtration chromatogram on a Superdex 75 10/300 of **A)** Perm1, **B)** Perm2, and **C)** Perm3 in 50 mM sodium acetate buffer pH 5.5 and 150 mM NaCl.

Based on this hypothesis, the incubation temperature for Perm2 and Perm3 were decreased at 50 °C to try to slow the aggregation process and to obtain better fibrillar aggregates. Also in this case, Perm2 and Perm3 were incubated at pH 2.5 in the presence of sodium chloride. For comparison, also Perm1 was incubated in the same experimental conditions, even though it is completely folded at this value of temperature. The aggregation kinetics were followed for 4 days taking sample aliquots at different times and analyzing them via ThT binding assay (**Figure 2.23**). As expected, ThT binding assay showed that Perm1 had a slower kinetic in comparison to the one at 55 °C, probably due to a low unfolded protein percentage. In particular, the ThT fluorescence emission did not increase during the first 6 hours for Perm1, while at the same time interval, reached about 50% of the plateau point upon binding to Perm2 and Perm3. Moreover, Perm2 and Perm3 reached the plateau within 24 hours of incubation, while Perm1 within 48 hours.

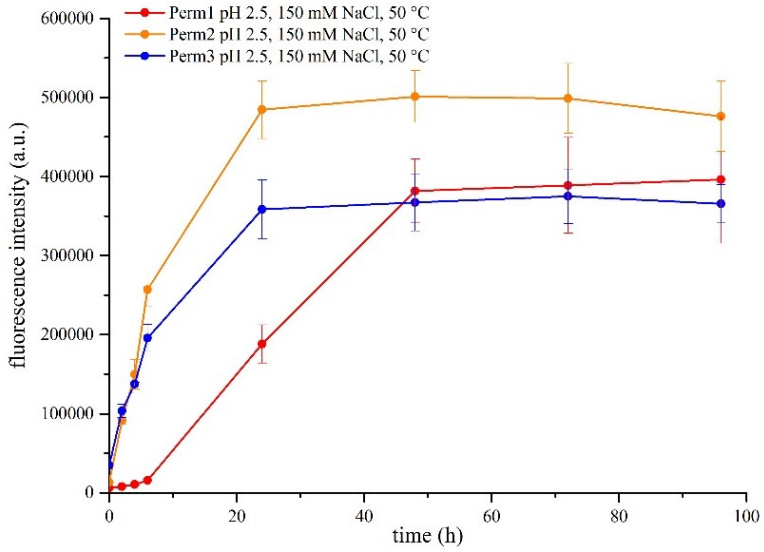

Figure 2.23. Time course of ThT binding assay of Perm1, Perm2 and Perm3 incubated at 50 °C. Fluorescence emission was recorded at 485 nm at the indicated times. The reported fluorescence curves represent the mean calculated on the values obtained by a sample triplicate. The error bars represent the standard deviation.

Also in this case, the morphology of Perm aggregates was investigated by TEM. Sample aliquots were taken at the end of the kinetic. The results (**Figure 2.24**) confirmed that Perm1 forms isolated fibrils even at this temperature even if they are much smaller in length and diameter than those obtained 55 °C (**Figure 2.24 A**). On the other hand, this temperature condition seems to reduce the tendency of Perm2 and Perm3 to form fibrils, as only amorphous aggregates are present in both samples (**Figure 2.24 B-C**). These data suggest that protein monomers could

prompt the formation of fibrillar aggregates while dimeric or oligomeric forms are off pathway toward amyloid aggregation.

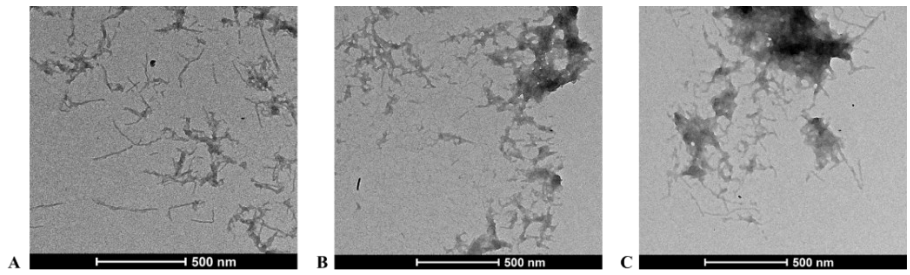

Figure 2.24. Transmission electron microscopy images of Perm1 (**A**), Perm2 (**B**), and Perm3 (**C**) after 96 hours of incubation, at 50 °C in 20 mM sodium phosphate buffer containing 150 mM NaCl. The samples were observed without any staining procedure; therefore, protein fibrils appear darker with respect to the background. The scale bars are 500 nm.

To confirm this hypothesis, all the three proteins were incubated in the same conditions at 50 °C for 3 hours. Samples aliquots were taken and analyzed by polyacrylamide gel electrophoresis (PAGE) under native conditions. Aliquots of each mutant were loaded on the gel before thermal treatment. The result (**Figure 2.25**) clearly showed that Perm1 and Perm2 are mostly present in solution as monomer and dimer, although small fractions of oligomers are present. Conversely, Perm3 is mainly a dimer in solution with a larger amount of other oligomeric forms to the respect of Perm1 and Perm2. Remarkably, after the

incubation at 50 °C, Perm1 remains in solution as a monomer, Perm2 as a monomer with a very small fraction of dimer, and Perm3 half as a monomer and half as a dimer. The tendency of each mutant to form dimer in solution exactly reflects their ability to form fibrils, confirming that the dimeric or oligomeric forms are off pathway toward amyloid fibrillation.

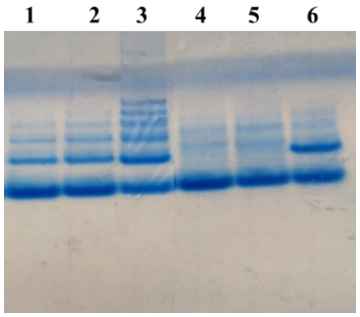

Figure 2.25. Gel electrophoresis under native condition of: Perm1 at pH 2.5 before thermal treatment (*lane 1*); Perm2 at pH 2.5 before thermal treatment (*lane 2*); Perm3 at pH 2.5 before thermal treatment (*lane 3*); Perm1 at pH 2.5 after thermal treatment at 50 °C for 3 h (*lane 4*); Perm2 at pH 2.5 after thermal treatment at 50 °C for 3 h (*lane 5*); and Perm3 at pH 2.5 after thermal treatment at 50 °C for 3 h (*lane 6*).

As for Mut9, also for Perm mutants a structural characterization has been carried out by mean of X-ray crystallography. The monomeric form of Perm1 and the dimer of Perm3 have been crystalized and X-ray diffraction data have been collected. Surprisingly, crystals of Perm1 grew in few months, while crystals of Perm3 dimer in only two days.

The structures will be solved and refined in the laboratory of Professor Essen. However, a first inspection to both structures showed the presence of swapped dimers in the asymmetric unit (**Figure 2.25**). The swapped dimers are quite different, in particular at the dimeric interface. As shown in **Figure 2.25**, Perm1 swapped structure has a smaller interface compared to that of Perm3, maybe due to the different length of the linkers. These features could be responsible for the diverse stability of Perm1 and Perm3 dimers. The larger interface and the shorter linker, in fact, make the dimer the most stable form of Perm3 in solution. In conclusion, the structural analysis allowed once again to affirm that the dimeric form is off pathway for the fibrillation process and to clarify the different aggregation behavior of two very similar protein mutants.

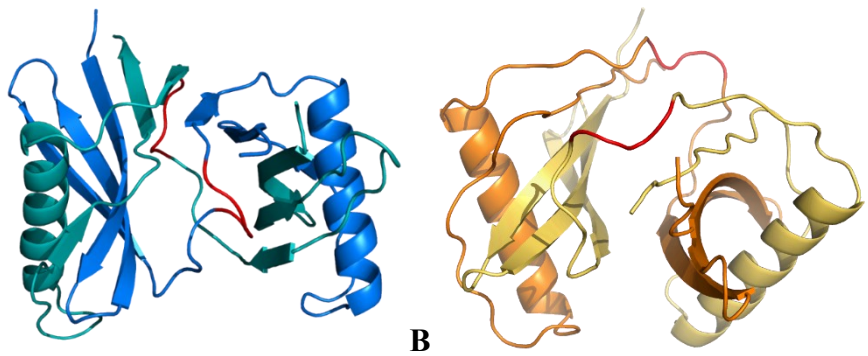

Figure 2.25. Cartoon representation of X-ray structures of Perm1 and Perm3. Chains A of each monomer of the asymmetric unit are colored in teal green (Perm1) and orange

(Perm3), while chains B in light blue and yellow (Perm3). The position of the mutated residues is indicated in red.

Domain swapping is a process by which two or more protein molecules exchange identical structural elements to form dimers or higher oligomers[66].

MATERIALS AND METHODS

1. Expression of MNEI and its mutants

MNEI and its mutants were expressed in *Escherichia Coli* BL21(DE3). Bacterial cells were transformed with plasmid pET22b+ transferring the gene encoding for each protein. Cells were cultured on LB/Agar containing ampicillin (Amp) 100 mg L^{-1} over night at 37 °C. Afterwards, a single colony was resuspended in LB medium with the same antibiotic overnight at 37 °C, then the starter culture was diluted 1:100 (v/v) into LB/Amp and incubated at 37 °C. Protein expression was induced at 0.8 OD_{600}/mL by adding lactose 5 mM and carried on overnight at 25 °C. Finally, the cells were harvested by centrifugation (4 °C, 8000 rpm, 30'), washed with pure water and stored frozen until protein purification.

2. Purification of MNEI and its mutants

To extract and purify the protein, cells were resuspended in sodium acetate 50 mM at pH 5.5 and sonicated on ice with a Microson Ultrasonic Homogenizer XL2000 for 30' (30'' on 30'' off). Since these proteins are soluble after sonication, the supernatant was recovered by centrifugation (4 °C, 12 000 rpm, 30'). The purification of MNEI and Mut9 was carried-out by loading the supernatant on a Macro-Prep High S cationic exchanger column (5 mL, Bio-Rad). The chromatography was monitored by UV absorbance at 280 nm. After loading, the column was washed up to absorbance baseline and the proteins were eluted by using a NaCl step gradient (50,100,150 and 200 mM) in sodium acetate 50 mM, pH 5.5. The fractions containing proteins were pooled and desalted by Size Exclusion Chromatography on a Sephadex G-25 column (GE Lifesciences) eluted with acetic acid 100 mM. Then, the fractions containing the desalted protein were pooled and freeze-dried. On the other hand, Perm1, Perm2 and Perm3 purifications required one more step in comparison with the one of MNEI or/and Mut9. In fact, in this case, after elution with 150 mM of sodium chloride in sodium acetate 50 mM at pH 5.5, fractions containing proteins were collected and loaded on Superdex 75 26/60 and eluted in sodium acetate 50 mM, pH 5.5 in the

presence of 150 mM of NaCl. The fractions containing the monomeric protein were pooled together, dialyzed against acetic acid 100 mM, and subjected to lyophilization. Purity of MNEI and its mutants was assessed by SDS Polyacrylamide Gel Electrophoresis. Proteins yields were estimated by UV absorbance at 280 nm and corresponds to about 35 mg per liter of LB medium.

3. Circular dichroism spectroscopy

Circular dichroism (CD) measurements were performed on a Jasco J-810 spectropolarimeter (JASCO Corp., Milan, Italy) at 25 °C. Quartz cells with path length of 0.1 cm and a protein concentration of 0.1 mg mL^{-1} were used. Thermal unfolding profiles were obtained by monitoring the CD signal at 215 nm as function of temperature, in the range 20–100 °C, with a heating rate of 1.0 °C min^{-1}. Each curve of denaturation was obtained averaging three independent measurements. Other experimental settings were: 50 nm min^{-1} scan speed, 2.0 nm band width, 1.0 nm resolution, 50 mdeg sensitivity, and 2 s response.

4. Crystallization, X-ray diffraction data collection, structure solution and refinement

MNEI and Mut9 were crystalized at 293 K by hanging drop vapor diffusion and a reservoir solution containing 30-33% PEG4K, 0.1 M sodium acetate buffer pH 4.5 and 0.2 M ammonium sulfate mixing 1 µL protein (4.5 and 5.7 mg mL^{-1} in 5.0 mM HCl, respectively) with 1 µL mother liquor at 20 °C. Crystals grew within one week (**Figure 2.26**).

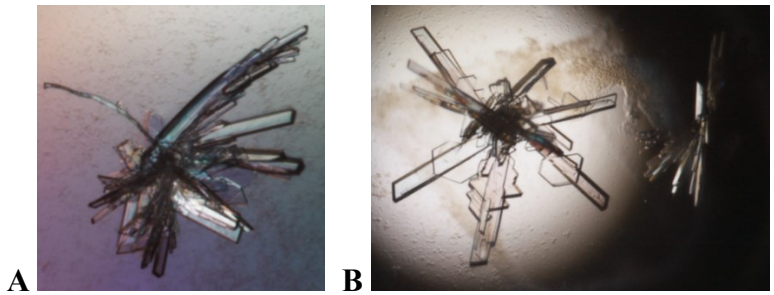

Figure 2.26. Crystals of MNEI (A) and Mut9 (B).

X-ray diffraction data were collected at 100 K on a Pilatus detector at XRD2 beamline of Elettra synchrotron, Trieste, Italy. Data collection statistics are reported in Table S7. Data were processed and scaled in $P12_11$ space group using AutoPROC[67]. Phase problem was solved by molecular replacement method using as starting model the structure from protein data bank (PDB) (2O9U). Refinement was carried out using

Refmac-CCP4i[68] and model building using Coot[69]. Refinement statistics are reported in **Table 2.8**. Coordinates and structure factors have been deposited in the protein data bank under the accession codes 8Q0S and 8Q0R, respectively.

Table 2.8. Data collection and refinement statistics.

Data collection statistics		
Protein	MNEI	Mut9
PDB code		
Space group	P1	P1
Unit cell parameters **a, b, c (Å)** **α, β, γ (°)**	31.65, 38.97, 44.13 106.00, 109.52, 103.36	31.72, 39.35, 43.89 105.35, 109.33, 103.23
Molecules in the asymmetric unit	2	2
Observed reflections	179068 (8015)	91391 (3387)
Unique reflections	52760 (2446)	27470 (1225)
Resolution (Å)	38.39 – 1.19 (1.21 - 1.19)	35.58 – 1.50 (1.53 – 1.50)
Completeness (%)	92.7 (85.4)	94.7 (84.6)
Rmerge	0.037 (0.679)	0.043 (0.489)
Rpim	0.024 (0.443)	0.028 (0.360)
Rmeas	0.044 (0.815)	0.052 (0.612)
I/I(σ)	14.2 (2.1)	16.3 (2.3)
Multiplicity	3.4(3.3)	3.3 (2.8)
$CC_{1/2}$	0.999(0.726)	0.999 (0.690)
Refinement statistics		
Resolution (Å)		
N° reflection (working set)	38.39 - 1.19	35.58 – 1.50

N° reflection (test set)	47541	25065
N° non-H atoms (refinement)	2337	1541
Rfactor/Rfree	0.218/0.256	0.233/0.274
r.m.s.d. from ideality		
r.m.s.d. bonds	0.012	0.010
r.m.s.d. angles (°)	1.768	1.625

†Rmerge= Σ hΣi |I(h,i)-<I(h)>|/ Σ hΣi I(h,i), where I(h,i) is the intensity of the i^{th} measurement of reflection h and <I(h)> is the mean value of the intensity of reflection h. Criteria used in determination of resolution cut: Rpim <= 0.6000; I/σI >= 2.00; $CC_{(1/2)}$ >= 0.3000
* Values in parenthesis refer to highest resolution shell

Perm1 and Perm3 have been crystallized by hanging drop vapor diffusion using a reservoir containing 30% PEG 4K and 0.2 M tri-sodium citrate buffer pH 5.5 and mixing 0.3 µL of protein solution (6.0 mg mL^{-1}) and 0.3 µL of reservoir. Perm1 crystals appeared within one month while those of Perm3 after only two days. Crystals were fished and cryo-protected with 15% glycerol and X-ray data were collected.

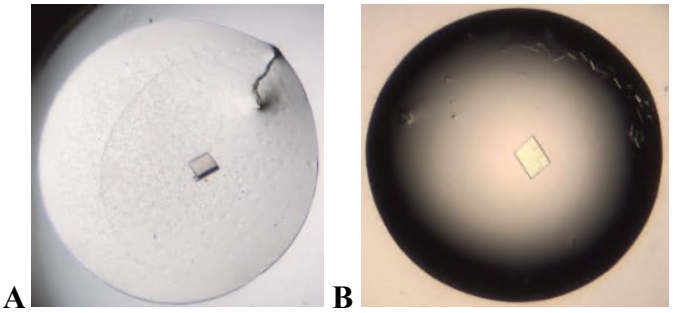

Figure 2.27. Crystals of Perm1 (**A**) and Perm3 (**B**).

5. ThT binding assay

MNEI and Mut9

MNEI at a concentration of 216 μM (2.5 mg mL^{-1}) was incubated in 20 mM phosphate buffer at pH 2.5, while Mut9, at the same concentration, was incubated in 20 mM phosphate buffer at pH 2.5 and 6.8 either with or without 150 mM NaCl. The aggregation kinetics was followed by ThT binding assay as function of time. Thioflavin T (ThT) was dissolved in 20 mM phosphate buffer pH 6.8 to prepare a stock solution of 1 mM. At different time points 19 μL of each incubated samples (final protein concentration 10 μM) were withdrawn and added to 12 μL of ThT stock solution (final concentration 30 μM) and 20 mM phosphate buffer pH 6.8, up to a final volume of 400 μL. Fluorescence emission spectra were recorded on a HORIBA Fluoromax-4 in the range of 400-600 nm with scan speed of 100 nm/min, upon excitation at 440 nm. Excitation and emission slits were both set at 5 nm. Fluorescence intensity values at 485 nm emission were plotted as a function of time. The reported values represent the average of three independent experiments.

Perm mutants

Fluorescence ThT assay was performed at the University of Marburg, using a RF-5301PC fluorescence spectrometer equipped with a thermostat bath. Spectra were registered at 20°C. MNEI and Perms were incubated at a concentration of 0.1 mg Ml^{-1} in 20 mM sodium phosphate buffer pH 6.8 with ThT in a molar ratio 1:3. Fluorescence spectra were recorded after different incubation times. Data reported fluorescence intensity as function of time. λex was 440 nm, while λem was 485 nm.

6. Transmission electron microscopy (TEM) analysis

MNEI and Mut9

Aliquots of the protein solution were taken and diluted 50 times with deionized water. 3 μL drops of the samples were deposited for 3 minutes on a carbon-coated copper TEM grid (200 mesh) and then, the excess fluid was drained off with filter paper and air-dried. Average fibril thickness was calculated from TEM images using IMAGE J (*ImageJ (nih.gov)*). The images were collected using a FEI TECNAI G2 S-twin apparatus operating at 120 kV (LaB_6 source).

Perm mutants

TEM images were recorded using a 200 kV FEI Tecnai G2 electron microscope applying a voltage of 120 kV. For hHFt 3 µl drop of the diluted sample was deposited on a carbon-coated copper grid. After 2 minutes of incubation the excess water was removed with a filter paper. 3 µl of staining, 1.5% PTA, were added to the grid for 4 minutes. Finally, the samples were dried for a few hours. MNEI and Perm1 images were recovered in collaboration with the University of Marburg.

7. FTIR spectroscopy

FTIR measurements in attenuated total reflection (ATR) mode were performed in the mid-IR range as previously described [53,64]. In particular, 2 µL of the samples were deposited on the single reflection diamond crystal of the ATR device (Quest, Specac) and dried at room temperature before the collection of the ATR-FTIR spectra by the Varian 670-IR spectrometer (Varian Australia Pty Ltd.). The following parameters were employed: spectral resolution of 2.0 cm^{-1}, scan speed of 25 kHz, 1024 scan coadditions, and nitrogen-cooled Mercury Cadmium Telluride detector. After 48 hours of incubation, samples were centrifuged at

16000 rcf for 30 minutes and the ATR-FTIR spectra of the pellets were collected as described above. Absorption spectra were smoothed using the Savitsky-Golay method before the second derivative analysis. Spectral collection and analysis were performed with the Resolutions-Pro software (Varian Australia Pty Ltd., Mulgrave VIC, Australia).

8. Kinetics of interconversion of Dimeric forms of Perms

Perm mutants were incubated at 55 °C and pH 2.5 at a protein concentration of 2.5 mg mL^{-1} and 150 mM sodium chloride. Aliquots of each protein were taken at different incubation times, filtered, and loaded on Superdex 75 10/300.

REFERENCES

(1) Jucker, M.; Walker, L. C. Self-Propagation of Pathogenic Protein Aggregates in Neurodegenerative Diseases. *Nature* **2013**, *501* (7465), 45–51. https://doi.org/10.1038/nature12481.

(2) Missmahl, H.-P.; Hartwig, M. Polarisationsoptische Untersuchungen an der Amyloidsubstanz. *Virchows Arch. path Anat.* **1953**, *324* (4), 489–508. https://doi.org/10.1007/BF00954791.

(3) Kumar, S.; Udgaonkar, J. B. Mechanisms of Amyloid Fibril Formation by Proteins. *Current Science* **2010**, *98* (5), 639–656.

(4) Sunde, M.; Serpell, L. C.; Bartlam, M.; Fraser, P. E.; Pepys, M. B.; Blake, C. C. F. Common Core Structure of Amyloid Fibrils by Synchrotron X-Ray Diffraction 1 1Edited by F. E. Cohen. *Journal of Molecular Biology* **1997**, *273* (3), 729–739. https://doi.org/10.1006/jmbi.1997.1348.

(5) Klunk, W. E.; Jacob, R. F.; Mason, R. P. [19] Quantifying Amyloid by Congo Red Spectral Shift Assay. In *Methods in Enzymology*;

Elsevier, 1999; Vol. 309, pp 285–305. https://doi.org/10.1016/S0076-6879(99)09021-7.

(6) Naiki, H.; Higuchi, K.; Hosokawa, M.; Takeda, T. Fluorometric Determination of Amyloid Fibrils in Vitro Using the Fluorescent Dye, Thioflavine T. *Analytical Biochemistry* **1989**, *177* (2), 244–249. https://doi.org/10.1016/0003-2697(89)90046-8.

(7) Kheterpal, I.; Zhou, S.; Cook, K. D.; Wetzel, R. Aβ Amyloid Fibrils Possess a Core Structure Highly Resistant to Hydrogen Exchange. *Proc. Natl. Acad. Sci. U.S.A.* **2000**, *97* (25), 13597–13601. https://doi.org/10.1073/pnas.250288897.

(8) Yamaguchi, K.; Katou, H.; Hoshino, M.; Hasegawa, K.; Naiki, H.; Goto, Y. Core and Heterogeneity of B2-Microglobulin Amyloid Fibrils as Revealed by H/D Exchange. *Journal of Molecular Biology* **2004**, *338* (3), 559–571. https://doi.org/10.1016/j.jmb.2004.02.067.

(9) Kheterpal, I.; Williams, A.; Murphy, C.; Bledsoe, B.; Wetzel, R. Structural Features of the Aβ Amyloid Fibril Elucidated by Limited

Proteolysis. *Biochemistry* **2001**, *40* (39), 11757–11767. https://doi.org/10.1021/bi010805z.

(10) Serpell, L. C.; Sunde, M.; Benson, M. D.; Tennent, G. A.; Pepys, M. B.; Fraser, P. E. The Protofilament Substructure of Amyloid fibrils11Edited by F. E. Cohen. *Journal of Molecular Biology* **2000**, *300* (5), 1033–1039. https://doi.org/10.1006/jmbi.2000.3908.

(11) Sunde, M.; Blake, C. The Structure of Amyloid Fibrils by Electron Microscopy and X-Ray Diffraction. In *Advances in Protein Chemistry*; Elsevier, 1997; Vol. 50, pp 123–159. https://doi.org/10.1016/S0065-3233(08)60320-4.

(12) Bauer, H. H.; Aebi, U.; Häner, M.; Hermann, R.; Müller, M.; Arvinte, T.; Merkle, H. P. Architecture and Polymorphism of Fibrillar Supramolecular Assemblies Produced by in Vitro Aggregation of Human Calcitonin. *Journal of Structural Biology* **1995**, *115* (1), 1–15. https://doi.org/10.1006/jsbi.1995.1024.

(13) Saiki, M.; Honda, S.; Kawasaki, K.; Zhou, D.; Kaito, A.; Konakahara, T.; Morii, H. Higher-Order Molecular Packing in Amyloid-like Fibrils Constructed with Linear Arrangements of

Hydrophobic and Hydrogen-Bonding Side-Chains. *Journal of Molecular Biology* **2005**, *348* (4), 983–998. https://doi.org/10.1016/j.jmb.2005.03.022.

(14) Caughey, B.; Lansbury, P. T. P ROTOFIBRILS , P ORES , F IBRILS, AND N EURODEGENERATION : Separating the Responsible Protein Aggregates from The Innocent Bystanders. *Annu. Rev. Neurosci.* **2003**, *26* (1), 267–298. https://doi.org/10.1146/annurev.neuro.26.010302.081142.

(15) Bitan, G.; Kirkitadze, M. D.; Lomakin, A.; Vollers, S. S.; Benedek, G. B.; Teplow, D. B. Amyloid β-Protein (Aβ) Assembly: Aβ40 and Aβ42 Oligomerize through Distinct Pathways. *Proc. Natl. Acad. Sci. U.S.A.* **2003**, *100* (1), 330–335. https://doi.org/10.1073/pnas.222681699.

(16) Naiki, H.; Hashimoto, N.; Suzuki, S.; Kimura, H.; Nakakuki, K.; Gejyo, F. Establishment of a Kinetic Model of Dialysis-Related Amyloid Fibril Extension *in Vitro*. *Amyloid* **1997**, *4* (4), 223–232. https://doi.org/10.3109/13506129709003833.

(17) Serio, T. R.; Cashikar, A. G.; Kowal, A. S.; Sawicki, G. J.; Moslehi, J. J.; Serpell, L.; Arnsdorf, M. F.; Lindquist, S. L. Nucleated Conformational Conversion and the Replication of Conformational Information by a Prion Determinant. *Science* **2000**, *289* (5483), 1317–1321. https://doi.org/10.1126/science.289.5483.1317.

(18) Uversky, V. N.; Li, J.; Souillac, P.; Millett, I. S.; Doniach, S.; Jakes, R.; Goedert, M.; Fink, A. L. Biophysical Properties of the Synucleins and Their Propensities to Fibrillate. *Journal of Biological Chemistry* **2002**, *277* (14), 11970–11978. https://doi.org/10.1074/jbc.M109541200.

(19) Pedersen, J. S.; Christensen, G.; Otzen, D. E. Modulation of S6 Fibrillation by Unfolding Rates and Gatekeeper Residues. *Journal of Molecular Biology* **2004**, *341* (2), 575–588. https://doi.org/10.1016/j.jmb.2004.06.020.

(20) Uversky, V. N.; Fink, A. L. Conformational Constraints for Amyloid Fibrillation: The Importance of Being Unfolded. *Biochimica et Biophysica Acta (BBA) - Proteins and Proteomics* **2004**, *1698* (2), 131–153. https://doi.org/10.1016/j.bbapap.2003.12.008.

(21) Kelly, J. W. The Alternative Conformations of Amyloidogenic Proteins and Their Multi-Step Assembly Pathways. *Current Opinion in Structural Biology* **1998**, *8* (1), 101–106. https://doi.org/10.1016/S0959-440X(98)80016-X.

(22) Dobson, C. M. Protein Misfolding, Evolution and Disease. *Trends in Biochemical Sciences* **1999**, *24* (9), 329–332. https://doi.org/10.1016/S0968-0004(99)01445-0.

(23) Zurdo, J.; Guijarro, J. I.; Jiménez, J. L.; Saibil, H. R.; Dobson, C. M. Dependence on Solution Conditions of Aggregation and Amyloid Formation by an SH3 Domain. *Journal of Molecular Biology* **2001**, *311* (2), 325–340. https://doi.org/10.1006/jmbi.2001.4858.

(24) Su, Y.; Chang, P.-T. Acidic pH Promotes the Formation of Toxic Fibrils from β-Amyloid Peptide. *Brain Research* **2001**, *893* (1–2), 287–291. https://doi.org/10.1016/S0006-8993(00)03322-9.

(25) Kusumoto, Y.; Lomakin, A.; Teplow, D. B.; Benedek, G. B. Temperature Dependence of Amyloid β-Protein Fibrillization.

Proc. Natl. Acad. Sci. U.S.A. **1998**, *95* (21), 12277–12282. https://doi.org/10.1073/pnas.95.21.12277.

(26) DuBay, K. F.; Pawar, A. P.; Chiti, F.; Zurdo, J.; Dobson, C. M.; Vendruscolo, M. Prediction of the Absolute Aggregation Rates of Amyloidogenic Polypeptide Chains. *Journal of Molecular Biology* **2004**, *341* (5), 1317–1326. https://doi.org/10.1016/j.jmb.2004.06.043.

(27) Lomakin, A.; Teplow, D. B.; Kirschner, D. A.; Benedek, G. B. Kinetic Theory of Fibrillogenesis of Amyloid β-Protein. *Proc. Natl. Acad. Sci. U.S.A.* **1997**, *94* (15), 7942–7947. https://doi.org/10.1073/pnas.94.15.7942.

(28) Harper, J. D.; Lansbury, P. T. MODELS OF AMYLOID SEEDING IN ALZHEIMER'S DISEASE AND SCRAPIE: Mechanistic Truths and Physiological Consequences of the Time-Dependent Solubility of Amyloid Proteins. *Annu. Rev. Biochem.* **1997**, *66* (1), 385–407. https://doi.org/10.1146/annurev.biochem.66.1.385.

(29) Dobson, C. M. Protein Folding and Misfolding. *Nature* **2003**, *426* (6968), 884–890. https://doi.org/10.1038/nature02261.

(30) Wurth, C.; Guimard, N. K.; Hecht, M. H. Mutations That Reduce Aggregation of the Alzheimer's Aβ42 Peptide: An Unbiased Search for the Sequence Determinants of Aβ Amyloidogenesis. *Journal of Molecular Biology* **2002**, *319* (5), 1279–1290. https://doi.org/10.1016/S0022-2836(02)00399-6.

(31) Chiti, F.; Dobson, C. M. Protein Misfolding, Amyloid Formation, and Human Disease: A Summary of Progress Over the Last Decade. *Annu. Rev. Biochem.* **2017**, *86* (1), 27–68. https://doi.org/10.1146/annurev-biochem-061516-045115.

(32) Calamai, M.; Taddei, N.; Stefani, M.; Ramponi, G.; Chiti, F. Relative Influence of Hydrophobicity and Net Charge in the Aggregation of Two Homologous Proteins. *Biochemistry* **2003**, *42* (51), 15078–15083. https://doi.org/10.1021/bi030135s.

(33) Chiti, F.; Calamai, M.; Taddei, N.; Stefani, M.; Ramponi, G.; Dobson, C. M. Studies of the Aggregation of Mutant Proteins *in Vitro* Provide Insights into the Genetics of Amyloid Diseases. *Proc. Natl. Acad. Sci. U.S.A.* **2002**, *99* (suppl_4), 16419–16426. https://doi.org/10.1073/pnas.212527999.

(34) Fandrich, M. The Behaviour of Polyamino Acids Reveals an Inverse Side Chain Effect in Amyloid Structure Formation. *The EMBO Journal* **2002**, *21* (21), 5682–5690. https://doi.org/10.1093/emboj/cdf573.

(35) Kallberg, Y.; Gustafsson, M.; Persson, B.; Thyberg, J.; Johansson, J. Prediction of Amyloid Fibril-Forming Proteins. *Journal of Biological Chemistry* **2001**, *276* (16), 12945–12950. https://doi.org/10.1074/jbc.M010402200.

(36) Pawar, A. P.; DuBay, K. F.; Zurdo, J.; Chiti, F.; Vendruscolo, M.; Dobson, C. M. Prediction of "Aggregation-Prone" and "Aggregation-Susceptible" Regions in Proteins Associated with Neurodegenerative Diseases. *Journal of Molecular Biology* **2005**, *350* (2), 379–392. https://doi.org/10.1016/j.jmb.2005.04.016.

(37) De Groot, N. S.; Pallarés, I.; Avilés, F. X.; Vendrell, J.; Ventura, S. Prediction of "Hot Spots" of Aggregation in Disease-Linked Polypeptides. *BMC Struct Biol* **2005**, *5* (1), 18. https://doi.org/10.1186/1472-6807-5-18.

(38) Kulshreshtha, S.; Chaudhary, V.; Goswami, G. K.; Mathur, N. Computational Approaches for Predicting Mutant Protein Stability. *J Comput Aided Mol Des* **2016**, *30* (5), 401–412. https://doi.org/10.1007/s10822-016-9914-3.

(39) Bliven, S.; Prlić, A. Circular Permutation in Proteins. *PLoS Comput Biol* **2012**, *8* (3), e1002445. https://doi.org/10.1371/journal.pcbi.1002445.

(40) Cunningham, B. A.; Hemperly, J. J.; Hopp, T. P.; Edelman, G. M. Favin versus Concanavalin A: Circularly Permuted Amino Acid Sequences. *Proc. Natl. Acad. Sci. U.S.A.* **1979**, *76* (7), 3218–3222. https://doi.org/10.1073/pnas.76.7.3218.

(41) Goldenberg, D. P.; Creighton, T. E. Circular and Circularly Permuted Forms of Bovine Pancreatic Trypsin Inhibitor. *Journal of Molecular Biology* **1983**, *165* (2), 407–413. https://doi.org/10.1016/S0022-2836(83)80265-4.

(42) Luger, K.; Hommel, U.; Herold, M.; Hofsteenge, J.; Kirschner, K. Correct Folding of Circularly Permuted Variants of a Bα Barrel

Enzyme in Vivo. *Science* **1989**, *243* (4888), 206–210. https://doi.org/10.1126/science.2643160.

(43) Dobson, C. M. The Structural Basis of Protein Folding and Its Links with Human Disease. *Phil. Trans. R. Soc. Lond. B* **2001**, *356* (1406), 133–145. https://doi.org/10.1098/rstb.2000.0758.

(44) Selkoe, D. J. Alzheimer's Disease Is a Synaptic Failure. *Science* **2002**, *298* (5594), 789–791. https://doi.org/10.1126/science.1074069.

(45) Lohcharoenkal, W.; Wang, L.; Chen, Y. C.; Rojanasakul, Y. Protein Nanoparticles as Drug Delivery Carriers for Cancer Therapy. *BioMed Research International* **2014**, *2014*, 1–12. https://doi.org/10.1155/2014/180549.

(46) Lam, P.-L.; Wong, W.-Y.; Bian, Z.; Chui, C.-H.; Gambari, R. Recent Advances in Green Nanoparticulate Systems for Drug Delivery: Efficient Delivery and Safety Concern. *Nanomedicine* **2017**, *12* (4), 357–385. https://doi.org/10.2217/nnm-2016-0305.

(47) Jahangirian, H.; Ghasemian Lemraski, E.; Webster, T. J.; Rafiee-Moghaddam, R.; Abdollahi, Y. A Review of Drug Delivery Systems

Based on Nanotechnology and Green Chemistry: Green Nanomedicine. *IJN* **2017**, *Volume 12*, 2957–2978. https://doi.org/10.2147/IJN.S127683.

(48) Kimura, T.; Uzawa, T.; Ishimori, K.; Morishima, I.; Takahashi, S.; Konno, T.; Akiyama, S.; Fujisawa, T. Specific Collapse Followed by Slow Hydrogen-Bond Formation of β-Sheet in the Folding of Single-Chain Monellin. *Proc. Natl. Acad. Sci. U.S.A.* **2005**, *102* (8), 2748–2753. https://doi.org/10.1073/pnas.0407982102.

(49) Patra, A. K.; Udgaonkar, J. B. Characterization of the Folding and Unfolding Reactions of Single-Chain Monellin: Evidence for Multiple Intermediates and Competing Pathways. *Biochemistry* **2007**, *46* (42), 11727–11743. https://doi.org/10.1021/bi701142a.

(50) Jha, S. K.; Udgaonkar, J. B. Direct Evidence for a Dry Molten Globule Intermediate during the Unfolding of a Small Protein. *Proc. Natl. Acad. Sci. U.S.A.* **2009**, *106* (30), 12289–12294. https://doi.org/10.1073/pnas.0905744106.

(51) Pica, A.; Leone, S.; Di Girolamo, R.; Donnarumma, F.; Emendato, A.; Rega, M. F.; Merlino, A.; Picone, D. pH Driven Fibrillar

Aggregation of the Super-Sweet Protein Y65R-MNEI: A Step-by-Step Structural Analysis. *Biochimica et Biophysica Acta (BBA) - General Subjects* **2018**, *1862* (4), 808–815. https://doi.org/10.1016/j.bbagen.2017.12.012.

(52) Donnarumma, F.; Emendato, A.; Leone, S.; Ercole, C.; D'Errico, G.; Picone, D. Salt Modulated Fibrillar Aggregation of the Sweet Protein MNEI in Aqueous Solution. *J Solution Chem* **2018**, *47* (5), 939–949. https://doi.org/10.1007/s10953-018-0764-6.

(53) Donnarumma, F.; Leone, S.; Delfi, M.; Emendato, A.; Ami, D.; Laurents, D. V.; Natalello, A.; Spadaccini, R.; Picone, D. Probing Structural Changes during Amyloid Aggregation of the Sweet Protein MNEI. *FEBS J* **2020**, *287* (13), 2808–2822. https://doi.org/10.1111/febs.15168.

(54) Liu, Q.; Li, L.; Yang, L.; Liu, T.; Cai, C.; Liu, B. Modification of the Sweetness and Stability of Sweet-Tasting Protein Monellin by Gene Mutation and Protein Engineering. *BioMed Research International* **2016**, *2016*, 1–7. https://doi.org/10.1155/2016/3647173.

(55) Rega, M. F.; Di Monaco, R.; Leone, S.; Donnarumma, F.; Spadaccini, R.; Cavella, S.; Picone, D. Design of Sweet Protein Based Sweeteners: Hints from Structure–Function Relationships. *Food Chemistry* **2015**, *173*, 1179–1186. https://doi.org/10.1016/j.foodchem.2014.10.151.

(56) Delfi, M.; Emendato, A.; Leone, S.; Lampitella, E. A.; Porcaro, P.; Cardinale, G.; Petraccone, L.; Picone, D. A Super Stable Mutant of the Plant Protein Monellin Endowed with Enhanced Sweetness. *Life* **2021**, *11* (3), 236. https://doi.org/10.3390/life11030236.

(57) Sun, Z.; Liu, Q.; Qu, G.; Feng, Y.; Reetz, M. T. Utility of B-Factors in Protein Science: Interpreting Rigidity, Flexibility, and Internal Motion and Engineering Thermostability. *Chem. Rev.* **2019**, *119* (3), 1626–1665. https://doi.org/10.1021/acs.chemrev.8b00290.

(58) Vriend, G. WHAT IF: A Molecular Modeling and Drug Design Program. *Journal of Molecular Graphics* **1990**, *8* (1), 52–56. https://doi.org/10.1016/0263-7855(90)80070-V.

(59) Pettersen, E. F.; Goddard, T. D.; Huang, C. C.; Couch, G. S.; Greenblatt, D. M.; Meng, E. C.; Ferrin, T. E. UCSF Chimera?A

Visualization System for Exploratory Research and Analysis. *J. Comput. Chem.* **2004**, *25* (13), 1605–1612. https://doi.org/10.1002/jcc.20084.

(60) Esposito, V.; Gallucci, R.; Picone, D.; Saviano, G.; Tancredi, T.; Temussi, P. A. The Importance of Electrostatic Potential in The Interaction of Sweet Proteins with the Sweet Taste Receptor. *Journal of Molecular Biology* **2006**, *360* (2), 448–456. https://doi.org/10.1016/j.jmb.2006.05.020.

(61) Zheng, W.; Yang, L.; Cai, C.; Ni, J.; Liu, B. Expression, Purification and Characterization of a Novel Double-Sites Mutant of the Single-Chain Sweet-Tasting Protein Monellin (MNEI) with Both Improved Sweetness and Stability. *Protein Expression and Purification* **2018**, *143*, 52–56. https://doi.org/10.1016/j.pep.2017.10.010.

(62) Weiffert, T.; Linse, S. Protein Stabilization with Retained Function of Monellin Using a Split GFP System. *Sci Rep* **2018**, *8* (1), 12763. https://doi.org/10.1038/s41598-018-31177-z.

(63) Aghera, N.; Dasgupta, I.; Udgaonkar, J. B. A Buried Ionizable Residue Destabilizes the Native State and the Transition State in the Folding of Monellin. *Biochemistry* **2012**, *51* (45), 9058–9066. https://doi.org/10.1021/bi3008017.

(64) Delfi, M.; Leone, S.; Emendato, A.; Ami, D.; Borriello, M.; Natalello, A.; Iannuzzi, C.; Picone, D. Understanding the Self-Assembly Pathways of a Single Chain Variant of Monellin: A First Step towards the Design of Sweet Nanomaterials. *International Journal of Biological Macromolecules* **2020**, *152*, 21–29. https://doi.org/10.1016/j.ijbiomac.2020.02.229.

(65) Sarroukh, R.; Goormaghtigh, E.; Ruysschaert, J.-M.; Raussens, V. ATR-FTIR: A "Rejuvenated" Tool to Investigate Amyloid Proteins. *Biochimica et Biophysica Acta (BBA) - Biomembranes* **2013**, *1828* (10), 2328–2338. https://doi.org/10.1016/j.bbamem.2013.04.012.

(66) Schlunegger, M.; Bennett, M.; Eisenberg, D. Oligomer Formation By 3D Domain Swapping: A Model For Protein Assembly And Misassembly. In *Advances in Protein Chemistry*; Elsevier, 1997; Vol. 50, pp 61–122. https://doi.org/10.1016/S0065-3233(08)60319-8.

(67) Vonrhein, C.; Flensburg, C.; Keller, P.; Sharff, A.; Smart, O.; Paciorek, W.; Womack, T.; Bricogne, G. Data Processing and Analysis with the autoPROC Toolbox. *Acta Crystallogr D Biol Crystallogr* **2011**, *67* (4), 293–302. https://doi.org/10.1107/S0907444911007773.

(68) Murshudov, G. N.; Skubák, P.; Lebedev, A. A.; Pannu, N. S.; Steiner, R. A.; Nicholls, R. A.; Winn, M. D.; Long, F.; Vagin, A. A. REFMAC 5 for the Refinement of Macromolecular Crystal Structures. *Acta Crystallogr D Biol Crystallogr* **2011**, *67* (4), 355–367. https://doi.org/10.1107/S0907444911001314.

(69) Emsley, P.; Lohkamp, B.; Scott, W. G.; Cowtan, K. Features and Development of Coot. *Acta Crystallogr D Biol Crystallogr* **2010**, *66* (4), 486–501. https://doi.org/10.1107/S0907444910007493.

CHAPTER 3

hHFt as a model for fibrillar nanostructured biomaterials

STATE OF ART

As already reported in the previous chapter, generally amyloid structures originate from soluble peptides and proteins, wherein peptide or protein monomers spontaneously or induced by stress self-associate into small oligomers, then into supramolecular aggregates, and finally, they form fibrillar structures[1,2]. Native-state globular proteins, as opposed to smaller pathological peptides, possess a condensed, defined structure, so their fibrillation occurs from the destabilization of the native structure into partially unfolded conformations via substantial changes in environmental conditions (mainly temperature and/or pH)[3].

Among the soluble proteins representing possible building-blocks for functional amyloid, Jurado and coworkers reported for the first time the conversion of apoferritin into amyloid-like fibers[4]. The morphology, size and stiffness of these one-dimensional structures are comparable to the fibrils formed by β-lactoglobulin, a protein frequently used as a model in the study of amyloid-like fibrillar proteins. Nanometre-sized globular apoferritin is capable of self-assembling to form 1D micrometre-sized structures after being subjected to a heating process. Depending on the experimental conditions, fibrils with different morphologies and sizes were obtained.

The study of ferritin fibrillation abilities is of particular interest for several reasons. Among them, there is the fact that alterations in ferritin functions have been associated with common iron-related diseases such as hemochromatosis and anaemia[5]. In addition, many works have reported the involvement of ferritin in some neurological pathologies such as Parkinson's and Alzheimer's disease[6]. Furthermore, the possibility of use a nanocage structured protein open new ways for the creation of functional materials with novel or improved properties.

Based on these premises, fibrils of human H-chain ferritin have been prepared and characterized by different techniques, analyzing the kinetics of formation and their shape and dimensions.

RESULTS AND DISCUSSION

The optimal experimental conditions[3] to obtain human H-chain ferritin fibrils ($hHFt_{fibril}$) is at pH 2.0, 90 °C temperature, 90 rpm stirring, and a protein concentration of 2.0 mg mL^{-1}. The growth kinetics $hHFt_{fibril}$ was studied by combining several techniques. Time-dependent intermediates of the evolving fibrils were collected by quenching aliquots of the samples at room temperature at specific incubation times (0, 5, 15, 30, 45 min and 1, 5, 6, 24 h).

Since protein hydrolysis seems an important step for amyloid aggregation, the presence of possible protein fragments at different incubation times has been investigated using SDS-PAGE electrophoresis (**Figure 3.1**). At time zero at pH 2.0, the original ferritin subunit band at around 20 kDa is still visible while after 1 h of incubation, the amount is already considerably reduced compared to the initial conditions. The appearance of the 11–13 kDa bands in the early stages of incubation is consistent with partial hydrolysis. A band at around 5 kDa was evident after incubation for 5 min, indicating a very high rate of hydrolysis. After 3 h of incubation, the native protein band at 20 kDa disappeared, which could be compatible with the formation of fibrils. After 24 h, the native protein was completely hydrolyzed, and only low-molecular-weight peptide fragments (<5 kDa) were present in the system. These results confirm the decisive role of protein hydrolysis in the formation of amyloid fibrils.

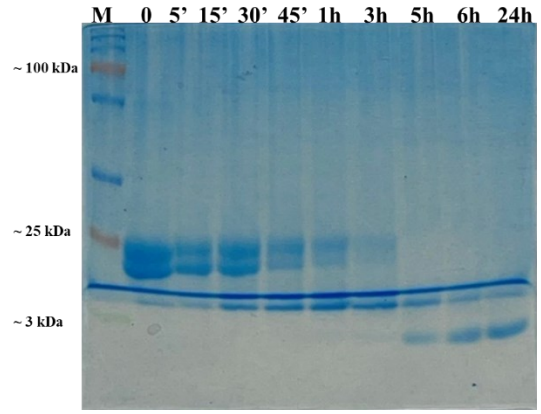

Figure 3.1. 12% SDS-PAGE of hHFt incubated at pH 2.0 and heated at 90 °C for different incubation times.

The hallmark of amyloid assemblies is a conformational transition of the constituent monomeric proteins into a β-sheet-rich fibril. Therefore, changes in the secondary structure content of $hHFt_{fibril}$ with incubation times were followed using circular dichroism spectroscopy (**Figure 3.2**). As observed in the graph reporting the superposition of CD spectra of ferritin upon different incubation times, from zero up to 5 hours, the protein spectral profile changes overtime. Indeed, at time zero, the spectrum showed a trend typical of proteins with a high content of α-helix secondary structures, as ferritin, whose subunit is a four-helix bundle, with two broad minima at 208 and 222 nm and a positive peak around 195 nm. Over incubation time, this profile changed. After 30 minutes, the CD spectrum indicated the persistence of α-helix secondary

structures, even if there was a pronounced reduction in helical content relative to the initial spectrum, which is evident based on the decrease in ellipticity intensity. After 1 hour the minimum at 222 nm disappears and the one at 208 nm shift to lower wavelength values; the shoulder at around 217 nm suggests the presence of β-sheet structures, as expected for the observed well-ordered amyloid aggregates. The proposed sequence should be from α-helix to random (via denaturation and hydrolysis–physical and chemical damage) and slow assembly toward β-sheet formation in selected sequences. In fact, over 5 hours, the CD spectrum has completely changed showing the characteristic signature of β-sheet-rich amyloids.

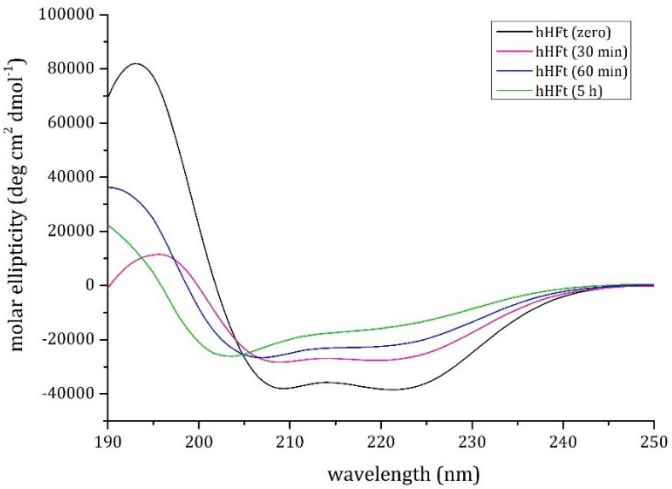

Figure 3.2. Far-UV circular dichroism of hHFt incubated at pH 2.0 and heated at 90 °C for different incubation times.

The kinetics of $hHFt_{fibrils}$ aggregation was studied also by means of the thioflavin-T (ThT) fluorescence assay. The formation of amyloid aggregates was detected as an increase in ThT fluorescence intensity, with a characteristic emission band centered at 482 nm. **Figure 3.3** shows the increase in ThT fluorescence upon binding to amyloid-like fibrils. In the early stages of aggregation, the fluorescence intensity increased, corresponding to the formation of small aggregates. There was a short lag phase in the first hour during which the fluorescence intensity remained low. At incubation times of over 3 h, when the first fibrils formed, the ThT fluorescence intensity increased and plateaued at a maximum after 24 h when mature fibrils were predominantly formed.

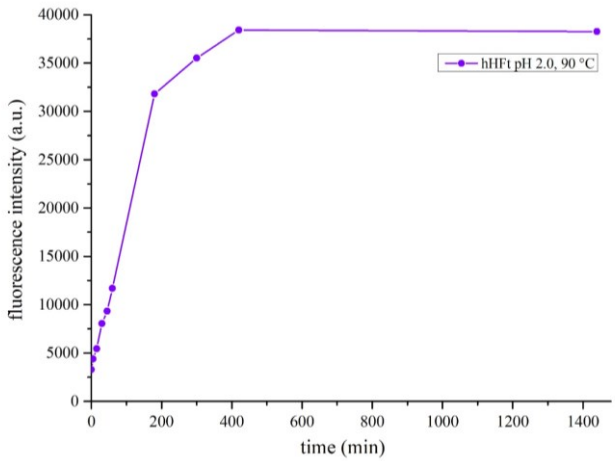

Figure 3.3. Time course of ThT binding assay of hHFt incubated at pH 2.0 and heated at 90 °C for different incubation times. Fluorescence emission was recorded at 485 nm at the indicated times.

Finally, the structural and morphology evolution of the hHFt$_{fibril}$ was characterized in detail using TEM (**Figure 3.4**). The images reported below show the presence of huge network of long well-defined fibrils.

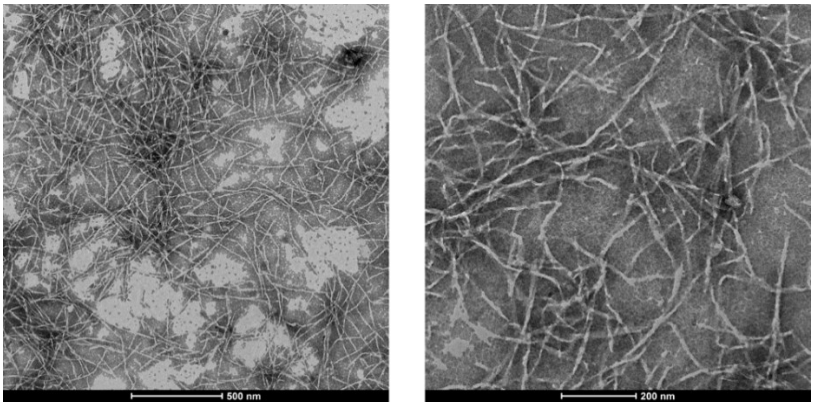

Figure 3.4. TEM images of hHFt incubated at pH 2.0 and heated at 90 °C.

The obtained fibrils, thanks to the big dimensions, allowed a macroscopic characterization by SEM. Images are reported in **Figure 3.5**, and also indicate their length, about 600 µm.

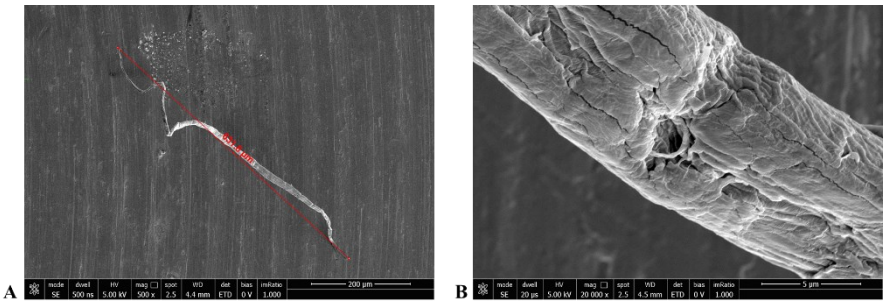

Figure 3.5. SEM images of hHFt incubated at pH 2.0 and heated at 90 °C.

As recently reported, ferritin, a key component in the regulation of brain iron homeostasis, forms amyloid fibrils that share common traits with the pathological amyloid fibrils found in Alzheimer's and Parkinson's diseases. In this study, the chemical conditions to form long, rigid fibrils from human H-chain ferritin were optimized. hHFt fibril growth kinetics have been then described. An incubation period of 9 h, a protein concentration of 2.0 mg mL^{-1}, and a stirring rate of 90 rpm are the optimal parameters to form well-structured long fibrils from hHFt protein. In addition, it has been demonstrated that the formation of ferritin amyloid fibrils starts from short oligomer aggregates that develop into long, mature fibrils after 3 h at 90 °C. SDS-PAGE and circular dichroism provide convincing evidence that the protein unfolding together with its partial hydrolysis are essential for the formation of large aggregates, and that small peptide fragments (<5 kDa) are involved in fibril formation. TEM measurements helped to define shape and dimension of the fibrils obtained from this experiment. All these results taken together, deepening the understanding of ferritin fibrillation, open up the possibility of using polypeptide chain primary structure as a mean to access new forms of protein tertiary and quaternary nanostructures and

pave the way to the use of this multitasking protein to produce novel biomaterials.

MATERIAL AND METHODS

1. Preparation of hHFt fibrils ($hHFt_{fibril}$)

Human H-chain ferritin was expressed and purified as reported in **Material and Methods** section of **Chapter 1.**

The pH of a solution of native hHFt at a concentration of 2.0 mg mL^{-1} was adjusted to pH 2.0 by adding 1.0 M HCl before heating treatment. Then hHFt was heated at 90 °C on a stirrer hot plate for 24 h and at 90 rpm.

2. TEM

Aliquots of the protein solution were taken and diluted 50 times with deionized water. 3 μL drops of the samples were deposited for 3 minutes on a carbon-coated copper TEM grid (200 mesh) and then, the excess fluid was drained off with filter paper and air-dried. To enhance the contrast, negative staining with 1.5% phosphotungstic acid (PTA) solution at pH 7.0 was carried out by depositing a drop of PTA solution

on the grid containing the sample for 4 min and then the excess fluid was drained off with filter paper. The images were collected using a FEI TECNAI G2 S-twin apparatus operating at 120 kV (LaB6 source).

3. Circular dichroism

Far-UV CD spectra were recorded on a Jasco J-715 spectropolarimeter equipped with a Peltier thermostatic cell holder (Model PTC-348WI) in the range of 190–250 nm, using protein concentration of 0.1 mg mL^{-1} in 10 mM sodium phosphate buffer pH 7.4 and 20 mM Tris HCl pH 7.4, and a 0.1 cm path length quartz cuvette. Each spectrum was obtained by averaging three scans and converting the signal to mean residue ellipticity in units of deg cm^2 $dmol^{-1}$. Other experimental settings were scanning speed 50 nm min^{-1}, bandwidth 2.0 nm, resolution 1.0 nm, sensitivity 50 mdeg and response 2 s.

4. ThT binding assay

ThT fluorescence emission was recorded after the addition of 25 μL of $hHFt_{fibril}$ aliquots to 25 μL of 56 μM ThT solution at pH 20. Fluorescence emission spectra were recorded on a HORIBA Fluoromax-4 in the range of 400-600 nm with scan speed of 100 nm/min, upon excitation at 440

nm. Excitation and emission slits were both set at 5 nm. Fluorescence intensity values at 485 nm emission were plotted as a function of time.

REFERENCES

(1) Hauser, C. A. E.; Maurer-Stroh, S.; Martins, I. C. Amyloid-Based Nanosensors and Nanodevices. *Chem. Soc. Rev.* **2014**, *43* (15), 5326. https://doi.org/10.1039/C4CS00082J.

(2) Miti, T.; Mulaj, M.; Schmit, J. D.; Muschol, M. Stable, Metastable, and Kinetically Trapped Amyloid Aggregate Phases. *Biomacromolecules* **2015**, *16* (1), 326–335. https://doi.org/10.1021/bm501521r.

(3) Jurado, R.; Adamcik, J.; Sánchez-Ferrer, A.; Bolisetty, S.; Mezzenga, R.; Gálvez, N. Understanding the Formation of Apoferritin Amyloid Fibrils. *Biomacromolecules* **2021**, *22* (5), 2057–2066. https://doi.org/10.1021/acs.biomac.1c00176.

(4) Jurado, R.; Castello, F.; Bondia, P.; Casado, S.; Flors, C.; Cuesta, R.; Domínguez-Vera, J. M.; Orte, A.; Gálvez, N. Apoferritin Fibers: A New Template for 1D Fluorescent Hybrid Nanostructures. *Nanoscale* **2016**, *8* (18), 9648–9656. https://doi.org/10.1039/C6NR01044J.

(5) Drakesmith, H.; Chen, N.; Ledermann, H.; Screaton, G.; Townsend, A.; Xu, X.-N. HIV-1 Nef down-Regulates the Hemochromatosis Protein HFE, Manipulating Cellular Iron Homeostasis. *Proc. Natl. Acad. Sci. U.S.A.* **2005**, *102* (31), 11017–11022. https://doi.org/10.1073/pnas.0504823102.

(6) Connor, J. R.; Snyder, B. S.; Arosio, P.; Loeffler, D. A.; LeWitt, P. A Quantitative Analysis of Isoferritins in Select Regions of Aged, Parkinsonian, and Alzheimer's Diseased Brains. *Journal of Neurochemistry* **1995**, *65* (2), 717–724. https://doi.org/10.1046/j.1471-4159.1995.65020717.x.

CONCLUSIONS

The design of new materials for biological applications requires a deep knowledge of the mechanisms controlling their building and construction. One of the most intriguing processes which is involved in the formation of new potential biomaterials is the molecular self-assembly process, recently emerged as a promising approach in chemical synthesis, nanotechnology, polymer science, and engineering. Systems able to form self-assembled structures lie at the interface between structural biology and engineering and embrace different types of molecules, ranging from copolymers, complex DNA structures, simple and complex proteins, and peptides. The key engineering principle for molecular self-assembly is to artfully design molecular building blocks that can undergo stepwise interactions and assemblies through the formations of non-covalent intermolecular interactions, such as hydrogen bonds, ionic bonds and van der Waals' bonds forming well-defined and stable hierarchical macroscopic structures. Although some bonds are rather weak, the collective interactions can result in very stable structures and materials. The fundamental elements in molecular self-assembly are chemical complementarity and structural compatibility.

Protein-based nanomaterials represents the topic of the PhD project here presented. Notably, protein mechanisms responsible for the formation of protein aggregates have been deeply investigated with a peculiar attention to the study of structure and morphology of the obtained aggregates. The protein aggregates under discussion comprised 3D architectures, and 1D materials. In particular, nanocages of ferritin were taken into account in the first case and amyloid fibrils obtained from monellin single chain derivatives in the second one. The assembly mechanism accountable for the formation of nanocages of human H-chain ferritin (hHFt), the chosen model of ferritin, was examined in detail, pointing the attention also on the reassembly process evaluated in term of protein amount and structural homogeneity of the recovered product. Regarding this point, a first experimental approach aimed to verify if hHFt has the same ability of other ferritins to disassemble and reassemble at alkaline pH, the most used protocol to load bioactive molecules for the development of potential drug delivery systems. A comparative study with horse spleen ferritin, already used to encapsulate several metallodrugs, has highlighted the hHFt incapacity to be disassembled at pH 13.0. Indeed, X-ray diffraction studies revealed that the Au complex that had to be encapsulated was bound to the protein

outer surface. A further investigation of the efficacy of the encapsulation procedures reported in literature, based on the pH switch, underlined, the relevant drawbacks of the currently available protocols, including for example not satisfactory protein recovery and lack of homogeneity. Conversely, the new protocol developed during my thesis, based on the use of small amounts of SDS, allowed quantitative disassembly and high-yield recovery of hHFt nanocages with structural properties identical to those of the untreated form as confirmed by X-ray crystallography and TEM. Moreover, the new protocol, applied to load a ruthenium compound and a hemolytic peptide within the protein nanocage, showed how drug encapsulation in hHFt can have significant advantages, such as increased solubility of the loaded small molecules, decreased immunogenicity, and especially selective targeting towards tumor cells preventing other possible side effects of the drug. Again, the protein recovery was quantitative. A biological characterization of hHFt loaded with the hemolytic peptide demonstrated the range of advantages shown by this nanocarrier. In fact, ferritin nanocages seem to accomplish several roles i) protecting the peptide from possible environmental damages; ii) impairing the dangerous side effects of the peptide on

normal cells and iii) specifically driving the cargo peptide to the cancer cells by the selective interaction with TfR1 receptors.

Despite the quantification of encapsulated peptide is a critical point of the process, the presence of the nanocage seems to reduce the peptide amount necessary to disrupt the tumour cells. Finally, it has been suggested that the toxicity of the encapsulated peptide might involve an oxidative stress on cancer cells, although further studies are needed to better clarify the molecular mechanism of the encapsulated peptide. Notably, while the toxicity of the free peptide is mediated by a destructive interaction with the external membrane of different cellular lines, the hHFt nanocage carries the peptide inside the tumour cell through a receptor-mediated endocytosis mechanism, inducing the cellular death by a different route, while assuring a specificity for malignant cells. Therefore, this thesis reported an alternative, efficient, reproducible, and versatile procedure to reversibly disassemble hHFt under mild pH conditions, without altering ferritin assembly, function, or safety. The new method can be applied to encapsulate different types of molecules showing interesting pharmacological activities preserving their structure and biological role. This finding strengthens the

possibility to use human H-chain ferritin as a carrier system to selectively deliver highly toxic drugs to specific cellular targets in a safe manner.

The protein assembly mechanism was also studied from another point of view, *i.e.* prompting the conversion of a globular protein, single chain plant protein monellin, into amyloid fibrils. Among the variety of designed monellin mutants, the attention has been focused on two types of mutants: Mut9, obtained by rational driven site-directed mutagenesis, and Perms (1, 2, 3), obtained by circular permutation. Mut9 has been already characterized as a super stable mutant[9]. Here, a structural characterization by X-ray of two well-known single chain monellin mutants, reveled the grounds of their different stability, demonstrated that all the point mutations in Mut9 eliminate unfavored interaction and create new ones. Furthermore, using a combination of biophysical techniques, it has been showed that Mut9 can be converted into fibrils not only at acidic pH, as reported for MNEI, but also at neutral pH, independently from the ionic strength. Therefore, this mutant has a greater potential to be used as building block for the construction of amyloid fibrils. TEM analysis revealed that fibrils of different size and morphology can be obtained at two pH values. The ability of Mut9 to form long well-defined fibrillar aggregates allowed the acquisition of

Cryo-EM images, whose analysis is in progress. Moreover, the obtained fibrils were big enough to be visible at the human eye. This feature allowed the isolation of fibrils for a macroscopic characterization by SEM. The possibility of isolate Mut9 fibrils represent an important result since it opens the way to the construction of both nano- and micro-structured materials for different application in the biotechnology field.

The second system analyzed, based on Perm1, Perm2 and Perm3 mutants, gave very different results compared not only to Mut9, but even to MNEI. Indeed, these proteins showed a lower tendency to form fibrillar aggregates and seemed worst candidates as amyloid fibrils building blocks. However, the investigation of the grounds of these differences, which are pronounced also among the three mutants, suggests a strong correlation between the length of Perm mutants' linkers and their tendency to exist in solution either in a monomeric or dimeric form. In particular, Perm3, which has the shortest linker, is isolated as 50% of dimer and 50% of monomer, suggesting an equilibrium between the two forms. Moreover, this tendency reduces the ability to form amyloid aggregates. In particular, the three mutants show an opposite behavior between the tendency to dimerize and the capability to form amyloid fibrils. This suggests that the dimeric form is off pathway with

respect to the amyloid aggregation, which is instead triggered by a partial unfolding of monomeric form. None of this mutant has an improved tendency to form amyloid fibrils with respect to the parent protein MNEI, or with respect to Mut 9, which proved to be a very versatile building block.

Interestingly, in the last weeks of my thesis, I obtained very intriguing results, albeit preliminary, by converting Ft nanocages into amyloid fibrils. The characterization of morphology and size of these obtained fibrils were strongly promising. Indeed, SEM analysis showed that, as Mut9, also hHFt can be suitable to produce long well-defined fibrils, visible and isolable.

In the end, this work demonstrated that the obtained supramolecular assemblies open the way for different scales structural characterization and biotechnological applications.